MINISTÉRIO DA CIÊNCIA, TECNOLOGIA E INOVAÇÕES
INSTITUTO NACIONAL DE PESQUISAS ESPACIAIS

sid.inpe.br/mtc-m21d/2022/09.06.18.49-TDI

MODELING GEOMAGNETICALLY INDUCED CURRENTS IN BRAZILIAN POWER NETWORKS USING 3-D MODELS TO REPRESENT THE SUBSURFACE ELECTRICAL CONDUCTIVITY STRUCTURE

Karen Viviana Espinosa Sarmiento

Doctorate Thesis of the Graduate Course in Space Geophysics, guided by Drs. Antonio Lopes Padilha, Lívia Ribeiro Alves, and Adam Schultz, approved in August 11, 2022.

URL of the original document:
<http://urlib.net/8JMKD3MGP3W34T/47JAE7S>

INPE
São José dos Campos
2022

PUBLISHED BY:

Instituto Nacional de Pesquisas Espaciais - INPE
Coordenação de Ensino, Pesquisa e Extensão (COEPE)
Divisão de Biblioteca (DIBIB)
CEP 12.227-010
São José dos Campos - SP - Brasil
Tel.:(012) 3208-6923/7348
E-mail: pubtc@inpe.br

MINISTÉRIO DA CIÊNCIA, TECNOLOGIA E INOVAÇÕES
INSTITUTO NACIONAL DE PESQUISAS ESPACIAIS

sid.inpe.br/mtc-m21d/2022/09.06.18.49-TDI

MODELING GEOMAGNETICALLY INDUCED CURRENTS IN BRAZILIAN POWER NETWORKS USING 3-D MODELS TO REPRESENT THE SUBSURFACE ELECTRICAL CONDUCTIVITY STRUCTURE

Karen Viviana Espinosa Sarmiento

Doctorate Thesis of the Graduate Course in Space Geophysics, guided by Drs. Antonio Lopes Padilha, Lívia Ribeiro Alves, and Adam Schultz, approved in August 11, 2022.

URL of the original document:
<http://urlib.net/8JMKD3MGP3W34T/47JAE7S>

INPE
São José dos Campos
2022

Cataloging in Publication Data

Espinosa Sarmiento, Karen Viviana.

Es65m Modeling geomagnetically induced currents in brazilian power networks using 3-D models to represent the subsurface electrical conductivity structure / Karen Viviana Espinosa Sarmiento. – São José dos Campos : INPE, 2022.

xxviii + 138 p. ; (sid.inpe.br/mtc-m21d/2022/09.06.18.49-TDI)

Thesis (Doctorate in Space Geophysics) – Instituto Nacional de Pesquisas Espaciais, São José dos Campos, 2022.

Guiding : Drs. Antonio Lopes Padilha, Lívia Ribeiro Alves, and Adam Schultz.

1. 3-D resistivity model. 2. Geomagnetic storms. 3. Geoelectric field. 4. Power transmission network. 5. GIC modeling. I.Title.

CDU 551.521.1/2

MINISTÉRIO DA CIÊNCIA, TECNOLOGIA E INOVAÇÕES

INSTITUTO NACIONAL DE PESQUISAS ESPACIAIS

Secretaria e Pós-Graduação - SEPGR

DEFESA FINAL DE TESE DE KAREN VIVIANA ESPINOSA SARMIENTO
REG 136328/2018, BANCA Nº 209/2022

No dia 11 de agosto de 2022, às 13h, por teleconferência, o(a) aluno(a) mencionado(a) acima defendeu seu trabalho final (apresentação oral seguida de arguição) perante uma Banca Examinadora, cujos membros estão listados abaixo. O(A) aluno(a) foi APROVADO(A) pela Banca Examinadora, por unanimidade, em cumprimento ao requisito exigido para obtenção do Título de Doutora em Geofísica Espacial/Ciências do Ambiente Solar-Terrestre. O trabalho precisa da incorporação das correções sugeridas pela Banca Examinadora e revisão final pelo(s) orientador(es).

Título: "Modeling Geomagnetically Induced Currents in Brazilian Power Networks using 3-D Models to Represent the Subsurface Electrical Conductivity Structure"

Membros da banca:

Dr. Cristiano Max Wrasse - Presidente - INPE

Dr. Antonio Lopes Padilha - Orientador - INPE

Dra. Lívia Ribeiro Alves - Orientadora - INPE

Dr. Adam Schultz - Orientador - Oregon State University-OSU

Dr. Severino Luiz Guimaraes Dutra - Membro interno - INPE

Dr. Sergio Luiz Fontes - Membro externo - Observatório Nacional-ON

Dr. Mauricio de Souza Bologna - Membro externo - USP

Documento assinado eletronicamente por **Severino Luiz Guimarães Dutra (E)**, **Usuário Externo**, em 12/08/2022, às 15:43 (horário oficial de Brasília), com fundamento no § 3º do art. 4º do Decreto nº 10.543, de 13 de novembro de 2020.

Documento assinado eletronicamente por **Cristiano Max Wrasse**, **Pesquisador**, em 12/08/2022, às 15:44 (horário oficial de Brasília), com fundamento no § 3º do art. 4º do Decreto nº 10.543, de 13 de novembro de 2020.

Documento assinado eletronicamente por **mauricio de souza bologna (E)**, **Usuário Externo**, em 12/08/2022, às 15:57 (horário oficial de Brasília), com fundamento no § 3º do art. 4º do Decreto nº 10.543, de 13 de novembro de 2020.

Documento assinado eletronicamente por **Sergio Luiz Fontes**, **Pesquisadora**, em 12/08/2022, às 16:18 (horário oficial de Brasília), com fundamento no § 3º do art. 4º do Decreto nº 10.543, de 13 de novembro de 2020.

Documento assinado eletronicamente por **Livia Ribeiro Alves**, **Pesquisadora**, em 12/08/2022, às 16:21 (horário oficial de Brasília), com fundamento no § 3º do art. 4º do Decreto nº 10.543, de 13 de novembro de 2020.

Documento assinado eletronicamente por **Antonio Lopes Padilha**, **Pesquisador**, em 12/08/2022, às 17:58 (horário oficial de Brasília), com fundamento no § 3º do art. 4º do Decreto nº 10.543, de 13 de novembro de 2020.

A autenticidade deste documento pode ser conferida no site https://sei.mcti.gov.br/verifica.html, informando o código verificador **10230317** e o código CRC **288A7F8F**.

Referência: Processo nº 01340.005932/2022-74 SEI nº 10230317

"O sucesso nasce do querer, da determinação e persistência em se chegar a um objetivo. Mesmo não atingindo o alvo, quem busca e vence obstáculos, no mínimo fará coisas admiráveis." ".

JOSÉ DE ALENCAR

Ao meu esposo ***Paulo H.****, a meus pais* ***Cecilia*** *e* ***Libardo*** *e à minha irmã* ***Angie***

ACKNOWLEDGEMENTS

I would like to thank my supervisors. To Dr. Padilha, he deserves more than saying thanks. There were six years of privilege and honor to work with someone I admire. Thanks for all your dedication, guidance, understanding and support. I wish you incredible trips, taste the most delicious desserts and happiness in the new stage of your life. To Dr. Lívia for always encouraging me to pursue this dream, for her empathy and support in every situation. I got this challenge standing on the shoulders of giants.

To Dr. Marcelo Banik de Padua, members and collaborators of the GEOMA group for the attention, dedication and help throughout the research. To Dr. Andrea Matos for helping me throughout the research and for motivating me during our long talkings. I acknowledge the personnel of EMBRACE program and Sony Su Chen for supporting the work with magnetometer data. To the Laboratory of Integrated Technologies and Sustainable Engineering (LabTIES) of the Mechanical Engineering Institute of UNIFEI for the computational resources made available.

My sincere thanks to Dr. Adam Shultz, for hosting me in his group at Oregon State University, and Dr. Anna Kelbert, for all her kindness and patience in teaching and supporting my research.

To my husband Paulo H., this work would not have been done without his emotional support. You always made me feel that it was possible. I have no words to describe how grateful I am because you are my life partner, my love.

In memoriam of my grandfather *Milciades Sarmiento*, my *bito*, who passed away during the first year of my doctorate. How I wish you were here today. I can even imagine your words and happiness; you always rejoiced in every achievement.

I am grateful to all of the folks that helped me with my research. To Brazil, my new country and home, to the Brazilian National Institute for Space Research (INPE) and to the postgraduate program in Space Geophysics at INPE, the great opportunity and receptivity. I am grateful to the staff and teachers.

This study was supported by CNPq (141376/2019-8) and PII-CAPES (88887.570889/2020-00) grants. Thanks to these funding agencies for the Ph.D. scholarship and grants, and for their investment in science.

ABSTRACT

Geomagnetically induced currents (GICs) result from the interaction of the temporal variation of the geomagnetic field with the deep electrical resistivity structure of the Earth. These currents can pose hazards to grounded technological systems during major disturbances of the geomagnetic field. A current methodology for simulating GICs in electric power transmission lines during geomagnetic storms was implemented in this thesis to assess potential risks of these currents in Brazilian power networks. It is based on the use of geomagnetic data measured at the surface, 3-D models of the electrical resistivity distribution inside the Earth and knowledge of transmission line engineering parameters. The precise resistances of the network components are unknown and therefore assumptions were made to calculate the GIC fluxes from the derived geoelectric field. This methodology was used to simulate GICs during geomagnetic storms in simplified representations of real power networks in the south-southeast and north-northeast regions of Brazil, affected by the South Atlantic Magnetic Anomaly and the Equatorial Electrojet, respectively. In the south-southeast region, two intense geomagnetic storms in June and December 2015 were chosen and geoelectric fields were calculated by convolution of a 3-D resistivity model derived under the Paraná basin with geomagnetic variations recorded by magnetometers from the EMBRACE program. The largest GICs were modeled in regions of high resistivity concentrated in an isolated substation at the north end of the network and in a cluster of substations in its central part where the E-W oriented transmission lines coincide with the orientation of the estimated geoelectric field. The maximum magnitude of the modeled GIC was 9.08 A during the main phase of the June storm, estimated at a northern substation, while the lowest magnitudes were found over prominent crustal anomalies along the Paraná basin axis and bordering the continental margin. In the north-northeast region, three storms recorded during the operation of a magnetometer array in 1990-1991 were modeled using a 3-D resistivity model derived under the Parnaíba basin. The largest GICs were modeled in substations of a central branch in the E-W direction of the transmission network, located on more resistive blocks of the 3-D model and parallel to the main direction of the estimated geoelectric currents. The maximum magnitude of the modeled GIC at these substations was 6.24 A at one of these central grid stations during an intense storm in November 1990. These simulation results will be used by the EMBRACE to identify optimal substations for installing monitoring sensors measuring real GIC values for validation efforts of the developed methodology.

Keywords: 3-D resistivity model. Geomagnetic storms. Geoelectric field. Power transmission network. GIC modeling.

MODELAGEM DE CORRENTES GEOMAGNETICAMENTE INDUZIDAS EM REDES DE TRANSMISSÃO DE ENERGIA ELÉTRICA NO BRASIL USANDO MODELOS 3-D PARA REPRESENTAR A ESTRUTURA DE CONDUTIVIDADE ELÉTRICA EM SUBSUPERFÍCIE

RESUMO

Correntes induzidas geomagneticamente (GICs) resultam da interação da variação temporal do campo geomagnético com a estrutura de resistividade elétrica profunda da Terra. Essas correntes podem representar perigos para sistemas tecnológicos de grande porte aterrados durante grandes distúrbios do campo geomagnético. Uma metodologia atual para simulação de GICs em linhas de transmissão de energia elétrica durante tempestades geomagnéticas foi implementada nesta tese para avaliar os riscos potenciais dessas correntes nas redes elétricas brasileiras. Baseia-se no uso de dados geomagnéticos medidos na superfície, modelos 3-D da distribuição de resistividade elétrica no interior da Terra e conhecimento de parâmetros de engenharia das linhas de transmissão. Valores precisos das resistências dos componentes da rede não são conhecidos e, portanto, foram feitas suposições para calcular os fluxos GIC a partir do campo geoelétrico obtido. Essa metodologia foi utilizada para simular GICs durante tempestades geomagnéticas em representações simplificadas de redes elétricas reais nas regiões sul-sudeste e norte-nordeste do Brasil, afetadas respectivamente pela Anomalia Magnética do Atlântico Sul e pelo eletrojato equatorial. Na região sul-sudeste, foram escolhidas duas tempestades geomagnéticas intensas ocorridas em junho e dezembro de 2015 e os campos geoelétricos foram calculados por convolução de um modelo de resistividade 3-D derivado sob a bacia do Paraná com variações geomagnéticas registradas por magnetômetros do programa EMBRACE. As maiores GICs foram modeladas em regiões de alta resistividade concentradas em uma subestação isolada na extremidade norte da rede e em um aglomerado de subestações em sua parte central onde as linhas de transmissão orientadas na direção E-W coincidem com a orientação do campo geoelétrico estimado. A magnitude máxima da GIC modelada foi de 9,08 A durante a fase principal da tempestade de junho, estimada em uma subestação da região norte, enquanto as magnitudes mais baixas foram encontradas sobre anomalias crustais proeminentes ao longo do eixo central da bacia do Paraná e margeando a margem continental. Na região norte-nordeste, três tempestades registradas durante a operação de uma malha de magnetômetros em 1990-1991 foram modeladas usando um modelo de resistividade 3-D derivado sob a bacia do Parnaíba. As maiores GICs foram modeladas em subestações de um ramal central com sentido E-W na rede de transmissão, localizado em blocos mais resistivos do modelo 3-D e paralelo ao sentido principal das correntes geoelétricas estimadas. A magnitude máxima da GIC estimada nessas subestações foi 6,24 A em uma dessas estações centrais da rede, durante uma intensa tempestade em novembro de 1990. Esses resultados de simulação serão usados pelo EMBRACE para identificar as subestações ideais para instalação de sensores de monitoramento medindo valores reais de GIC visando esforços de validação da metodologia desenvolvida.

Palavras-chave: Modelo 3-D de resistividade elétrica. Tempestades geomagneticas. Campos geoelétricos. Redes de transmissão de energia. Modelagem de GIC.

LIST OF FIGURES

Page

LIST OF TABLES

Page

LIST OF ABBREVIATIONS

1-D	–	One-dimensional
2-D	–	Two-dimensional
3-D	–	Three-dimensional
AC	–	Alternating Current
ANSI	–	American National Standards Institute
ARV	–	Average Relative Variance
CME	–	Coronal Mass Ejections
DC	–	Direct Current
Dst	–	Disturbance Storm-Time
EEJ	–	Equatorial Electrojet
EM	–	Electromagnetic
EMBRACE	–	Brazilian Studies and Monitoring of Space Weather
FACs	–	Field-Aligned Currents
FERC	–	Federal Energy Regulatory Commission
FFT	–	Fast Fourier Transform
GDS	–	Geomagnetic Deep Sounding
GEOMA	–	INPE's Geomagnetism Group
GICs	–	Geomagnetically Induced Currents
GMD	–	Geomagnetic Disturbances
IEEE	–	Institute of Electrical and Electronics Engineers
IGRF	–	International Geomagnetic Reference Field
IMF	–	Interplanetary Magnetic Field
INPE	–	National Institute for Space Research
INTERMAGNET	–	International Real-time Magnetic Observatory Network
LP	–	Lehtinen and Pirjola
LT	–	Local Time
MCTI	–	Ministry of Science, Technology and Innovation
ModEM	–	Modular System for EM Inversion
MT	–	Magnetotelluric
ON	–	National Observatory
PE	–	Prediction Efficiency
SAMA	–	South Atlantic Magnetic Anomaly
SECS	–	Spherical Elementary Current System
si	–	Sudden Impulse
Sq	–	Solar Quiet
ssc	–	Sudden Storm Commencement
TE-mode	–	Transverse Electric mode
TM-mode	–	Transverse Magnetic mode
UT	–	Universal Time

CONTENTS

1 INTRODUCTION

Modeling geomagnetically induced currents (GIC) helps to understand risks in grounded systems triggered by space weather events such as geomagnetic storms (BOTELER; PIRJOLA, 2017). These induced currents derive from the coupling of multiple non-stationary and transient processes, related to variations in the geomagnetic field observed on the Earth's surface, with stationary and relatively permanent processes, such as the distribution of electrical conductivity within the Earth. The characteristics and location of networks and grounded conductor systems in power transmission networks have an impact as well. Thus, the accuracy in GIC modeling requires monitoring the geomagnetic field and deepening knowledge of the local distribution of the Earth's conductivity to estimate the induced geoelectric field and provide realistic conditions to assess the GIC risk.

A great accuracy in determining these geoelectric fields is one of the most critical objectives in studies related to monitoring and evaluating risks derived from GICs. Because the most significant geomagnetic disturbances (GMD) are observed in regions of high latitudes, these countries have led this area (PIRJOLA, 2000; PULKKINEN et al., 2005; PULKKINEN et al., 2015). Working groups in North America (United States and Canada) and Fennoscandia (Finland, Sweden, and Norway), in the first case encouraged by the Federal Energy Regulatory Commission (FERC) of the United States, were guided to establish requirements for optimal performance of electric power transmission networks during significant GMD. Currently, even middle- and low-latitude countries are concerned about the possible impact of GICs on their grounded technological systems (TRIVEDI et al., 2007; NGWIRA et al., 2008; WATARI et al., 2009; MARSHALL et al., 2012; TORTA et al., 2012; CARABALLO et al., 2013; KELLY et al., 2017). In the case of Brazil, GIC studies were intensified after the creation of its space weather program (EMBRACE) in 2008 at INPE (PADILHA et al., 2008). Using existing scientific capabilities at INPE, this program monitors the Sun and Earth's space environment through different instruments (solar radio telescopes, ionospheric sounders, GNSS receivers, magnetometer array, optical imagers, radiofrequency radars) and also contemplates the impacts of this space environment in ground-based technological systems.

Historically, the estimation of geoelectric field amplitudes used in GIC studies was done using one-dimensional (1-D) conductivity models to represent the Earth's interior. In that cases, the geomagnetic variation is assumed to be a plane wave propagating from space to the Earth's surface and subsurface conductivity is represented

by multiple horizontal layers of different conductivities and thicknesses (i.e. the conductivity inside the Earth varies vertically but not horizontally). This is the basic approach of the magnetotelluric (MT) method and results in horizontal electric and magnetic fields without spatial variation (PIRJOLA, 2002). These were the only models available for large physiographic regions for a long time and were useful in comparison processes as they produced reasonable estimates of the GICs in various regions, even though they did not reflect the values measured in regions with more complex conductivity. In these 1-D models, the subsurface is smoothed by integrating along transmission lines (hundreds of kilometers) without considering crossing regions with different conductivity (VILJANEN et al., 2012; BOTELER, 2015).

In the last decades, with the availability of 3-D inversion programs (MACKIE et al., 2001; SIRIPUNVARAPORN et al., 2005a; EGBERT; KELBERT, 2012) and the increase in MT data acquisition with stations arranged in grid form (KELBERT et al., 2011; DONG et al., 2013; ROBERTSON et al., 2016), 3-D models of a non-uniform Earth (in which the Earth's conductivity varies vertically and horizontally) have become more common. In particular, data availability from the EarthScope project, which obtained MT transfer functions for almost the entire United States, made it possible to carry out several studies comparing local geoelectric fields modeled by transfer functions (impedances) derived from 1-D and 3-D conductivity distributions. It has been shown that estimates of geoelectric magnitudes derived from 1-D models can provide errors of more than one order of magnitude (possibly exceeding two orders of magnitude in some cases) compared to more realistic results derived from 3-D impedances (BEDROSIAN; LOVE, 2015; BONNER; SCHULTZ, 2017; WEIGEL, 2017; CUTTLER et al., 2018; LOVE et al., 2018a; LUCAS et al., 2018). New approaches have also been proposed to estimate the response functions of induced electric currents to estimate GICs that could be used by electric grid operating companies as a real-time GIC risk assessment (INGHAM et al., 2017; KELBERT; LUCAS, 2020). More globally, focusing on strengthening the security of the critical infrastructure of countries, initiatives have been proposed to encourage the study of GICs due to their socio-economic impact (EXEC.ORDER, 2019).

Geoelectric field modeling to derive the amplitude of GICs during magnetic storms in South America has used geomagnetic field variations with 1 min acquisition and 1-D models for the subsurface electrical conductivity distribution (TRIVEDI et al., 2007; CARABALLO et al., 2013; BARBOSA et al., 2015; DIOGO, 2018; ESPINOSA et al., 2019). In Brazil, GICs with amplitudes in the range $15 - 20$ A were measured during the November 2004 geomagnetic storm, with index $Dst = -373$ nT (TRIVEDI

et al., 2007). GIC estimates of about 25 A were modeled during other storms by Barbosa et al. (2015), considering 1-D conductivity models. These currents of tens of amperes are not enough to cause the collapse of a power transmission network, but can still generate unwanted effects by causing substation instruments (mainly power transformers) to operate for prolonged periods outside their ideal regime. In this case, GICs can cause saturation, harmonic generation and consequent decrease in the useful life of this equipment. An aggravating factor is a trend in recent years to build longer transmission lines to transport large amounts of power over greater distances, trying to improve the robustness and capacity of these systems to deliver power and minimize costs in order to obtain more competitive prices. The problem here stems from the increased interconnectivity between different power grids, which significantly increases their vulnerability to the occurrence of GICs (ALVES; PADILHA, 2017). More importantly, there are also induction effects amplifying ground-level electric fields in regions of complex Earth structure (KELBERT, 2020). These factors justify the increased monitoring and analysis of the various parameters involved in the occurrence and modeling of GICs in low- and mid-latitude regions (GAUNT; COETZEE, 2007; MARSHALL et al., 2012).

On the other hand, studies carried out so far in South America have used a magnetic field sampling period of 1 min to model GIC amplitudes (BARBOSA et al., 2015; ESPINOSA et al., 2019). This is known to cause significant attenuation in the estimation of modeled peaks of the surface geoelectric field because the shorter period (higher frequency) geomagnetic signals also contribute to the overall amplitude of the calculated geoelectric field (PULKKINEN et al., 2006; GANNON et al., 2017; GRAWE et al., 2018). The long-term collection of time series of 1 s cadence by fluxgate magnetometers is relatively recent in most magnetic observatories. Consequently, comparisons of geoelectric fields using geomagnetic time series of 1 min and lower periods have only recently been presented (LOVE et al., 2018b), with significant differences observed depending on geomagnetic activity and impedance tensor. More recent measures of GICs with a sampling rate of 0.1 s (WATARI et al., 2021) suggest that samplings intervals of geomagnetic fields shorter than 1-2 s are recommended to extend our understanding of the frequency response of GICs.

1.1 Thesis outline

The main objective of this thesis is to estimate geomagnetically induced currents that may affect electric power transmission lines in Brazil during geomagnetic disturbances, using 3-D models to obtain information about the distribution of subsurface

electrical conductivity. A secondary goal is to implement an operational methodology for the EMBRACE program that can be used in different regions of the country allowing to evaluate potential GIC hazards in the Brazilian power transmission system and locate weak spots in the different grids, more susceptible to the risk derived from these induced currents. At these substations will be installed sensors measuring the real GIC values for further validation efforts of the methodology developed. This methodological procedure involves the interpolation of geomagnetic variations data measured by some stations throughout the region where the GICs are to be calculated, the convolution of these interpolated geomagnetic data with 3-D MT impedances derived from forward calculation of Earth resistivity models in the study region to obtain the surface geoelectric fields and, finally, the combination of these geoelectric fields with engineering parameters and topology of the power transmission networks to simulate the resulting GICs at the nodes (substations) of the grid.

Geomagnetically induced currents were estimated during geomagnetic disturbances in two regions of the Brazilian territory, the south-central region affected by ionospheric particle precipitation in the South Atlantic Magnetic Anomaly (SAMA) and the north-northeast region affected by the diurnal ionospheric currents of the Equatorial Electrojet (EEJ). Underground 3-D resistivity models for both regions were derived through joint inversion of available GDS (Geomagnetic Deep Sounding) array data and sparse MT soundings. South-central Brazil is almost entirely covered by the sedimentary-volcanic package of the Paraná Basin and the induced currents were derived during two geomagnetic storms of solar cycle 24, using high-cadence of geomagnetic variations (1 s) measured by magnetometers of the EMBRACE. The area studied in the north-northeast Brazil covers a large portion of the sedimentary Parnaíba Basin and used geomagnetic data collected during an old GDS survey with acquisition every 1 min that sampled three periods with geomagnetic disturbances in the solar cycle 22.

Chapter 2 presents the theoretical framework associated with the generation of GICs. Section 2.1 describes the physical principles involved in the chain of processes that result in the occurrence of GICs and introduces the methods used to directly measure and indirectly estimate these currents. Section 2.2 describes the conditions of the interplanetary environment acting as a source of GICs and the characteristics of variations in the geomagnetic field observed on the Earth's surface, with emphasis on peculiar phenomena of the geomagnetic field in Brazilian territory. Section 2.3 introduces electromagnetic methods that use natural sources to probe the distribu-

tion of conductivity within the Earth. The MT and GDS methods used in this study to obtain 3-D subsurface resistivity models are briefly presented.

A more detailed description of the methodology used in this work to model GICs in power transmission lines is presented in Chapter 3. The geomagnetic field interpolation method, a brief discussion of the procedure used to invert electromagnetic geophysical data to obtain the distribution of 3-D resistivity and the method used to estimate GICs in power transmission lines are presented. Tests to verify the reliability of the algorithms developed for some of these procedures are also presented.

Chapter 4 shows two case studies of modeling GICs in Brazilian territory. Section 4.1 shows simulations of GICs in a simplified representation of the power transmission network in the low latitude region of south-southeast Brazil. This was the first study in the South American sector that used 3-D conductivity structure information and high-cadence geomagnetic variations to model GICs, helping to identify substations where to install monitoring equipment for future validation efforts. An article discussing the results shown in this section is currently submitted for publication in an indexed journal (ESPINOSA et al., 2022). Similarly, Section 4.2 shows simulations of GICs for the north-northeast region of Brazil, but using geomagnetic data with a cadence of 1 min. Another scientific article with the results of this section is currently being prepared for submission.

The last two chapters discuss the most salient results obtained in this study (Chapter 5) and the conclusions and future work planned to improve and implement the methodology by the EMBRACE program (Chapter 6).

2 THEORETICAL BACKGROUND

2.1 Geomagnetically Induced Currents (GICs)

Transient variations due to interplanetary structures such as flares and coronal mass ejections (CME) from the Sun alter the propagation of the solar wind and cause changes in the magnetosphere. The geomagnetic field carried by the solar wind and the incoming particles intensify the magnetosphere and ionosphere current systems, driving variations of the magnetic field on the Earth's surface, dominated by Ampere's law (Equation 2.1). During geomagnetic disturbances, geomagnetic field variations can reach thousands of nT at auroral latitudes and hundreds of nT at low and mid-latitudes (PULKKINEN et al., 2012).

$$\nabla \times \boldsymbol{B} = \mu_0 \boldsymbol{J} \tag{2.1}$$

The electromagnetic signal, which propagates in all directions, reaches the Earth's surface and is mainly reflected by the transition between an insulating medium air and a conducting medium, the solid Earth, with only a small proportion penetrating the underground. Related to the rate of change of the geomagnetic field and the conductivity distribution inside the Earth, a geoelectric field governed by Faraday's law will be induced in the subsurface (Equation 2.2).

$$\nabla \times \boldsymbol{E} = -\frac{\partial \boldsymbol{B}}{\partial t} \tag{2.2}$$

Generation and propagation of this geoelectric field beneath the Earth are related to changes in the subsurface electric resistivity structure (or its reciprocal conductivity $\bar{\boldsymbol{\sigma}}$). The induced electric field conducts the electric (telluric) currents, expressed in the constitutive relation $\boldsymbol{J} = \bar{\boldsymbol{\sigma}}\boldsymbol{E}$, which are the geomagnetically induced currents. In the case of an electric power transmission line, its grounding points and the Earth's surface form a closed path (Figure 2.1). Between the start and endpoint of each transmission line, for a given length L, an electromotive force that acts as an additional voltage source is induced. It will direct the geomagnetically induced currents along the lines that make up the electric power transmission system (BOTELER; PIRJOLA, 2017).

Figure 2.1 - Schematic of the induced electric field in electric power transmission systems along the closed path formed by the transmission line and the Earth's surface.

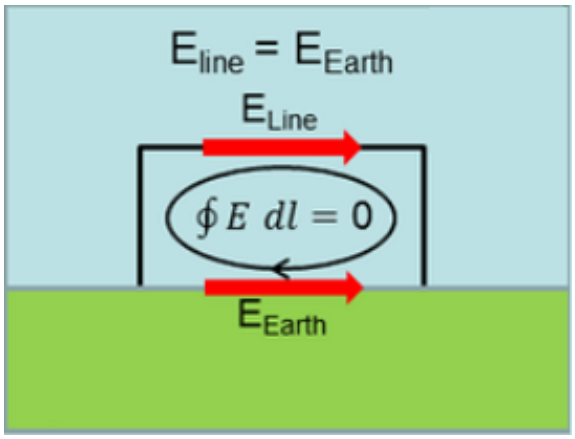

SOURCE: Adapted from Boteler and Pirjola (2017).

Thus, the induced geoelectric field endues the same amplitude and direction as the electric field along the voltage lines and is responsible for the induced currents in the transmission lines (BOTELER; PIRJOLA, 2017). Compared to the operational frequency of electric power transmission grids (frequencies ranging from $50 - 60$ Hz), geomagnetically induced current frequencies are considered quasi-continuous variations (almost DC level) (PIRJOLA, 2007). When the offset is added to the alternating current, the core operating point of the transformer may go into saturation; the distorted waveform produces a harmonic current, which in turn produces local heating and increase reactive power. It compromises the lifetime of the equipment because of the cumulative effects and could even result in an early catastrophic failure (KIRKHAM et al., 2011).

Hall-effect sensors are frequently used to directly monitor GICs, installed at the neutral ground connection of a transformer in a power transmission substation. This device converts the magnetic field generated by the current flowing in the conductor (neutral copper cable) to a voltage proportional to the generated field. Operating in balanced conditions, without GIC, the current flow at the neutral-ground connection of a transformer will be zero. Under unstable conditions, AC and quasi-DC currents (GICs) will be present at the neutral-ground terminal. The AC currents can be filtered out with the knowledge of the typical GIC frequencies (generally $0.001 - 0.1$ Hz).

The indirect method for estimating GIC can be subdivided into two parts: geophysics and power system engineering. The geophysics part uses measurements of magnetic field variations by magnetometers installed in the region where the GIC is to be calculated to obtain a corresponding geoelectric field, using the plane wave model for electromagnetic wave propagation and a geoelectric model of the distribution of electrical conductivity (resistivity) inside the Earth. Next, an engineering model transforms the geoelectric field to GIC on the transmission line. Thereupon, it is necessary to have information about the transmission line that includes substation coordinates, transformer resistances, station grounding, possible reactors, grid topology and configuration (line locations and connections), information about the connections at the stations (auto-transformers, etc.) and the possible presence of series capacitors. GICs are calculated using this data, plus Kirchhoff's charge and energy conservation principles. In this thesis, using the indirect method, the methodology applied to estimate GICs from geomagnetic data is described in Chapter 3.

2.2 GIC sources in the interplanetary medium

In polar regions, geomagnetic field lines merge with the IMF (interplanetary magnetic field) lines, approximating an "open" field line configuration that extends and distorts the magnetic field in the opposite direction to the Sun. The solar wind acts as the sourcing process that modifies the geomagnetic field and leads the flow of momentum and energy to drive a convection motion governed by $\boldsymbol{E} \times \boldsymbol{B}$ (MILAN et al., 2017). In this process, a magnetic field and plasma circulation are established from the magnetosphere and directed toward the ionosphere (GANUSHKINA et al., 2018). Plasma motion, in the convection cycle in the magnetosphere, has an associated electric field in the dawn-dusk ($\boldsymbol{E}_y$) direction, which is mapped along the geomagnetic field lines to the ionosphere (MILAN et al., 2017). Thus, the level of geomagnetic field perturbation recorded on the surface is a function of this electric field in the $\boldsymbol{E}_y$ direction (GONZALEZ et al., 1994). Field-aligned currents (FAC) are fundamental to understanding the energy exchange processes between the ionosphere and the magnetosphere in the so-called "convection circuit" ($solar\ wind - magnetosphere - ionosphere$) because they depend on the intensity of the convection phenomenon in the auroral region of the magnetosphere and the conductance of the ionosphere (MILAN et al., 2017).

The principal characteristic of a geomagnetic storm is the decrease in the horizontal $\boldsymbol{H}$ component of the geomagnetic field, which can last from one to several days. Geomagnetic disturbances result from the passing solar wind effects, intensified by

extreme solar activity (mainly solar flares or CME) and the interaction processes with the magnetosphere, controlled by the convection loop. In general, during a strong magnetic storm, the IMF has a southward component, opposite to the direction of the geomagnetic field (north-south) oriented to the south for sufficiently extended intervals.

2.2.1 Variations of the geomagnetic field

Magnetic disturbances are caused by a sudden increase in the dynamic pressure of the solar wind as high speed and high-density plasma from the Sun suddenly arrive at the Earth. This increase in dynamic pressure compresses the magnetosphere, shrinking its size and pushing it earthward. In this way, all the boundaries and regions of the magnetosphere play important roles in determining the type of magnetic disturbances seen on the ground. The real magnetosphere is extremely complex because of the asymmetric magnetic field with strong gradients in field and plasma in every direction and its dimensions which are continually changing in response to the solar wind (MCPHERRON, 2005). Thereby, at low latitudes the magnetic field response to the solar wind pressure change is often step-like due to the Chapman-Ferraro magnetopause currents and a propagating compressional wave front. Geomagnetic variations at low latitudes can be considered as remote to field-aligned, auroral ionospheric, and equatorial electrojet currents (VICHARE et al., 2014).

An example of sudden changes in the horizontal component of the geomagnetic field is the *si* (*sudden impulse*), commonly associated with the passage of tangential discontinuities of the solar wind (JOSELYN; TSURUTANI, 1990). When this event precedes a storm, it is usually observed as a positive variation in the magnetic field at the Earth's surface (except for high-latitude regions, where negative variations are likely). In a geomagnetic storm, the *si* is identified as *ssc* (*sudden storm commencement*) and marks the beginning of the storm. It is produced by the first impact of the solar wind on the magnetosphere, and it is due to the front compression effect and the increase in the solar wind dynamic pressure. It has been found that a geomagnetic SI at low latitudes is proportional to the change of the square root of the solar wind pressure (VICHARE et al., 2014).

Generically, three well-defined phases are identified during a typical geomagnetic storm: the initial, main, and recovery phases. As the prominent signature during the main phase of the storm, a drastic decrease in the horizontal component of the geomagnetic field is observed. This decrease is more substantial at low latitudes and

can be explained by the intensification of the westward ring current in the inner magnetosphere. This current produces a magnetic disturbance that is southward along the Earth's dipole axis, whereas the geomagnetic field itself is northward (MCPHERRON, 2005). The north-south component of the IMF (GONZALEZ et al., 1994), which results from the magnetosphere's sufficiently strong and long-lived interaction with the IMF of the solar wind, controls the ring current's growth or decay.

Figure 2.2 - Geomagnetic storm phases; Initial, main and recovery phases.

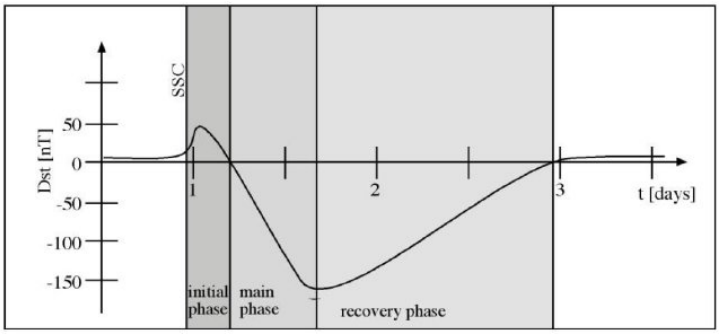

SOURCE: Kasran et al. (2018).

The level of disturbance in the magnetosphere is quantified by geomagnetic indices, which contain information on the geomagnetic activity and the current systems flowing in the solar wind-magnetosphere system. Among the set of indices, the most widely used for characterizing geomagnetically perturbed periods is the *Dst* index, with 1 hour temporal resolution.

The *Dst* is calculated from measurements of the magnetic field at the Earth's surface (4 stations at mid-latitudes) and provides information on the increase or decrease of the ring current. This index is meaningful since, during the main phase, the most significant element of a geomagnetic storm is the ring current's intensification, which is the primary source of disturbance of the magnetic field recorded at the surface for low latitudes. In the case of the *dip equator*, the diurnal amplification of the magnetic field is attributed to the Equatorial Electrojet (EEJ) current system (KIKUCHI; HASHIMOTO, 2016). The storm's intensity is quantified using the *Dst* index, which allows it to be classified as moderate, severe, intense, or great. Table 2.1 shows the classification of magnetic storms using the *Dst* index.

Table 2.1 - Classification of geomagnetic storms according to the Dst index.

Storm type	Dst **range (nT)**
Moderate	$-100 < Dst \leq -50$
Intense	$-200 < Dst \leq -100$
Severe	$-350 < Dst \leq -200$
Great	$Dst \leq -350$

SOURCE: Adapted from Rathore et al. (2012).

2.2.2 Features of the geomagnetic field in Brazil

The Brazilian territory is characterized by two phenomena of the geomagnetic field: the magnetic equator, with diurnal electric currents forming the equatorial electrojet which crosses the country in the north region (FORBES, 1981), and the presence of the South American Magnetic Anomaly (SAMA), with a minimum intensity of the Earth's magnetic field that covers much of the south-southeast region. These conditions cause changes in electrodynamics processes in the ionosphere and are also reflected in the characteristics of the local magnetic field variations observed on the ground.

At the geomagnetic equator, the current system Sq (solar quiet) in the southern and northern hemispheres merge and are enhanced into a current in the E region of the ionosphere. In addition to the Sq current, in the dayside equatorial ionosphere, currents driven by tidal wind through the dynamo mechanism cause an accumulation of charges, which are positive at dawn and negative at dusk terminators, resulting in an eastward electric field along the magnetic equator. In this region, the magnetic field lines are nearly horizontal and northward, orthogonal to the electric field. The dynamo region is bounded by a non-conducting atmosphere below ~ 70 km and by the effectively collisionless plasma above ~ 140 km. Electrons within $\sim 70 - 140$ km drift upward relative to the ions, causing a vertical Hall polarization field, which causes an additional eastward current. An abnormally large Cowling conductivity is thus generated along a narrow channel at the dayside *dip equator*, resulting in enhanced eastward electrical current termed the equatorial electrojet (CHAPMAN, 1951; BAKER; MARTYN, 1953).

The most substantial influence of these electric currents around 100 km altitudes

and approximately 600 km wide centered on the *dip equator* had been studied from different approaches (HESSE, 1982; KANE; TRIVEDI, 1982; PADILHA et al., 1997; PFAFF JR. et al., 1997; RIGOTI et al., 1999; DENARDINI et al., 2005). Moreover, different studies have been carried out in terms of the geomagnetic variations observed on the ground (TRIVEDI et al., 1997; SHINOHARA et al., 1998; ZANANDREA, 1999; PADILHA et al., 2003), which are the most important for GIC generation. These studies provide evidence that amplification of the northward component of a broad spectrum of geomagnetic field variations within a zone of 5° on either side of the geomagnetic equator during geomagnetically quiet days is one of the effects of the increased Cowling conductivity in this region.

During geomagnetically disturbed periods, an alternative model was proposed by Kikuchi and Araki (1979) to explain the diurnal amplification in geomagnetic variations caused by the local increase in the Cowling conductivity in the equatorial region. In the occurrence of interplanetary shocks, magnetospheric compression can increase the magnetospheric-ionospheric current system. The surface waves (Alfvèn) generated by diurnal magnetosphere boundary instabilities (such as Kelvin-Helmholtz instabilities) propagate directly along magnetic field lines into the high-latitude ionosphere, generating large-scale oscillations in ionospheric currents at these latitudes. These high-latitude currents propagate horizontally through the atmosphere to low-latitude regions in a waveguide bounded by the conducting ionosphere and the ground and cause the geomagnetic variations observed at low latitudes. The mechanism is also efficient enough to allow pole waves to travel near-instantaneously to very low latitudes and be amplified suddenly by any localized increase in ionospheric electrical conductivity, such as the increased Cowling conductivity around the *dip equator*.

On the other hand, as a consequence of low magnetic field intensity at SAMA, azimuthally drifting energetic particles trapped in the Earth's inner Van Allen radiation belt come closest to the Earth's surface, interacting with the dense atmosphere and producing enhanced ionization at ionospheric E layer heights (PAULIKAS, 1975). This extra ionization leads to the rise of the ionospheric conductivity, producing conductivity gradient and creating a zonal electric field that changes the way magnetospheric source fields interact with the local ionosphere, such as a pre-existing pattern of geomagnetic disturbance. It will also modify the amplitude of these geomagnetic variations, even during geomagnetically quiet times (ABDU et al., 2005), the sudden impulses at the storm onset, and geomagnetic pulsations during geomagnetically disturbed periods (TRIVEDI et al., 2005; SHINBORI et al., 2010). This

amplification effect at SAMA occurs during the day and at night, more easily identifiable in the latter case. This increment in the amplitude of geomagnetic variations can also influence the amplitudes of geomagnetically induced currents in the Earth subsurface, as suggested by Trivedi et al. (2005).

2.3 The magnetotelluric (MT) method

Electromagnetic (EM) methods use a primary magnetic field that induces electrical currents to flow in conductive rocks within the Earth. These currents drive secondary, measurable EM fields, which allow to get deep and lateral conductivity information over different lithospheric sections. While artificial sources, typically in the frequency range $0.1 - 10$ kHz (ZONGE; HUGHES, 1991), probe only a few kilometers deep in the crust, passive techniques that use natural geomagnetic field variation (frequencies of $10^{-5} - 10^{4}$ Hz (SIMPSON; BAHR, 2005), such as the MT method, allow studies capable of reaching depths of up to hundreds of kilometers.

2.3.1 Natural electromagnetic sources

Two primary natural sources can generate an electromagnetic signal on the Earth's surface. The first, of meteorological origin and with frequencies approximately > 1 Hz, is caused by electrical storms. In this case, the signal comes from lightning activity, mainly in the equatorial region. They give rise to the highest frequency signals related to the reflection of the plane wave in the Earth-ionosphere waveguide. The second source of electromagnetic variation comes from solar wind-magnetosphere interactions (convection circuit) with frequencies below 1 Hz. The amplitude of the variations can reach hundreds of nT due to interactions between the Earth's main magnetic field and the interplanetary magnetic field component. This interaction gives rise to several current systems within the magnetosphere and ionosphere, resulting in the temporal variations of the geomagnetic field recorded on the Earth's surface (SIMPSON; BAHR, 2005).

These natural electromagnetic sources are assumed by the MT method to be plane waves and are modeled as time-varying magnetic fields produced at great distances above the Earth's surface. Most energy is reflected on the Earth's surface because of a high resistivity contrast between the air and the surface. A smaller amount of the EM signal propagates vertically inside the Earth. A flexible dead band, around 0.5 Hz to 5 Hz, extends in the boundary between the variations of the magnetospheric source and those generated by electrical discharges from lightning. In this range of periods (i.e., approximately between $0.2 - 2$ s), the power spectrum of

electromagnetic fields of natural origin presents a minimum. In practical situations, this frequency range with a weaker natural signal leads to a reduction in the data quality of MT soundings due to the decreased signal-to-noise ratio which is dealt with through remote reference processing. Figure 2.3 shows the characteristic power spectrum of natural magnetic variations, emphasizing the reduced signal power in the dead band.

Figure 2.3 - Power spectrum illustrating period characteristics of natural magnetic variations. Inset shows the reduced signal power in the dead band.

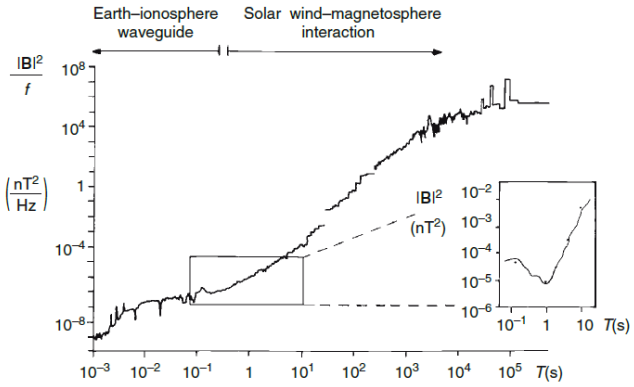

SOURCE: Simpson and Bahr (2005).

2.3.2 Theory of wave propagation inside the Earth

Maxwell's equations describe the propagation and attenuation of EM fields to establish the relationship between spatial and temporal variations of electric and magnetic fields. For an isotropic medium of conductivity σ, magnetic permeability μ and permittivity ϵ three fundamental constitutive relations (Equations 2.3, 2.4 and 2.5) are established:

$$\boldsymbol{B} = \mu \boldsymbol{H} \tag{2.3}$$

$$\boldsymbol{D} = \epsilon \boldsymbol{E} \tag{2.4}$$

$$\boldsymbol{J} = \sigma \boldsymbol{E} \tag{2.5}$$

where:
$\boldsymbol{H}$ the magnetic field vector in amperes per meter (A/m);
$\boldsymbol{B}$ is the magnetic induction vector in weber per square meter (Wb/m^2);
$\boldsymbol{D}$ the electric displacement field vector in coulombs per square meter (C/m^2);
$\boldsymbol{E}$ the electric field intensity vector in volts per meter (V/m);
$\boldsymbol{J}$ the electric current density vector in amperes per meter (A/m);
μ the magnetic permeability in henry per meter (H/m);
ϵ the electrical permittivity, in farad per meter (F/m);
σ the conductivity of the medium in siemens per meter (S/m) (the resistivity $\rho = 1/\sigma$ in Ωm is also often used).

Since the variation of electric permittivity and magnetic permeability for most rocks is minimal compared to electrical conductivity, the free space values ($\mu \approx \mu_0 = 4\pi \times 10^{-7}$ H/m and $\epsilon \approx \epsilon_0 = 8.854 \times 10^{-12}$ F/m) are assumed. Then, electromagnetic field propagation can be written using Maxwell's equations in differential form as:

$$\nabla \times \boldsymbol{E} = -\frac{\partial \boldsymbol{B}}{\partial t} \tag{2.6}$$

$$\nabla \times \boldsymbol{B} = \mu_0 \epsilon_0 \frac{\partial \boldsymbol{E}}{\partial t} + \mu_0 \sigma \boldsymbol{E} \tag{2.7}$$

$$\nabla \cdot \boldsymbol{E} = \rho / \epsilon_0 \tag{2.8}$$

$$\nabla \cdot \boldsymbol{B} = 0 \tag{2.9}$$

The theory of electromagnetic induction considers that electric and magnetic fields propagating inside the Earth exhibit temporal variations sufficiently slow to be considered quasi-static in their spatial distribution (CAGNIARD, 1953). When an electromagnetic signal diffuses through a conductive medium, Equations 2.6 (Faraday) and 2.7 (Ampere) govern the propagation of the electric and magnetic fields. Thus, Equations 2.6 to 2.9 can be rearranged to produce expressions to extract information

about the subsurface.

Derivation of the mathematical expressions used by the MT method requires some important assumptions about the source signal and the nature of electrical conduction on Earth. These are:
1. It is assumed that the electromagnetic signals are generated by magnetic sources located at distances approaching infinity. As a consequence, electromagnetic signals can be treated as uniform plane waves that propagate vertically downwards onto the Earth's surface. A plane electromagnetic wave with amplitude E_0 and B_0 at the surface and angular frequency ω is then given by:

$$\boldsymbol{E} = \boldsymbol{E}_0 e^{i\omega t} \tag{2.10}$$

$$\boldsymbol{B} = \boldsymbol{B}_0 e^{i\omega t} \tag{2.11}$$

2. In Earth materials, the relatively low frequencies of electromagnetic fields used by the MT method do not induce significant displacement currents relative to conduction currents. Displacement currents can then be neglected in Equation 2.7 which becomes:

$$\nabla \times \boldsymbol{B} = \mu_0 \sigma \boldsymbol{E} \tag{2.12}$$

3. The conductivity contrast between two adjacent media (multidimensional Earth) causes accumulation of charges at the interface between them (conductivity gradients) to ensure the principle of continuity inside the Earth (JIRACEK, 1990). This is expressed by an equation derived by taking the divergence of Equation 2.5 and solving for electric charge density q using Equation 2.8:

$$q = -\frac{\epsilon_0}{\sigma} \boldsymbol{E} \cdot (\nabla \sigma) \tag{2.13}$$

2.3.3 The skin depth

For a homogeneous, isotropic medium with non-zero conductivity ($\sigma > 0$), and assuming a time variation of the form $e^{i\omega t}$, Maxwell's equations produce Helmholtz equations for the difusion of electric and magnetic fields:

$$(\nabla^2 - \boldsymbol{\kappa}^2)\boldsymbol{E} = 0 \tag{2.14}$$

$$(\nabla^2 - \boldsymbol{\kappa}^2)\boldsymbol{B} = 0 \tag{2.15}$$

These diffusion equations have the following simplified solutions:

$$\boldsymbol{E} = \boldsymbol{E}_0{}^{-i\boldsymbol{\kappa}z} \tag{2.16}$$

$$\boldsymbol{B} = \boldsymbol{B}_0{}^{-i\boldsymbol{\kappa}z} \tag{2.17}$$

where $\boldsymbol{E}_0$ and $\boldsymbol{B}_0$ are the electromagnetic fields at the Earth's surface, z indicates vertical propagation and $\boldsymbol{\kappa}$ is the complex wave number given by $\boldsymbol{\kappa}^2 = i\omega\mu_0\sigma$. Then,

$$\boldsymbol{\kappa} = \sqrt{i\omega\mu_0\sigma} = \sqrt{i}\sqrt{\omega\mu_0\sigma} = \frac{1+i}{\sqrt{2}}\sqrt{\omega\mu_0\sigma} = (1+i)\sqrt{\frac{\omega\mu_0\sigma}{2}} \tag{2.18}$$

The real component of the propagation constant $\boldsymbol{\kappa}$ can be written as

$$\delta = \sqrt{\frac{2}{\omega\mu_0\sigma}} \approx 500\sqrt{\rho T} \tag{2.19}$$

where δ is known as the *skin depth* (in meters). It describes the depth at which an inducing magnetic field decays in amplitude to $1/e$ of its surface amplitude, approximately 37 % of its initial amplitude.

Note that *skin depth* depends on the frequency ω (or the period T) and the conductivity σ of the medium. As the frequency and conductivity increase, δ decreases. This means that surveys in more resistive media tend to map deeper depths (EVANS, 2012). Similarly, the lower the frequency, the lower the signal attenuation, and consequently, the greater the depth reached. This parameter is important because it provides proxy estimates of the depth of investigation, related only to the medium parameters (conductivity σ and permittivity μ_0) and the signal frequency (ω). It also demonstrates that altering the frequency of the signal aids in determining the differences in conductivity within the Earth (higher frequency signals survey shallower

depths, and lower frequency signals survey greater depths).

2.3.4 Apparent resistivity and phase

Expanding the curl operator in Equation 2.6 for three-dimensional Cartesian coordinates gives the following relationships between electric and magnetic fields:

$$\frac{\delta E_z}{\delta y} - \frac{\delta E_y}{\delta z} = -i\omega B_x \tag{2.20}$$

$$\frac{\delta E_x}{\delta z} - \frac{\delta E_z}{\delta x} = -i\omega B_y \tag{2.21}$$

$$\frac{\delta E_y}{\delta x} - \frac{\delta E_x}{\delta y} = -i\omega B_z \tag{2.22}$$

A key assumption of the MT method is that the magnetic source signals behave as plane waves vertically incident on the Earth's surface. Since this B-field signal propagates vertically downward, induced E-field signals do not have a vertical component ($E_z = 0$). Another implication of the plane wave assumption is that the B-field also does not have vertical component for the Earth approximated by a conducting half-space with a plane surface ($B_z = 0$). Therefore, $\delta E_x/\delta y = \delta E_y/\delta x = 0$. Applying these assumptions to Equation 2.20 and using Equations 2.16 and 2.17 gives:

$$-\frac{\delta E_y}{\delta z} = \boldsymbol{\kappa} E_{y0} e^{-\boldsymbol{\kappa} z} = -i\omega B_x = -i\omega B_{x0} e^{-\boldsymbol{\kappa} z} \tag{2.23}$$

The magnetotelluric impedance $\boldsymbol{Z}$ (in V/A) is then defined as the ratio of the electric and magnetic fields measured at the surface:

$$\boldsymbol{Z}(\omega) = \frac{E_{y0}}{B_{x0}} = -\frac{i\mu_0\omega}{\boldsymbol{\kappa}} = -\frac{i\mu_0\omega}{\sqrt{i\omega\mu_0\sigma}} = -\sqrt{\frac{\mu_0\omega}{\sigma}}\sqrt{i} \tag{2.24}$$

The apparent resistivity ρ_a of the half-space in units of Ωm at a given angular frequency ω can be derived by rearranging Equation 2.24:

$$\rho_a(\omega) = \frac{1}{\mu_0\omega} \left|\boldsymbol{Z}(\omega)\right|^2 \tag{2.25}$$

The apparent resistivity is equivalent to the average electrical resistivity of the Earth over a hemispherical volume with a radius of one skin depth. Moreover, in the frequency domain $\boldsymbol{Z}(\omega)$ is a complex number and has an associated phase ϕ

$$\phi(\omega) = arg\boldsymbol{Z} = tan^{-1}\left(\frac{\Im Z}{\Re Z}\right) \tag{2.26}$$

where $\Im Z$ and $\Re Z$ are the imaginary and real parts of the complex impedance, respectively. In a homogeneous half-space the phase of the magnetic field lags the orthogonal electric field by 45°.

2.3.5 MT impedance tensor

In a homogeneous half-space, measuring the transfer function of a pair of orthogonal electric and magnetic fields at a single frequency would be sufficient to estimate the apparent resistivity. A layered half-space would again require a single transfer function, but measured at several frequencies to estimate apparent resistivity as a function of depth. This is because in a one-dimensional domain, where resistivity varies only with depth, the transfer function of one orthogonal pair, say B_x and E_y, is equal and opposite in sign to the transfer function of the other pair, B_y and E_x. When resistivity varies in two or three spatial dimensions, both pairs of orthogonal electric and magnetic fields must be measured at several frequencies. In such situations, all B-field and E-field components are coupled and the MT impedance is now expressed as a tensor that links the horizontal components of these fields:

$$\begin{pmatrix} \boldsymbol{E}_x(\omega) \\ \boldsymbol{E}_y(\omega) \end{pmatrix} = \frac{1}{\mu_0} \begin{pmatrix} \boldsymbol{Z}_{xx} & \boldsymbol{Z}_{xy} \\ \boldsymbol{Z}_{yx} & \boldsymbol{Z}_{yy} \end{pmatrix} \begin{pmatrix} \boldsymbol{B}_x(\omega) \\ \boldsymbol{B}_y(\omega) \end{pmatrix} \tag{2.27}$$

Each component of the impedance tensor has apparent resistivity ρ_a and phase ϕ given by:

$$\rho_{aij}(\omega) = \frac{1}{\mu_0 \omega} \left|\boldsymbol{Z}_{ij}(\omega)\right|^2 \tag{2.28}$$

$$\phi_{ij}(\omega) = tan^{-1}\left(\frac{\Im \boldsymbol{Z}_{ij}(\omega)}{\Re \boldsymbol{Z}_{ij}(\omega)}\right) \tag{2.29}$$

where the subscripts i and j are indices for the rows and columns of the impedance tensor.

2.3.6 Vertical magnetic transfer function

For the MT method, the horizontal components of the electric field and all three orthogonal components of the magnetic field are measured at the Earth's surface. Thus, in addition to the impedance elements derived from the horizontal components of the electric and magnetic fields, other transfer functions involving the vertical magnetic field can also be defined.

Since lateral variations in Earth resistivity create vertical magnetic fields, the ratio of the vertical component to the horizontal components of the B-field can be used to depict lateral resistivity boundaries. This relationship is employed by the geomagnetic depth sounding (GDS) technique, which defines a dimensionless complex transfer function $\boldsymbol{T}$ relating the amplitude and phase of the horizontal inducing field and the vertical anomalous induced field for a given frequency ω. Such a relationship is written as:

$$\boldsymbol{B}_z = \boldsymbol{T}_{zx}\boldsymbol{B}_x + \boldsymbol{T}_{zy}\boldsymbol{B}_y \tag{2.30}$$

For a laterally uniform resistive Earth and with a horizontal source field, there is no anomalous induced $\boldsymbol{B}_z$ field and $\boldsymbol{T} = 0$. Close to a boundary between low and high resistivity structures, there is a strong $\boldsymbol{B}_z$ field and $\boldsymbol{T}$ is correspondingly large.

Induction arrows are a graphical representation of the GDS transfer function components $\boldsymbol{T}_{zx}$ and $\boldsymbol{T}_{zy}$. These have a real $(in{-}phase)$ and a quadrature $(out{-}of{-}phase)$ part, with arrow lengths of the real (M_r) and quadrature (M_i) given by:

$$M_r = \sqrt{\Re T_{zx}^2 + \Re T_{zy}^2} \qquad\qquad M_i = \sqrt{\Im T_{zx}^2 + \Im T_{zy}^2} \tag{2.31}$$

Orientation of the arrows is similarly determined by:

$$\theta_r = tan^{-1}\left(\frac{\Re T_{zy}}{\Re T_{zx}}\right) \qquad\qquad \theta_i = tan^{-1}\left(\frac{\Im T_{zy}}{\Im T_{zx}}\right) \tag{2.32}$$

where θ_r and θ_i are the orientations for the real and quadrature induction arrows,

respectively. These angles are plotted clockwise from the x-direction.

When plotted on a map, the magnitudes and directions of the induction arrows provide information about the lateral variation in subsurface resistivity. Using the Parkinson convention (PARKINSON, 1962) to plot the arrows involves the reversal of the real component, which results in arrows pointing toward regions of high conductance and away from regions of low conductance. It should be noted that the GDS transfer functions do not have depth sensitivity, but are a useful tool of investigating MT data in cases where 3-component magnetometer information is recorded. GDS information can also be incorporated into 3-D inversion algorithms in addition to the impedance tensor.

2.3.7 MT inversion

The transfer functions obtained from MT measurements can be transformed into resistivity depth models by inversion methods. Inversion theory deals with estimating model parameters (e.g. electrical resistivity) to approximate subsurface geological structures from geophysical data measured at the surface. This is achieved by iteratively changing these model parameters so that the synthetic observations calculated from the underground models approach the measured data. A fundamental part of any inversion is therefore the solution of the "*forward problem*", i.e. the computation of synthetic data from a given underground model. Forward modeling is essentially done by solving the laws of physics connecting subsurface properties with observed properties (Maxwell Equations 2.6 to 2.9 and constitutive relations 2.3 to 2.5). This approach produces a single, unique solution for a given subsurface model. On the other hand, the inversion problem is non-unique because for any set of observations there is a range of different models that can reproduce the observations with the same degree of precision. This is further complicated by the fact that geophysical observations are always contaminated by noise and MT data are often sparsely distributed and available only at the Earth's surface.

All forward and inverse modeling presented in this thesis uses ModEM3DMT, a freely available 3-D inversion code developed by Egbert and Kelbert (2012) and Kelbert et al. (2014) at Oregon State University, USA. The software package uses a nonlinear conjugate gradient scheme to minimize an objective functional formulated in the least squares sense. The algorithm attempts to find a spatially smoothly varying resistivity model, preferably similar to the prior model, which also predicts the measured data within the uncertainty of the estimated data. A roughness function describing the degree of structural variation present in a model is also included in

the inversion procedure. Like other gradient-based algorithms, a local rather than a global minimum of the objective function will generally be achieved. The objective functional ($\boldsymbol{\Phi}$) to be minimized then consists of data misfit and model regularization given by (EGBERT; KELBERT, 2012):

$$\boldsymbol{\Phi} = (\boldsymbol{d} - \boldsymbol{f}(\boldsymbol{m}))^T \boldsymbol{C}_d^{-1} (\boldsymbol{d} - \boldsymbol{f}(\boldsymbol{m})) + \lambda (\boldsymbol{m} - \boldsymbol{m}_0)^T \boldsymbol{C}_m^{-1} (\boldsymbol{m} - \boldsymbol{m}_0) \tag{2.33}$$

where $\boldsymbol{d}$ is the experimental data, $\boldsymbol{m}$ is the earth resistivity model parameter, $\boldsymbol{m}_0$ is the a priori model parameter, $\boldsymbol{f}(\boldsymbol{m})$ is the forward functional mapping, $\boldsymbol{C}_d$ is the data covariance matrix, and $\boldsymbol{C}_m$ is the model covariance matrix. Note that the model covariance matrix is often defined by $\boldsymbol{C}_m^{-1} = \boldsymbol{D}^T \boldsymbol{D}$, with $\boldsymbol{D}$ being, for example, the derivative operator. However, ModEM3DMT builds the model covariance matrix through a recursive autoregressive scheme (KELBERT et al., 2014). The trade-off between data misfit and model regularization is controlled by the parameter λ. ModEM3DMT uses a scheme where, during initial iterations, a relatively high λ parameter is used, but is reduced when the change in misfit becomes less than a predefined threshold value between subsequent iterations.

The misfit between the measured data ($\boldsymbol{d}$) and the predicted data ($\boldsymbol{f}$) of a given resistivity model is given by a normalized rms (root mean square):

$$rms = \sqrt{\frac{1}{N} \sum_{i=1}^{N} \left(\frac{d_i - f_i}{\Delta d_i} \right)^2} \tag{2.34}$$

where N is the number of data points and Δd_i is the prescribed uncertainty for the i_{th} data. Thus, rms equals unit means that the model predicts the measured data exactly within the prescribed uncertainties, on average. Δd_i is the largest of the uncertainty derived from the measurements (normally 95% confidence intervals) and a selected error floor.

3 METHODOLOGY

This chapter provides more details on the methodology applied in this work to estimate GICs, showing some examples used as validation tests at each stage. The following block diagram describes the different steps of the implemented procedure (Figure 3.1) and used generically in two regions of Brazil. The experimental data (GDS and MT) constitute the input parameters to derive the 3-D subsurface resistivity distribution by a data inversion method, later used to obtain the impedance tensor at any location through forward modeling. In both cases, the $ModEM3DMT$ package was used for forward modeling and 3-D inversion of the measured data. Furthermore, the measured geomagnetic variations were interpolated at any point within the study region using SECS to allow projecting the magnetic field variations on the impedance tensor $\bar{\boldsymbol{Z}}_{ij}$ and thus estimating the geoelectric field $\boldsymbol{E}(t)$. Finally, this geoelectric field was used to estimate the GIC magnitudes in power transmission lines following the Lehtinen & Pirjola method.

Figure 3.1 - Flowchart of the methodology used to calculate GICs. Input variables are represented by green boxes, processing functions by white boxes and process data by yellow boxes.

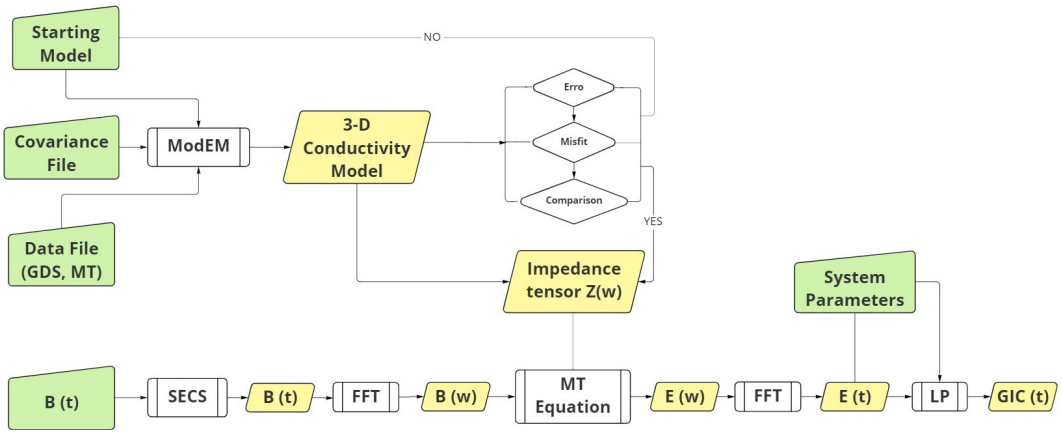

SOURCE: Author production.

3.1 SECS method for geomagnetic field interpolation

The Spherical Elementary Current System (SECS) is a suitable approach to obtain variations of the geomagnetic field at the Earth's surface as a function of a system

of equivalent currents in the ionosphere (AMM, 1997; AMM; VILJANEN, 1999). In this method, the ionosphere is considered a thin two-dimensional spherical shell of radius R, in which a horizontal surface electric current density $\boldsymbol{J}(r)$ flows (PULKKINEN et al., 2003). Considering the current density vector field (J), one can apply Helmholtz's theorem and rewrite it in terms of its curl-free ($\boldsymbol{J}_{cf}$) and divergence-free ($\boldsymbol{J}_{df}$) components (AMM, 1997):

$$\boldsymbol{J}(r) = \boldsymbol{J}_{cf} + \boldsymbol{J}_{df} \tag{3.1}$$

The equivalent current system is composed of field-aligned currents (FACs), which are compensated by currents uniformly distributed and flowing over the surface of the ionosphere (Figure 3.2).

Figure 3.2 - Representation of the equivalent ionosphere current systems used in the SECS method.

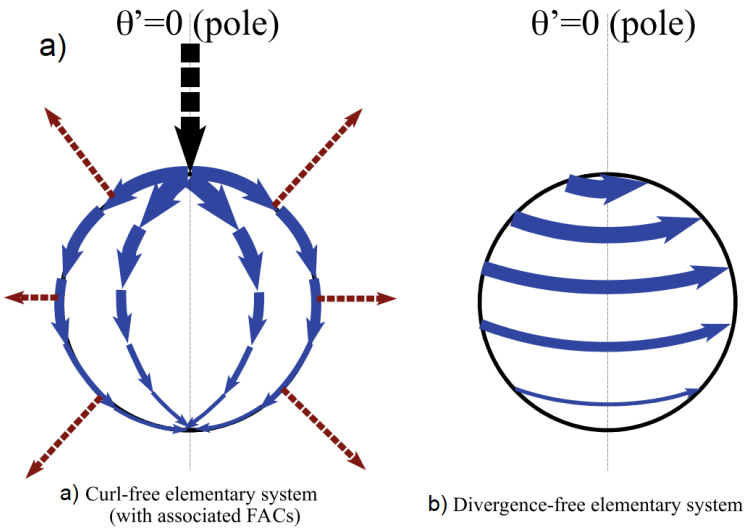

SOURCE: Vanhamäki and Juusola (2020).

The current density $\boldsymbol{J}_{cf}$ is irrotational and has associated an aligned fundamental current, of magnitude $\boldsymbol{I}_{cf}$, at its pole (Figure 3.2a). This current flows in the opposite direction to the distributed aligned currents to ensure that the network of currents associated with the FACs in the ionosphere system is zero (PULKKINEN et al., 2003). However, currents associated with the current density $\boldsymbol{J}_{df}$ form a uni-

formly distributed rotational current throughout the surface of the ionosphere and create a poloidal magnetic field (Figure 3.2b).

For a spherical coordinate system (r, θ, ϕ), the current density can be written in terms of Equations 3.2 and 3.3 below. With R representing the radius of the ionosphere, where the elementary systems are placed, measured from the center of the Earth, and I the equivalent system current amplitudes, called scale factors (AMM, 1997; AMM; VILJANEN, 1999), these equations in spherical coordinates express the current distribution at the ionosphere surface:

$$\boldsymbol{J}_{cf} = \frac{\boldsymbol{I}_{cf}}{4\pi R} cot(\theta/2) \tag{3.2}$$

$$\boldsymbol{J}_{df} = \frac{\boldsymbol{I}_{df}}{4\pi R} cot(\theta/2) \tag{3.3}$$

In a simplified geometry, $cot(\theta/2) \approx (2/\theta)$ and $R\theta \approx \rho$, the Equations 3.2 and 3.3 can be rewritten in cylindrical coordinates (ρ, ϕ, z), considering $\rho = 0$ to coincide with the position of the elementary current system (pole). In this case in cylindrical coordinates, the surface current density of the equivalent current system with amplitude $\boldsymbol{I}$, height $h = 100$ km and considering the distances in the Cartesian coordinate system $x(north - south), y(east - west)$ to determine $\rho = \sqrt{x^2 + y^2}$ will be given by (PULKKINEN et al., 2003):

$$\boldsymbol{J}_{cf} = \frac{\boldsymbol{I}_{cf}}{2\pi\rho} \tag{3.4}$$

$$\boldsymbol{J}_{df} = \frac{\boldsymbol{I}_{df}}{2\pi\rho} \tag{3.5}$$

The irrotational currents associated with the density $\boldsymbol{J}_{cf}$ are poloidal. They do not generate a magnetic field below the ionosphere, while the solenoidal component $\boldsymbol{J}_{df}$ considered in Equation 3.5 generates a poloidal magnetic field $\boldsymbol{B}$ (Equation 3.6). It constitutes the equivalent current density capable of producing the same continuation effect on the magnetic field perturbation below the ionosphere relative to real three-dimensional current systems (BERNHARDI et al., 2008).

$$\boldsymbol{B}(\rho) = \frac{\mu_0 \boldsymbol{I}}{2\pi\rho}\left(1 - \frac{h}{\sqrt{\rho^2 + h^2}}\right) \tag{3.6}$$

3.1.1 Interpolation of the magnetic field from the equivalent current systems

The procedure for interpolation starts with calculating the equivalent current system within the ionosphere associated with the magnetic fields measured at the surface. Once the current system is defined, it can be used to calculate the magnetic field at any point on the Earth's surface within the area where the equivalent currents are defined. The horizontal magnetic fields ($\boldsymbol{B}_x, \boldsymbol{B}_y$) are obtained from the linear Equation 3.7. This equation fits the horizontal magnetic field $\boldsymbol{B}$, produced by the equivalent current system, with the horizontal magnetic field measured in observatories.

$$\boldsymbol{B} = \boldsymbol{M}\boldsymbol{I} \tag{3.7}$$

where $\boldsymbol{M}$ is given by:

$$\boldsymbol{M} = \frac{\mu_0}{2\pi\rho}\left(1 - \frac{h}{\sqrt{\rho^2 + h^2}}\right) \tag{3.8}$$

Each element in Equation 3.7 is decomposed in the form shown in Equation 3.9.

$$\begin{bmatrix} \boldsymbol{B}_j(x_i, y_i) \\ . \\ . \\ \boldsymbol{B}_j(x_N, y_N) \end{bmatrix} = \begin{bmatrix} \boldsymbol{M}_{j,11} & ... & \boldsymbol{M}_{j,1K} \\ . & & . \\ . & & . \\ \boldsymbol{M}_{j,N1} & ... & \boldsymbol{M}_{j,NK} \end{bmatrix} \begin{bmatrix} \boldsymbol{I}_1 \\ . \\ . \\ \boldsymbol{I}_K \end{bmatrix} \tag{3.9}$$

where the column vector $\boldsymbol{B}_j(x_i, y_i)$ corresponds to the j temporal records of the magnetic field in the N observatories, measured at locations given by x_i and y_i. The components of the matrix $\boldsymbol{M}_{j,il}$ are obtained from geometric proportionality factors (Equation 3.8), where ρ is the radial distance calculated between each observatory with records and the point where the amplitudes of the equivalent currents (poles) in the ionosphere will be calculated. Finally, the vector $\boldsymbol{I}_K$ represents the amplitude

of the equivalent current at each pole (BERNHARDI et al., 2008).

Thus, the initial problem is calculating the amplitude of the equivalent current system (Equation 3.6) using the available magnetic field records. The $\boldsymbol{B}_x$ and $\boldsymbol{B}_y$ components are then calculated using the equivalent current system at each site where magnetic field variations are evaluated.

$$\boldsymbol{I} = \boldsymbol{M}^{-1}\boldsymbol{B} \tag{3.10}$$

Note that the linear system is indeterminate because the number of observatories is less than the number of poles. Therefore, it is necessary to use the Singular Value Decomposition (SVD) method to obtain an expression for the matrix $\boldsymbol{M}$, which allows the calculation of the equivalent current amplitudes $\boldsymbol{I}_K$ (JUUSOLA et al., 2006). Furthermore, taking the inverse of singular values below a finite positive threshold to zero guarantees that the positive-definite requirement for matrix inversion is satisfied. This regularization method also eliminates higher-frequency information in the final interpolation (RIGLER et al., 2019).

3.1.2 Test of the algorithm developed applying SECS

The equations described in the previous section were applied to calculate $\boldsymbol{B}_x$ and $\boldsymbol{B}_y$ components at Kakioka station, Japan, as an example. The modeled region (Figure 3.3) encompasses an area of $21° \times 21°$, on a grid of equivalent current poles (8×8, 64 *poles*). This area was chosen due to the quality of accessible geophysical data, which allowed an efficient test of the computational method. The grid poles were uniformly dispersed to enable optimal coverage of the study zone, with the ionosphere considered at a height of 100 km from the surface and the estimated distance between adjacent poles being 333.4 km. In this test, the magnetic field records correspond to the severe storm of March 17, 2015 ($Dst = -223$ nT). Magnetic field data provided by the Kakioka Magnetic Observatory (http://www.kakioka-jma.go.jp/obsdata/metadata/en) for the Kakioka (KAK $36.23°N, 140.18°E$), Memambetsu (MMB $43.91°N, 144.18°E$) and Kanoya (KNY $31.42°N, 130.88°E$) geomagnetic stations were considered. The values measured for the additional station Chichijima (CBI $27.09°N, 142.18°E$) were compared to those generated by the SECS interpolation method for that same station. The effectiveness of the field disturbance prediction can thus be evaluated using the $\boldsymbol{B}_x$ and $\boldsymbol{B}_y$ components.

Figure 3.3 - The 64-pole grid in the ionosphere used to obtain the equivalent current system (SECS method) from three reference observatories (red) to interpolate the magnetic field at a test observatory (green) in Japan.

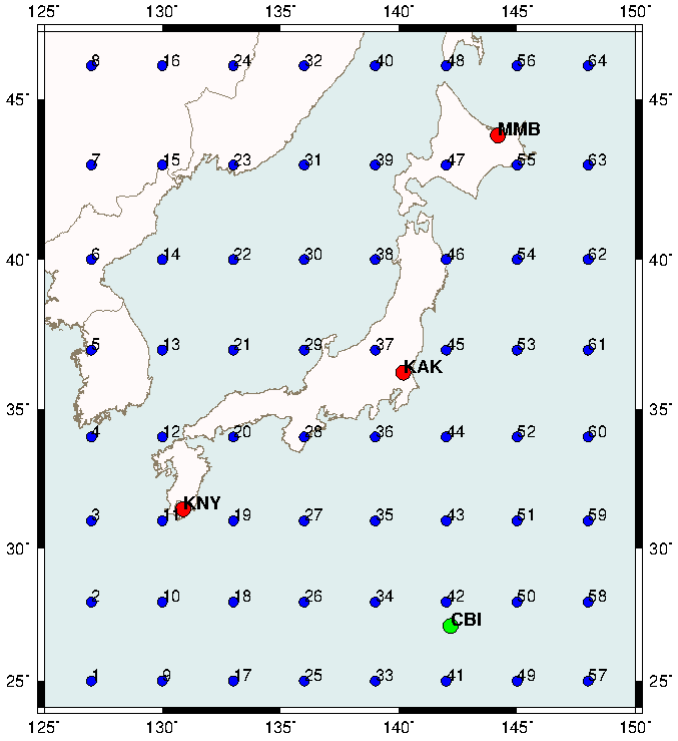

SOURCE: Author production.

A comparison of the magnetic field variations observed on the surface with those calculated by the SECS method at the CBI station is presented in Figure 3.4. Some authors (WEIGEL, 2017; KELBERT et al., 2017) define the prediction efficiency by the dimensionless equation $PE = 1 - ARV$, where 1 is the perfect prediction, and ARV (average relative variance) is defined by Equation 3.11. The variance can be calculated using the measured records t, the interpolation results p, and the variance of the measurement series σ_t, as follows:

$$ARV = \frac{\frac{1}{N}\sum_{i=1}^{n}(p_i - t_i)^2}{\sigma_t^2} \tag{3.11}$$

Figure 3.4 - Comparison of the B_x and B_y components of the magnetic field obtained from the SECS method with the data measured at the CBI magnetic station in Japan.

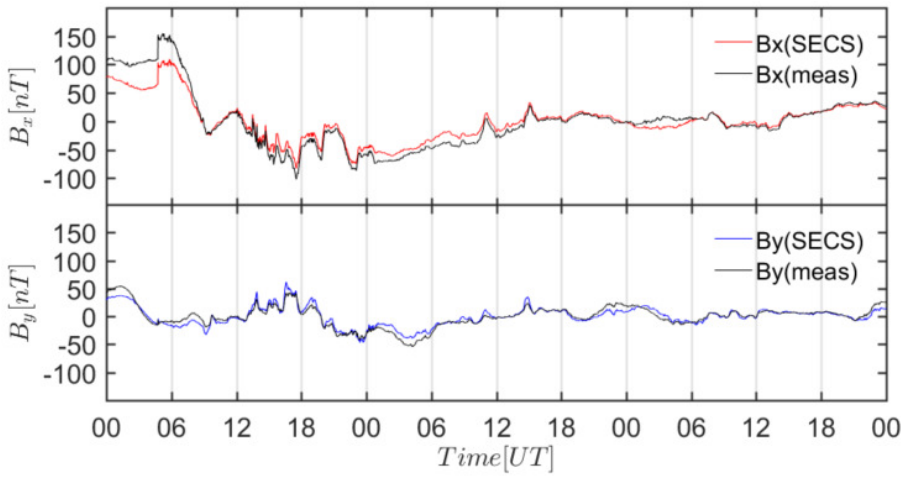

SOURCE: Author production.

In this test, the $\boldsymbol{B}_x$ component generated a $PE \approx 0.89$, while the $\boldsymbol{B}_y$ $PE \approx 0.87$. Once the equivalent current system results from strictly external perturbation sources (calculated for the ionosphere at $h = 100$ km), geomagnetic field records at locations separated by distances greater than 100 km should generally be expected to show significant variation (LOVE et al., 2018a). A threshold of 38% of the maximum singular value was used to obtain the most reliable interpolation over the considered geomagnetic storm. This SVD's criteria automatically excludes those critical components that do not contribute to a solution that best matches the available observations (RIGLER et al., 2019). The result obtained was acceptable, although the construction of grids with better resolution is considered in the following case study in southern Brazil (Subsubsection 4.1.2.1). The greater advantage of using SECS is that the reference stations do not have to be uniformly distributed on the grid, which allows applying it in most real situations with the current distribution of stations in South America. On the other hand, it should be emphasized that equivalent current systems are quite useful for reproducing geomagnetic disturbances at the surface since, in the interpolation process, it is not necessary to know the origin of the currents. However, the equivalent current system is not a real system and, therefore, should be used with care to infer the real current systems in the ionosphere.

In practice, as GMD reflect a highly complex process of magneto-hydrodynamic waves in the ionosphere that give rise to these geomagnetic variations seen at ground level, SECS may not properly simulate them. Additionally, SECS can introduce a coarse spatial smoothing filter that can bypass the true complexity of ground-level inducing magnetic fields. This is because the vertical scale length of ionospheric current systems extends from approximately 100 km above ground level to hundreds of km, while the scale length for induced fields in the Earth's interior within the frequency band of interest is several hundreds of km. Thus, the infinitely thin layer approximation at 100 km above the Earth's surface may imposes certain simplifications and restrictions. In the end, SECS interpolation is essentially just a method for generating potential geomagnetic fields and it must constantly be adapted to increase its value for tracking GIC-related geomagnetic disturbances.

3.2 Inversion and forward calculation using *ModEM3DMT*

A modular system of parallel computer codes for inversion of electromagnetic geophysical data was developed at Oregon State University, commonly referred to as ModEM (EGBERT; KELBERT, 2012; KELBERT et al., 2014). The code is structured as a flexible system, adaptable to a variety of EM geophysical data types and supports a range of inverse problem solution strategies and regularization models. A version of the code suitable for 3-D modeling and inversion of MT and GDS was made freely available for academic use, called ModEM3DMT, and was used throughout this thesis.

Generally, ModEM3DMT penalizes smoothed deviations from a prior model. Deviations are penalized with a spatial covariance where small-scale features are more heavily penalized. Choosing the best covariance is a trade-off between fitting the data well and creating a geologically plausible model. The program is run by a command-line interface that controls the program's various options and specifies the required and optional input and output files. These include the format of input data files, model files, model covariance file, and forward and inversion modeling options. Description of these options and files for performing the most common modeling and inversion tasks are provided in the user manual (EGBERT et al., 2016). All inversions and direct modeling in this thesis were carried out using computational clusters from the Embrace program of INPE, Oregon State University, USA, and the Observatório Nacional (ON/MCTI), Rio de Janeiro, Brazil.

This section presents an overview of the procedure adopted to perform a 3-D inversion in ModEM. As an example, the process carried out to obtain a 3-D resistivity

model for the Parnaíba Basin region, north-northeast of Brazil, will be detailed. The MT and GDS transfer functions were provided by INPE's Geomagnetism group and are part of joint MT and GDS surveys carried out by INPE and ON/MCTI (RIGOTI et al., 1999; ARORA et al., 1999; SOLON et al., 2018; FONTES et al., 2022). In these surveys, the time series recorded in up to five electromagnetic channels were processed using a robust code (EGBERT, 1997) to estimate the complex MT tensor elements and the GDS responses at varying periods for each recording location. To ensure the plane wave hypothesis, only nighttime data from the GDS survey of the north-northeast region of Brazil were used in the derivation of the transfer functions to avoid possible effects generated by the diurnal currents of the equatorial electrojet. Note that the MT data were measured approximately 30 years after the GDS survey. Due to the continuous and slow westward drift in the main geomagnetic field at the Earth's surface, these MT data are not affected by the equatorial electrojet effects. As ambient electromagnetic noise levels during the surveys were generally low, reliable response function estimates were obtained for the entire period range used. Details about the data acquisition, its processing and the quality of the obtained transfer functions were discussed in these works cited above.

Before starting the inversion, some preliminary tests were done to decide the orientation for the grid coordinate system in which the Earth is discretized, the horizontal widths of the cells in the area of interest, the uniform half-space resistivity of the starting model, options for the error floors of impedance tensor and GDS components, selection of periods to be used for data fitting, and model covariance parameters (model smoothing) to obtain the best balance between roughness and smoothness of the inverted model.

After this evaluation, the grid coordinate system was taken as aligned with the geographic coordinates, with the x-direction of the model pointing to the north. The study area was limited between latitudes 10°N to 18°S and longitudes 60°W and 33°W, with the model center located at latitude 4.1°S and longitude 46.5°W. In this region, the Earth was discretized into a grid containing 122 cells in the x-direction, 102 cells in the y-direction, and 90 cells in the vertical direction. The internal part of the model comprised a mesh of $90 \times 70 \times 90$ cells, with edge lengths of 10 km in both horizontal directions. To constrain modeling artifacts at the edges of the model domain, this central part was filled on all four horizontal sides with 16 planes, where cell size increased laterally by a factor of 1.2. Cell sizes in the z-direction started from 20 m for the first cell at the surface and the thicknesses of subsequent layers successively increased by a factor of 1.1. This shallow starting

layer for the vertical mesh was chosen to allow the inversion to generate shallow structures to account for possible galvanic distortion effects.

A coarse 3-D bathymetry of the Atlantic Ocean was included as a priori information and a resistivity of 0.3 Ωm was assigned to seawater. This part of the model domain was kept fixed during the inversion procedure. In choosing the subset of data to be used in the inversion, a distribution of periods was sought that would improve the resolution of the deeper structure. Thus, the transfer functions were decimated into 12 target periods, evenly spaced on a logarithmic scale between 240 s and 10240 s.

A homogeneous 50 Ωm half-space was chosen as the prior and starting model (a value close to the average high frequency apparent resistivity in the Parnaíba basin), and all impedance tensor elements and GDS responses were used to improve the resolution of nearby structures (SIRIPUNVARAPORN et al., 2005b). Relative errors were kept as small as possible to ensure that variations in all MT and GDS data were reflected in the 3-D inversion process. Final error floors were assigned to 5% for off-diagonal impedance elements ($\boldsymbol{Z}_{xy}$ and $\boldsymbol{Z}_{yx}$), 10% for diagonal impedance elements ($\boldsymbol{Z}_{xx}$ and $\boldsymbol{Z}_{yy}$) and a constant value of 0.03 for GDS components. Measured data errors were used only when greater than these relative error limits. Finally, it was observed that the default value of 0.3 is the best choice for the model's covariance parameters in the three spatial directions. This gave us a rougher and not well resolved shallow structure, but a smoother and more reliable deep structure.

To obtain a preferred model, the inversion was run in two steps. First, the inversion was run using only the GDS transfer functions for the 29 available stations (including GDS data from the 7 MT stations) with the error floor and covariance values as indicated earlier, and the starting λ value set to 1000 to get a relatively smooth model. The inversion converged to a normalized rms misfit of 1.04 after 14 iterations in 5 days. The second step used this converged model as a prior model, but incorporated the impedance tensor elements from 7 broad-band MT stations located mainly on the east-central region of the Parnaíba Basin, together with the data from the 29 GDS stations. Error floor was 5% for the off-diagonal and 10% for the main diagonal impedance elements, covariance was 0.3, but the starting λ was set to 1 and GDS error floor was reduced to 0.02. The inversion started with an rms of 16.66 for the initial model and converged to a normalized rms misfit of 2.12 after 98 iterations in 11 days.

A detailed comparison between the measured and predicted MT and GDS transfer functions for the final inversion is shown in Figures 3.5-3.7. The discrete points

represent the experimental data, with the vertical bars indicating their standard deviation, and the solid lines are the corresponding results predicted by the inversion model. In general, there is a good fit between experimental and theoretical data for all components of the impedance tensor and magnetic transfer functions, indicating that the model is adequate to represent the measured transfer functions.

Figure 3.5 - Comparison of measured (discrete marks) with predicted MT responses (continuous solid lines) from the 3-D inversion model. Transfer functions for the real and imaginary $\boldsymbol{Z}_{xx}$ (blue), $\boldsymbol{Z}_{xy}$ (red), $\boldsymbol{Z}_{yx}$ (green) and $\boldsymbol{Z}_{yy}$ (magenta) components of the impedance tensor are shown for the 7 stations. Error bars are one standard deviation.

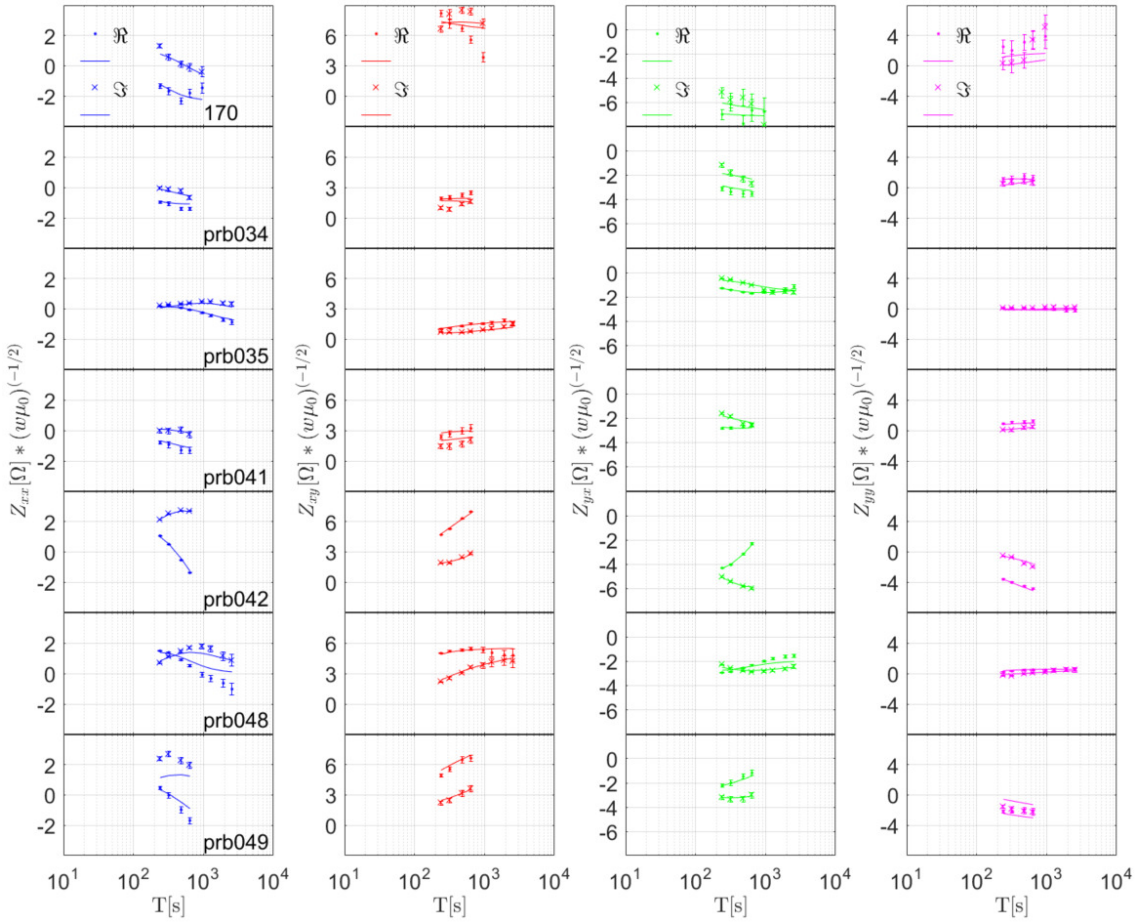

SOURCE: Author production.

Figure 3.6 - Comparison of measured (discrete marks) with predicted GDS responses (continuous solid lines) from the 3-D inversion model. Real (blue) and imaginary (red) components of the $\boldsymbol{T}_{zx}$ magnetic transfer function are shown for the 29 stations. Error bars are one standard deviation.

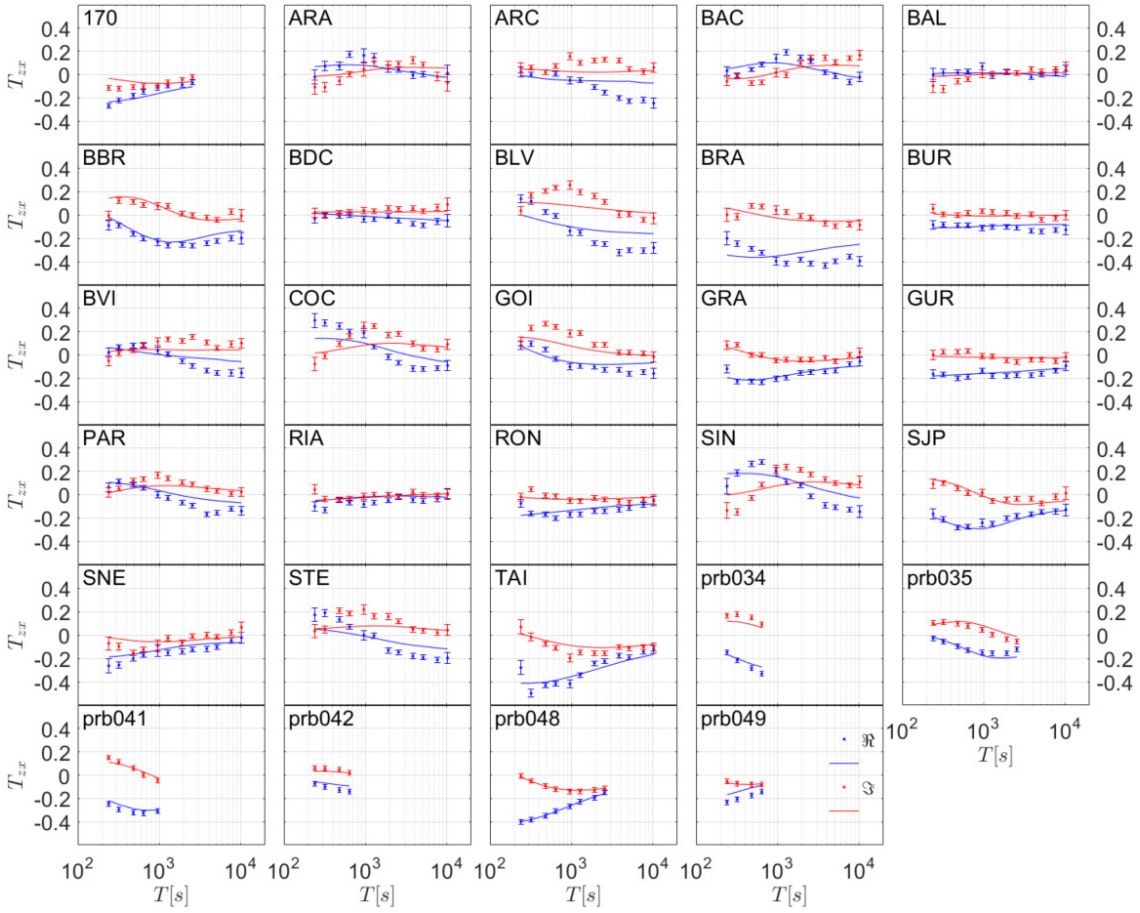

SOURCE: Author production.

Figure 3.7 - Comparison of measured (discrete marks) with predicted GDS responses (continuous solid lines) from the 3-D inversion model. Real (blue) and imaginary (red) components of the $\boldsymbol{T}_{zy}$ magnetic transfer function are shown for the 29 stations. Error bars are one standard deviation.

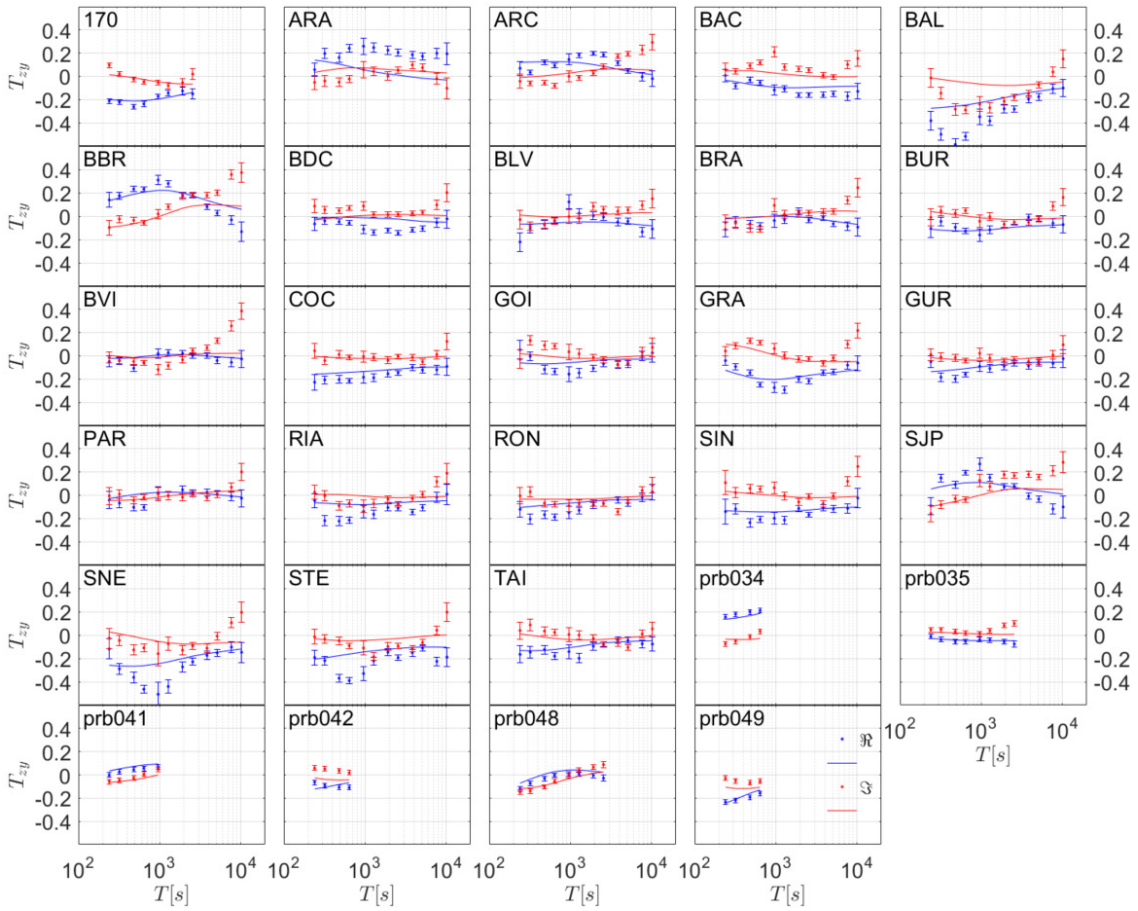

SOURCE: Author production.

When evaluating the reliability of a 3-D model, an important aspect is to assess how the misfits between measured and predicted data are distributed as a function of the measurement period and at each station. This is done in Figure 3.8, which shows the site-by-site distribution of *rms* misfits for all analyzed periods. In order to have a regional image, only the vertical magnetic transfer functions are presented. There are some high *rms* values randomly distributed, probably associated with noise, but mainly in the central part of the model there is a good fit to the data. A higher concentration of high *rms* misfits is observed in the stations of the extreme southeast of the study area, where some MT stations included in the inversion are

located.

Figure 3.8 - Site-to-site *rms* misfit distribution maps for different periods in the final 3-D inversion model. The rms (color coded) distribution is shown for GDS responses only.

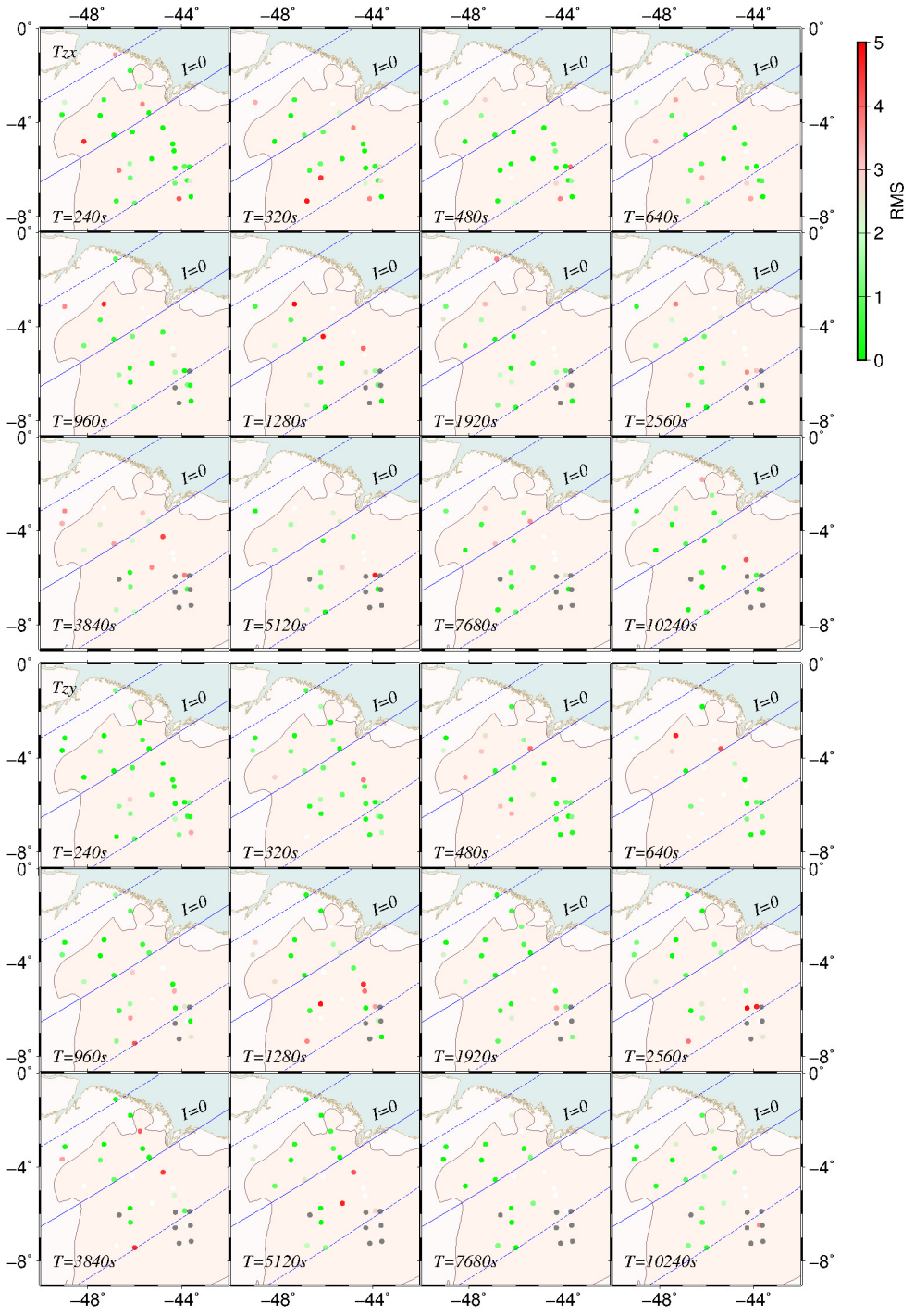

SOURCE: Author production.

The final 3-D inversion model is represented in Figure 3.9 by a horizontal slice at the crustal depth of 25.6 km. The regions of higher conductivity in this model section are represented by warm colors (red) and the regions of higher resistivity by cold colors (blue). Also shown is the horizontal grid by which the Earth's half-space was subdivided for 3-D inversion and projections of some main structural elements on the surface (continental margin and Parnaíba basin boundaries). A preliminary geophysical interpretation of the conductivity anomalies detected by the model will be discussed in Subsection 4.2.1.2 but they correlate with some structures previously identified by thin-sheet modeling of these GDS data (ARORA et al., 1999) and inversions along MT profiles across the basin (PADILHA et al., 2017; SOLON et al., 2018).

Figure 3.9 - A horizontal slice of the 3-D conductivity model from joint 3-D MT and GDS data at a depth of 25.6 km. Projections of the continental margin (black contour line), Parnaiba basin limits (white contour line) and position of MT (black dots) and GDS (white dots) sites on the surface are also shown. The conductivity color scale is logarithmic and covers the range 0.001-1 Sm^{-1}. The horizontal grid used for 3-D inversion is also shown (black straight lines).

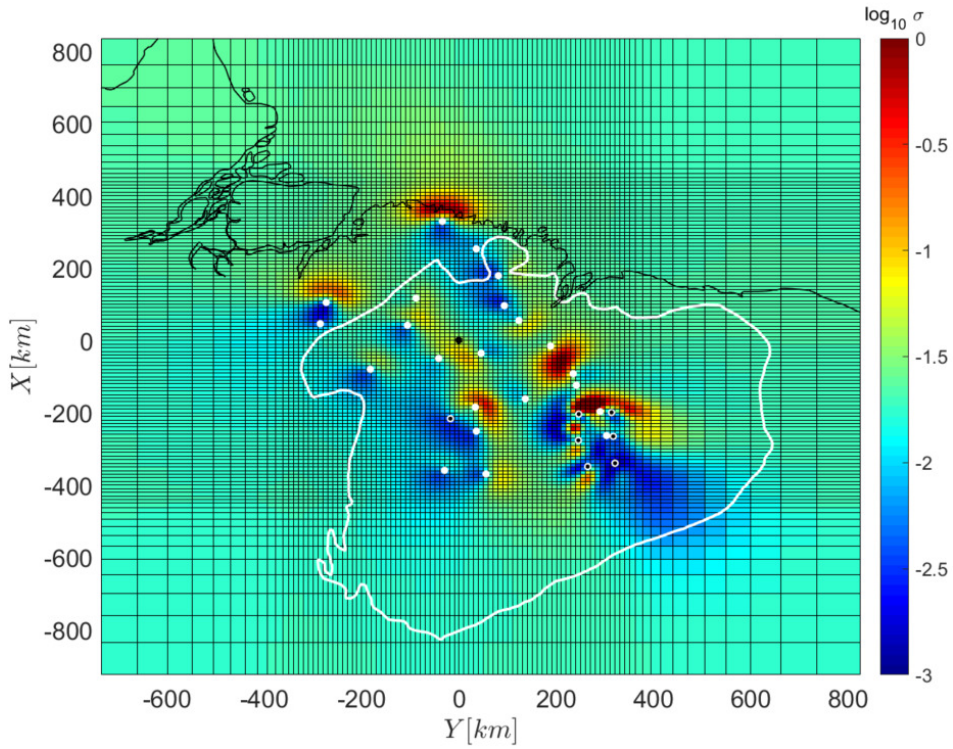

Using a tool developed by Kelbert et al. (2011).

SOURCE: Author production.

From this 3-D resistivity model, the impedance tensor elements can be derived anywhere in the model grid through forward calculation using the ModEM computational package. These impedances can be convolved with geomagnetic fields interpolated by the SECS technique during magnetic storms to allow obtaining the geoelectric field at any location in the study area.

3.3 Test of the algorithm developed to calculate the geoelectric field from the 3-D impedance tensor

MatLab computer codes were developed to estimate the geoelectric field from geomagnetic field variation data and 3-D impedance tensors. The procedure adopted is similar to that proposed by Kelbert et al. (2017), Love et al. (2018b), Lucas et al. (2018) and uses interpolation methods for the transfer functions ($\bar{\boldsymbol{Z}}$) and the Fourier transform of magnetic fields. The calculations are initially performed in the frequency domain, bounded by the Nyquist frequency ($1/2\triangle t$) related to the data acquisition rate.

Initially, the time series of the horizontal geomagnetic field ($\boldsymbol{B}_H(t)$) are transformed to the frequency domain ($\boldsymbol{B}_H(w)$) using the Fourier transform. In this step, time series with a duration of 1 to 3 days are normally considered, including the different phases of the magnetic storms. It should be noted that the MT information from the impedance vectors must be continuous in the frequency space to convolute with the Fourier transform result of the magnetic fields. Thus, it is necessary to interpolate the impedance tensor components (usually presented in discrete frequencies) to obtain a continuous spectrum of these transfer functions. It is considered the real and imaginary part of the full impedance tensor ($\boldsymbol{Z}_{xx}$, $\boldsymbol{Z}_{yx}$, $\boldsymbol{Z}_{xy}$ and $\boldsymbol{Z}_{yy}$). The chosen interpolation method is the cubic spline (AHLBERG et al., 1967), using polynomials of degree 3 between contiguous discrete points and ensuring that the first and second derivatives are continuous. In this way, the interpolation result does not show peaks or abrupt curvature changes at the points where the experimental data (MT transfer functions) are located.

Having the full impedance tensor ($\bar{\boldsymbol{Z}}_{\boldsymbol{ij}}$) and the geomagnetic field ($\boldsymbol{B}_H$) with the same frequencies, one can perform the basic tensor product of the MT method, defined by Equation 2.27. In this way, the geoelectric field in the frequency domain is determined. Then, the time series of the geoelectric field is obtained using the inverse Fourier transform.

The developed code was validated using geomagnetic variations and MT transfer

functions for the same region in Japan previously studied to validate the SECS algorithm (Subsection 3.1.2). The choice of this region was motivated by the availability of high-quality geoelectric data (available for over 70 years). Several observatories provide long-term series of geomagnetic field variations covering several storms, in addition to having long-period MT transfer functions (FUJII et al., 2015). This huge database has been widely used in the literature to test GIC modeling processes (KELBERT et al., 2017; LOVE et al., 2018b; LUCAS et al., 2018). The impedance tensor is available for a wide range of periods ($6.4 - 213,400$ s), equispaced on a logarithmic scale at 42 frequencies at the MMB observatory site (SCHULTZ et al., 2001-2011). Also, magnetic field records ($\boldsymbol{B}_x$, $\boldsymbol{B}_y$) acquired with a sampling frequency of 1 Hz were used. The procedure for obtaining geoelectric fields from this dataset was described above.

Figure 3.10 shows the geoelectric field estimates derived in this test using the magnetic disturbance records during the October 2003 severe magnetic storm "Halloween" ($Dst = -401$ nT). The electric field measured at the observatory are directly compared with the geoelectric field derived from our modeling. In terms of prediction efficiency, the test reached values of ≈ 0.89 and ≈ 0.83 for the components $\boldsymbol{E}_x$ and $\boldsymbol{E}_y$, respectively.

Figure 3.10 - Measured and estimated geoelectric fields at the MMB observatory during the Halloween geomagnetic storm. Top, comparison between electric fields estimated using developed computer code (red) and measured directly at the observatory (blue). Bottom, difference between estimated and measured electric fields.

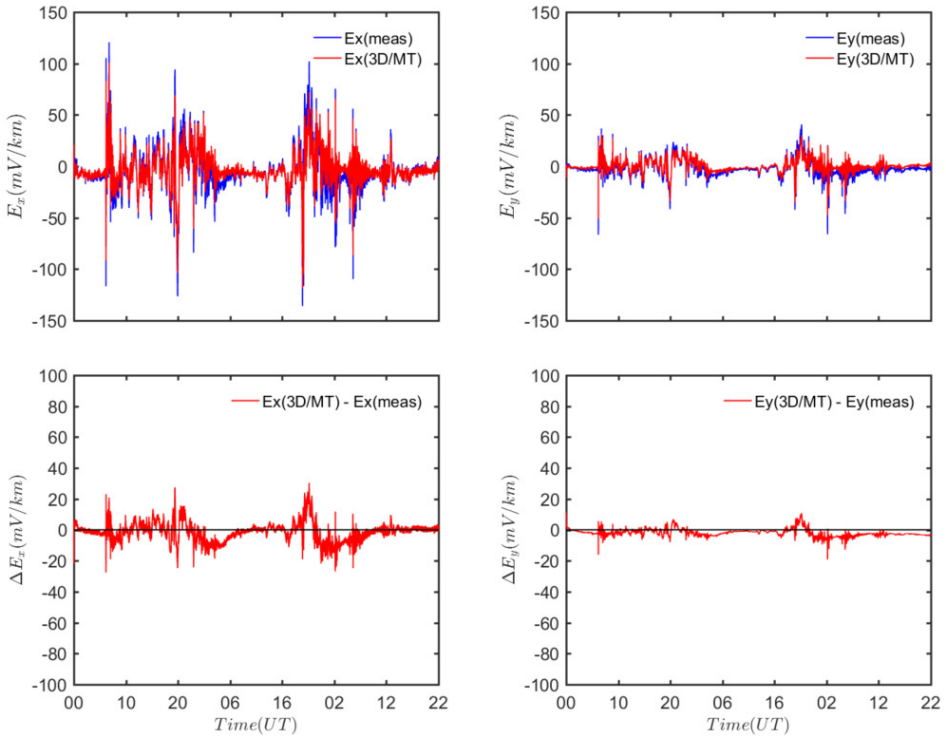

SOURCE: Author production.

For comparison, Kelbert et al. (2017) calculated the geoelectric fields that would have been obtained considering a 1-D model for the conductivity distribution under the MMB observatory. The results are displayed in Figure 3.11 and again compared with the measured data. The difference between the measured and calculated values is significant in this case, as the region where the observatory is located is strongly affected by a 3-D distribution of subsurface conductivity. This result justifies the choice of this thesis to adopt the full impedance tensor (3-D information) to represent the conductivity inside the Earth.

Figure 3.11 - Comparison between measured electric fields at the MMB observatory during the Halloween geomagnetic storm with estimated electric fields using a 1-D resistivity model (KELBERT et al., 2017). Top, measured (blue) and estimated (red) electric fields. Bottom, difference between estimated and measured electric fields.

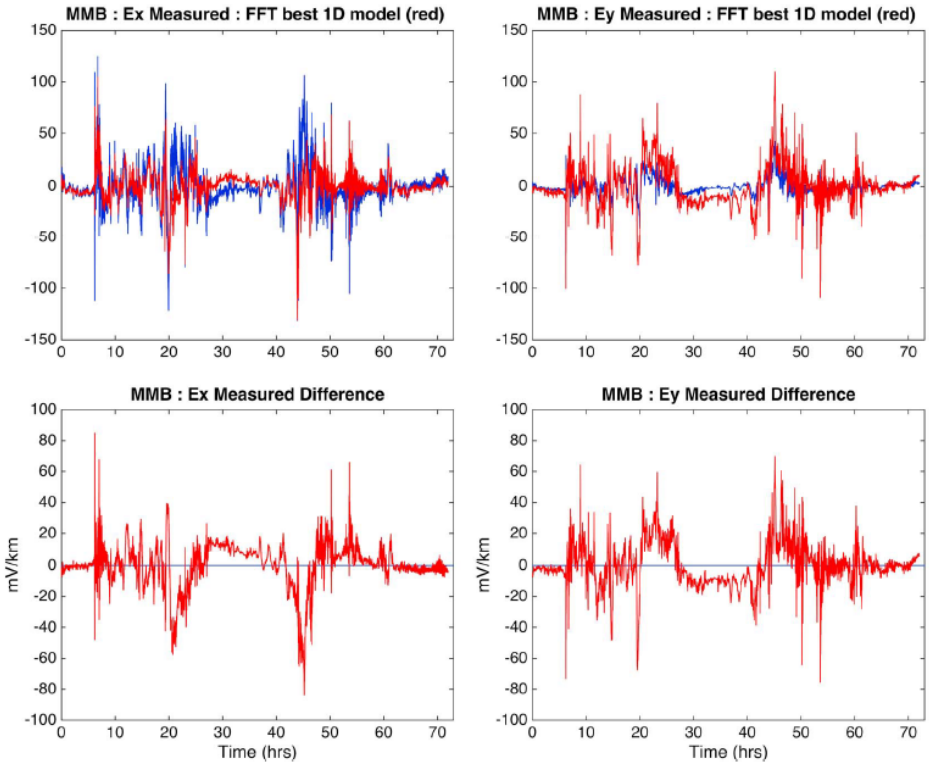

SOURCE: Kelbert et al. (2017).

The results of this validation test using the 3-D conductivity model are consistent with goodness of fit between measured and estimated geoelectric field at the MMB station for this same storm through computer codes produced by other authors (KELBERT et al., 2017; NAKAMURA et al., 2018). These authors reproduce the electric field measurements in MMB to within 15%, compatible with the result obtained here. Thus, the code developed to calculate the geoelectric field can be considered validated. Furthermore, depending on the characteristics of the local geology, the results show that the use of 3-D conductivity distributions instead of 1-D distributions for the modeling of GICs is highly recommended.

3.4 The Lehtinen & Pirjola (LP) method

Since the variation of the induced geoelectric field is rather slow, GICs can be approximated as quasi-direct currents (frequency ranges of decihertz or lower) superimposed on the 50/60 Hz power system currents. The induced geoelectric field can be represented by a voltage source between two substations (e.g., i and j) of a transmission line. This voltage can be calculated by integrating the vector electric field along the length between the substations and expressed as:

$$V_{ji} = \int_C \boldsymbol{E}\ d\boldsymbol{l} = \int_i^j \boldsymbol{E}\ d\boldsymbol{l} \tag{3.12}$$

where the line integral is along each finite segment of the path C between substations i and j, which takes into account the amplitude and direction of the electric field ($\boldsymbol{E}$), V_{ji} represents the voltage source between substations i and j, and dl represents the incremental length of the line.

Following Kirchhoff's laws, Lehtinen and Pirjola (1985) proposed an approach (LP method) to calculate earthing currents flowing in or out of the system at substation locations. In this case, the network is considered as a set of discrete grounded nodes, connected by the transmission line through a path $(i - j)$. Using this method, the GIC flowing through n earthed substations can be calculated as

$$I_n = (U + YZ_n)^{-1} J_n \tag{3.13}$$

where I_n is a $n \times 1$ vector of GICs flowing into the Earth, U is the $n \times n$ unit matrix, Y represents a $n \times n$ network admittance matrix that mainly depends on the resistance of the conductors, Z_n represents a $n \times n$ matrix containing earthing impedance, and J_n is a $n \times 1$ column vector with the induced nodal current sources. The elements of the nodal admittance matrix Y are defined by the resistance per unit length of the transmission lines (R_{ij}) interconnecting the substations, which are represented by

$$Y_{ij} = \frac{-1}{R_{ij}} \qquad i \neq j \qquad Y_{ij} = \sum_{\substack{k=1 \\ i \neq k}}^{n} \frac{1}{R_{ij}} \qquad i = j \tag{3.14}$$

Also, based on the calculated voltage using Equation 3.12, the elements of the column

matrix J_n can be obtained through

$$J_{ni} = \sum_{j \neq i} \frac{V_{ji}}{R_{ji}} \tag{3.15}$$

A computer code was written to calculate GICs at each node (substation) of a transmission line using the matrices of Equation 3.13. It was previously validated by comparing estimated amplitudes with direct measurements at a substation during a magnetic storm that occurred on October 8, 2013 (ESPINOSA et al., 2019).

4 MODELING GEOMAGNETICALLY INDUCED CURRENTS - CASE STUDIES IN BRAZIL

This chapter addresses two case studies of modeling GICs in simplified power networks operating at 525 kV in Brazilian territory [1]. In the southern region, measurements with high cadence (1 s) of three magnetometers from the EMBRACE program are used to interpolate geomagnetic variations by the SECS method. In the north-northeast region, geomagnetic variations observed during an old GDS campaign through magnetometers installed around the *dip equator* with a resolution of 1 min are used. In both cases, 3-D models were derived to represent the underground electrical conductivity structure and the modeling process to estimate GICs during magnetic storms was carried out by applying the previously described methodology.

4.1 GIC estimation in a power network of southern Brazil

This section reviews the paper *"Estimation of geomagnetically induced currents in the electrical grid of southern Brazil using a 3-D terrestrial resistivity model"* by Espinosa et al. (2022) currently submitted for publication. It presents the first GIC study in a South American power grid using 3-D subsurface resistivity structure and high-cadence geomagnetic variations to derive geoelectric fields during geomagnetic storms.

For this study, geomagnetic data with resolution of 1 s provided by the EMBRACE magnetometer network (DENARDINI et al., 2018) were interpolated in southern Brazil during two geomagnetic storms using SECS. 3-D impedance tensor elements were obtained from forward calculation using an Earth resistivity model for the study region. Following the procedure described earlier in this thesis, the surface geoelectric fields were derived using the interpolated geomagnetic data and the 3-D MT impedances, following the plane-wave assumption (Equation 2.27). Finally, using the LP approach, these local geoelectric fields and a simplified model of the 525 kV transmission network in southern Brazil were combined to estimate GICs at each substation (node) of the network. This modeling sought to locate weak spots in the considered grid, which would be more susceptible to the risk derived from induced currents. Another objective is to implement an operational methodology for the EMBRACE program to assess potential GIC hazards in the Brazilian power transmission system.

[1] This section is an adapted version of Espinosa et al. (2022).

4.1.1 Data sources

The information available for southern Brazil and necessary to simulate GIC magnitudes during the two selected geomagnetic storms is described in this section. Details are presented on the local geology, Earth's resistivity structure, magnetic field observations and a representation of the high voltage transmission system, considering its topology, network resistance and location of the substation grounding points.

4.1.1.1 Geological background and available geoelectrical information

The South American platform is characterized by a central core formed by several Archean to Mesoproterozoic cratonic nuclei from earlier supercontinents welded together during the Neoproterozoic Brasiliano/Pan African Orogeny in the final assembly of West Gondwana (ALMEIDA et al., 2000). Intracratonic basins cover an extensive segment of this Precambrian framework. The study area in south-central Brazil (Figure 4.1a) is marked by the presence of the Paraná basin, a large intracratonic feature deposited from Late Ordovician to Late Cretaceous in response to a geological stabilization after the Brasiliano Orogeny.

The basin consists of a thick and vast sedimentary-magmatic sequence covering about $1,700,000$ km^2, mainly in southern Brazil and Uruguay, Paraguay, and Argentina. The stratigraphic succession in the study area outlines successive episodes of subsidence and uplift, with a thickness of up to 7000 m in the central depocenter (ZALÁN et al., 1990). Just before the breakup of the supercontinent Pangaea in the Early Cretaceous, one of the most voluminous volcanic events in the Earth's history covered the basin with basaltic lava flows, while many dykes and sills also intruded the sedimentary sequence (MELFI et al., 1988). After basaltic volcanism, the northern part of the basin subsided and a thin layer of continental sediments was deposited in the Late Cretaceous, ending the depositional history of the basin. Below the basin, the basement structure remains uncertain with different proposed lithospheric models, such as a single cratonic block underneath the axial region of the basin surrounded by mobile belts of the Brasiliano age (MANTOVANI et al., 2005) or a collage of fragmented blocks separated by interposed suture zones (MILANI; RAMOS, 1998).

The 3-D deep electrical resistivity structure of this region was previously investigated using 63 regional-scale GDS data with an average site interval of $\sim$ 100 km (see GDS station distribution in Figure 4.1a), but constrained by different MT datasets (PADILHA et al., 2015; MAURYA et al., 2018). These MT data were mainly from broad-

band soundings positioned along profiles in the central part of the basin. These two studies generically modeled the same resistivity distribution at medium-to-lower crustal and upper mantle depths, which are represented in Figure 4.1b through a horizontal resistivity map at a lower crustal depth (33 km) of the model by Padilha et al. (2015). It shows that the crust below the basin consists of several quasi-linear highly conducting channels of limited lateral extent.

Figure 4.1 - Regional geology and 3-D resistivity models for the study area. (a) Generalized geological map of southern Brazil, with emphasis on the Brazilian part of the Paraná basin (modified from Bizzi et al. (2001)). Locations of GDS, long-period MT, and EMBRACE magnetic stations are shown. Geological periods of outcrops are: CZ = Cenozoic; K = Cretaceous sediments; SG = Early Cretaceous basalts; TC = Triassic to Cambrian sediments; PZ = Proterozoic; and AR = Archean. The inset shows the study area with the full areal extent of the Paraná Basin (PB) and contiguous Chaco-Paraná basin (CP) in northeastern Argentina. (b) A horizontal section at a depth of 33 km from the 3-D resistivity model of Padilha et al. (2015), derived from GDS data alone. The position of the GDS sites (dots) and Paraná Basin boundaries (white dashed lines) is shown. (c) Same as (b) from the 3-D resistivity model derived for this thesis using joint GDS (dots) and long-period MT (triangles) data.

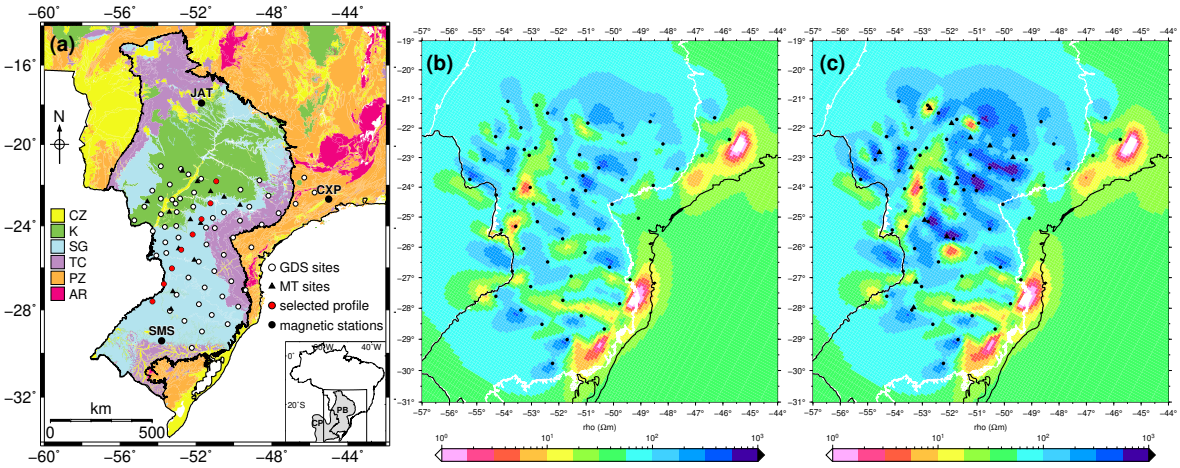

SOURCE: Author production.

A new 3-D resistivity model was derived for this thesis incorporating 13 new long-period MT stations distributed over different regions of the Paraná basin to the GDS array data. The procedure was generically the same described in Section 3.2. The

parallel 3-D inversion code ModEM3DMT was used for data inversion that included all four components of the impedance tensor of the MT sites (periods from 300 to $10,000$ s and error floors of 5% for the off-diagonal and 10% for the on-diagonal impedance elements) and vertical magnetic responses of GDS and MT sites (periods from 300 to $3,000$ s and a constant error floor of 0.02). The model grid was the same as that of Padilha et al. (2015), with a covariance value of 0.3 applied once in all directions and the Atlantic Ocean (0.3 Ωm seawater resistivity) included as *a priori* and fixed structure.

The previous model of Padilha et al. (2015) was used as the starting model and after 77 iterations in 9 days the inversion converged to a normalized *rms* of 2.8. The final 3-D inversion model is represented in Figure 4.1c by a horizontal slice at a depth of 33 km. The same elongated major conductivity anomalies are observed when comparing the previous (Figure 4.1b) and current (Figure 4.1c) 3-D resistivity models. However, the new model features a more resistive crustal core, especially in the northern portion of the basin where most long-period MT soundings are concentrated. This new 3-D model will be used to obtain the full impedance tensor and geoelectric field amplitudes across the study area during the selected geomagnetic storms.

4.1.1.2 Geomagnetic field variations

Two intense geomagnetic storms that occurred in the decreasing phase of sunspot cycle 24, on 21-23 June 2015 (minimum Dst of -204 nT) and 19-21 December 2015 (minimum Dst of -175 nT), were chosen for GIC modeling. Of the 16 magnetic stations currently operated in the EMBRACE array, 3 were selected based on data availability for the two events and geographic distribution in the study region (see Figure 4.1a). Details about the stations are presented in Table 4.1, where geomagnetic information was obtained using IGRF-13 coefficients (ALKEN et al., 2021).

Table 4.1 - Geographic and geomagnetic coordinates and total geomagnetic field strength at the selected EMBRACE stations for 2015.

	Geographic		Geomagnetic			
Code	Lat.	Lon.	Lat.	Lon.	Total field (nT)	Inclination(°)
CXP	22.70 S	45.01 W	19.49 S	22.41 E	23,085	-37.56
JAT	17.93 S	51.72 W	12.61 S	17.77 E	23,024	-25.37
SMS	29.44 S	53.82 W	21.62 S	13.50 E	22,477	-37.18

SOURCE: Author production.

EMBRACE magnetometers produce digital samples at a rate of one sample per second, which are averaged to 1 min resolution for data distribution (DENARDINI et al., 2018). Specifically for this study, the 1 s time resolution raw measurements were accessed and the first derivatives of the horizontal ($\boldsymbol{H}$) and declination (D) magnetic vector components were used to identify local spikes and other artificial disturbances. The $\boldsymbol{H}$ and D geomagnetic time series were converted into northward (B_x) and eastward (B_y) data, using $B_x = HcosD$ and $B_y = HsinD$. Following, a low-pass filter with a cutoff frequency of 100 mHz (equivalent period of 10 s) was chosen to remove high-frequency components in the raw magnetic data (B_x, B_y). This is in line with previous studies arguing that the geomagnetic field variations that generate the greatest risk for high voltage power grid transformers occur in periods of about 10 to 1000 s (BEDROSIAN; LOVE, 2015; CUTTLER et al., 2018).

The magnetic signature of the two geomagnetic storms is shown in Figure 4.2, which plots the northward (ΔB_x) and eastward (ΔB_y) components of the horizontal magnetic field at the three EMBRACE stations. As a typical result for low geomagnetic latitudes, the magnetic field variation of the northern component is much greater than that of the eastern component. Furthermore, the recorded geomagnetic variations are very similar in the 3 stations, despite the large separation between them (maximum distance of 1300 km between JAT and SMS) and possible effects that could be attributed to the South Atlantic Magnetic Anomaly (SAMA). This region of global minimum geomagnetic field strength leads to enhanced precipitation of energetic particles in the local ionosphere and increased amplitudes in horizontal magnetic components have been reported in the center of the anomaly during magnetic storms (TRIVEDI et al., 2005). However, the similarity between the ground geomagnetic variations shown in Figure 4.2 does not indicate that SAMA ionospheric effects contributed significantly during the two analyzed storms.

Figure 4.2 - Low-pass filtered geomagnetic field time series for northward (ΔB_x) and eastward (ΔB_y) components at the three EMBRACE stations during the geomagnetic storms of June (left panels; from 12 UT on 21 June to 18 UT on 24 June 2015) and December (right panels; from 08 UT on 19 December to 20 UT on 21 December 2015).

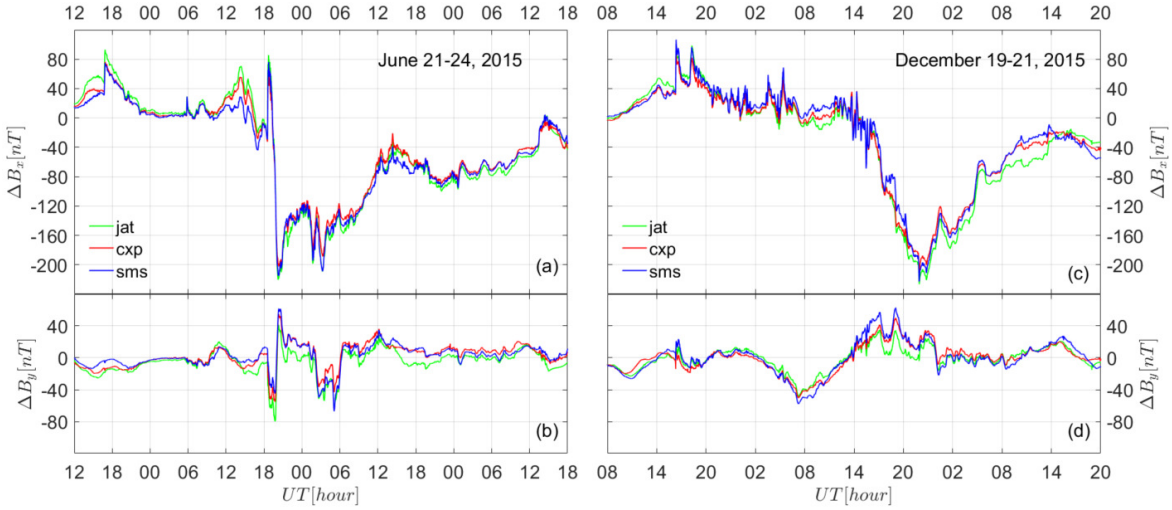

SOURCE: Author production.

However, GICs are commonly associated with rapid temporal variations of the geomagnetic field during magnetic storms and therefore more directly related to high frequency signals. Figure 4.3 compares the Fourier spectral power of the time derivative of the geomagnetic field during the two magnetic storms at the three EMBRACE stations shown in Table 4.1. Each panel presents a snapshot of the dB/dt spectrogram around (120 s) selected time instants. The distribution of signal energy across frequencies was obtained through the Parseval relation (SMITH, 2013). Panels in the horizontal direction correspond to instants in the time derivative of the geomagnetic field (6 snapshots in each storm) that correspond to some selected peaks during the storms to be listed in Table 4.2. As much of the geomagnetic field variation that drives GICs is at the higher end of the spectrum, in this case from 10 s to 100 s, it is critical to determine whether the spectra of these time series exhibit the same behavior visually observed in Figure 4.2. The results in Figure 4.3 do not show substantial changes in signal power throughout the entire frequency range when comparing the same time instant in the three magnetic stations. As a consequence, geomagnetic field disturbances at the three widely separated sites in Figure 4.2 have similar mag-

nitudes and power spectra, indicative of the homogeneity of the magnetic signal in our study region during the two magnetic storms.

Figure 4.3 - Comparison of instantaneous dB/dt power spectra at the three geomagnetic stations during selected peaks of the two magnetic storms. Panels in the top three rows correspond to the June storm spectrograms with the day and time of each snapshot identified in the top two rows, respectively. Panels on the bottom three rows correspond to the December storm spectrograms with the day and time of each snapshot labeled analogously to the June storm.

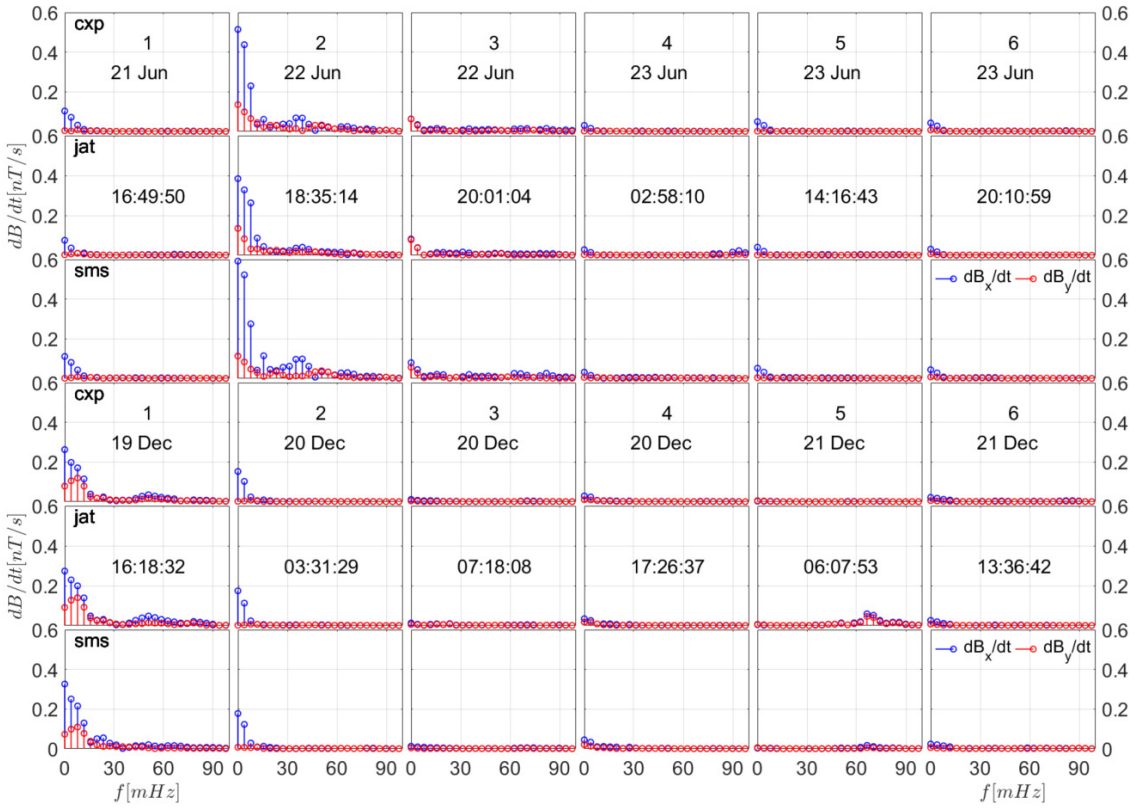

SOURCE: Author production.

4.1.1.3 High-voltage power transmission lines of south-southeast Brazil

South-southeast Brazil is the most populous and industrialized region in the country, thus presenting the largest number of high voltage networks and power plants. The high-voltage network in this region consists of transmission lines with a voltage level of up to 765 kV. A simplified representation of the grid is shown in Figure 4.4, where

network branches with different operating voltages are presented with colored lines (red = 765 kV, blue = 525 kV and green = 440 kV). Lower voltage elements of the power network (mainly 345 kV and 230 kV) are not included in the figure, which also shows the layout of the Bolivia-Brazil gas pipeline (Gasbol).

Figure 4.4 - Map with straight-line approximations of the three main high-voltage transmission lines in south-southeast Brazil and the path of the Gasbol pipeline. The region covering the Paraná basin in Brazil is shown in pink.

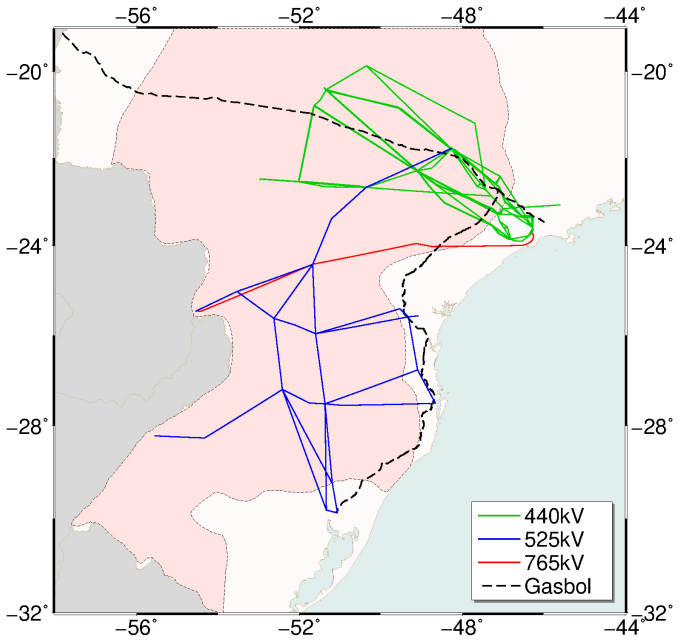

SOURCE: Author production.

For the GIC simulation, only the 525 kV network was considered as it is located within the region where the 3-D resistivity model is available and the geomagnetic interpolations are more reliable. Low-voltage networks were ignored in these calculations as more intense GICs are expected in the high voltage branch due to longer line sections and lower line resistances (ZHENG et al., 2014). However, several studies have shown that neglecting the low voltage portion of a network can lead to overestimated GICs (TORTA et al., 2014; BLAKE et al., 2018), particularly in substations with direct connections to the lower voltage elements. Our modeling is justified because we are at this stage mainly looking for the nodes most susceptible to large

increases in GIC for installing monitoring equipment, rather than trying to make an accurate GIC magnitude prediction. The simplified network 525 kV is composed of 31 transmission lines and 23 substations, each one corresponding to a ground node represented by a single conductor. This means that a three-phase power transmission line is connected to a transformer with a neutral point on ground, with the total resistance given by the sum of the transformer resistance and the earthing resistance.

4.1.2 Estimates of geoelectric fields during the 2015 geomagnetic storms

Together with the 3-D resistivity model for the region encompassing the Paraná basin in southern Brazil, the geomagnetic field variations recorded by EMBRACE magnetometers can be used to estimate geoelectric fields during the 2015 storms. The procedure involves interpolation of the magnetic field in the region of interest using SECS and its convolution with the impedances derived through forward calculation of the resistivity model.

4.1.2.1 Interpolating the geomagnetic field variations

The SECS interpolation method has shown good results at high latitudes (PULKKINEN et al., 2003; VANHAMÄKI; AMM, 2011; WEYGAND et al., 2011; RIGLER et al., 2019), where near-vertical FAC flowing radially along the geomagnetic field and connecting ionospheric currents to the magnetosphere is a reasonable approximation. At lower latitudes, where magnetic field lines are tilted, this approximation is more problematic and the use of this technique for magnetic field interpolation purposes during disturbed periods has been questioned (MCLAY; BEGGAN, 2010; TORTA et al., 2017). However, other studies have shown very reasonable interpolation results in low latitude regions of South Africa (BERNHARDI et al., 2008), Uruguay (CARABALLO et al., 2013) and Brazil (DIOGO, 2018). In particular, this last study was carried out in the central region of Brazil, adjacent to the area where GICs are being here estimated. Diogo (2018) showed that a large density of poles and an extrapolation of the SECS equivalent current system to an area much larger than the region covered by the data must be used to avoid the occurrence of artifacts and improve the interpolation accuracy.

In line with this approach, Figure 4.5a displays the area of analysis over which the elementary ionospheric current poles were placed to interpolate geomagnetic fields in southern Brazil. The altitude of the ionospheric equivalent current sheet was 100 km and the distances of the poles in the grid (marked as brown dots) were 0.4° and

0.6° in the longitudinal and latitudinal directions, respectively. Elementary current intensities during magnetic storms were determined to provide minimal error match with EMBRACE magnetometer records. The magnetic field was then interpolated on the Earth's surface to the locations of the 63 GDS stations shown in Figure 4.1a.

An essential role in the different stages of GIC studies is played by validation tests that aim to verify the capacity, precision and limitations of the modeling. Due to our limited dataset and lack of GIC measurements in substations, we opted for a qualitative evaluation, verifying the physical reasonableness of the magnetic field inputs and outputs and observing the robustness of the modeling in not generating interpolation artifacts in the calculated geomagnetic field. From the results shown in Figure 4.2, no significant variations in the interpolated fields between nearby sites are expected. Furthermore, due to its greater sensitivity to spikes and because it is commonly used as an indicator of the level of geomagnetically induced electric field at the Earth's surface (VILJANEN et al., 2001), the time derivative of the magnetic field (dB/dt) was chosen to compare observation and model data.

Figure 4.5 - SECS interpolation of geomagnetic field variations. (a) Equivalent ionospheric current grid (brown dots) to estimate the elementary current amplitudes. Red closed triangles indicate where the SECS amplitudes are calculated on the surface, with the inset showing the GDS site names and the chosen profile. (b) dB_x/dt observed at geomagnetic stations (*jat*-green, *cxp*-red, and *sms*-blue) and interpolated at the selected profile sites from 12 UT on 21 June to 20 UT on 23 June 2015. (c) Same as (b) for dB_y/dt.

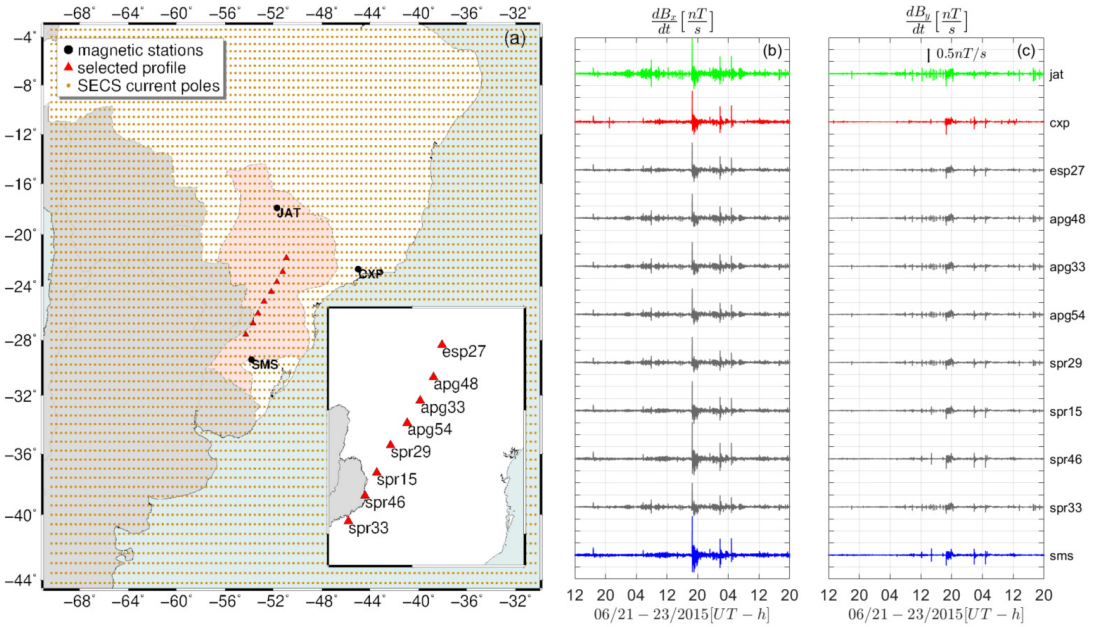

SOURCE: Author production.

Figure 4.5 exemplifies our validation of the interpolated dB/dt fields by showing a comparison of these fields predicted by the SECS model with the available observations. The NE-SW profile highlighted in the central part of the Paraná basin (Figure 4.5a) was selected for comparison and will also be used in the next sections when discussing the calculated geoelectric field. The dB/dt values during the June storm are shown in Figure 4.5b-c, as measured at the 3 EMBRACE stations and derived by SECS at the selected profile sites. A threshold of 23% of the maximum singular value was used to obtain the most reliable interpolation over the June storm. The results are in accordance with the assumptions previously established to consider adequate the interpolation of the magnetic field by SECS. There are no anomalous spikes in the interpolated fields and the dB/dt varies smoothly between the interpolated sites and the measured stations. In fact, the interpolation results

across the profile resemble a latitudinal weighted average of observed data. It can be then assumed that SECS model geomagnetic field variations change smoothly depending on latitude during the studied magnetic storms in this low-latitude region.

4.1.2.2 Synthetic test of geoelectric field calculation

To calculate the geoelectric fields, 345, 535 points of the interpolated magnetic field time series were computed at each GDS survey site for the June storm (from 00 : 00 : 13 UT on June 21 to 23 : 59 : 07 UT on June 24, 2015) and 338, 400 points for the December storm (from 23:59:44 UT on December 18 to 21:59:43 UT on December 22, 2015) with a sampling interval of 1 s. A Hann window function was applied to the time series to minimize spectral leakage in the FFT calculation. The 1-D magnetic field spectra were calculated for the components B_x and B_y in the bandwidth $0.1 - 0.0001$ Hz (periods of $10 - 10,000$ s) at each site.

Due to the limited period range of the MT and GDS data used to obtain the 3-D resistivity model, only periods above 300 s (frequencies below 0.0033 Hz) were considered for calculating the geoelectric field. The MT transfer functions (tensor impedances) of the 3-D resistivity model were derived at each GDS site over the same interval of $0.0001 - 0.0033$ Hz, with 10 estimates per frequency decade equally spaced in a logarithmic scale, through forward calculation using the ModEM software package. In order to have the same frequency spectra in the magnetic field and in the MT model response, the real and imaginary parts of all impedance tensor components were interpolated to have a continuous spectrum of the transfer functions. The geoelectric field spectra were then computed by convolving the MT tensors with the magnetic fields as in Equation 2.27. The geoelectric field time series were finally derived by inverse FFT and removing the window effect.

To validate the developed computer code and perform a simple examination of the effects of Earth's resistivity structure, synthetic geoelectric fields that would be induced by a geographically uniform reference geomagnetic signal were calculated. A peak recorded at 5:48 UT on June 22 storm in component B_x was chosen and its spectrum is defined here as $B_0(\omega)$. Three hypothetical scenarios were considered, with the magnetic field polarized in the directions south ($-B_x(\omega) = B_0(\omega)$, $B_y(\omega) = 0$), west ($B_x(\omega) = 0$, $-B_y(\omega) = B_0(\omega)$) and southwest ($-B_x(\omega) = -B_y(\omega) = \sqrt{2}B_0(\omega)$).

Figure 4.6 shows maps during the chosen time instant with the spatial change in magnitude and direction of the derived 2-D vector geoelectric field compared to mag-

netic variations ΔB and time derivative dB/dt for the three different polarizations of the magnetic field. A rough orthogonality between the magnetic and electrical vectors can be seen for the different polarizations. However, there are few sites showing a typical 1-D resistivity structure with the geoelectric field vectors really orthogonal to the direction of the polarized geomagnetic field and have almost the same magnitude, regardless of the direction of the inducing geomagnetic vector. In most cases, geoelectric vectors have different magnitudes from one site to another and are oriented at acute and obtuse angles in relation to the inducing geomagnetic vector. These site-to-site differences are due to local differences in the impedance tensor, related to the Earth's 3-D resistivity structure

Figure 4.6 - Snapshots of the modeled geoelectric field (red arrows) for three different magnetic field polarizations compared to magnetic variation B (blue arrows) and time derivative dB/dt (green arrows). (a) Magnetic field polarized in the NS direction; (b) magnetic field polarized in the EW direction, with reference arrows corresponding to 90 nT for B, 0.1 nT/s for dB/dt and 30 mV/km for E; and (c) magnetic field polarized in the SW direction.

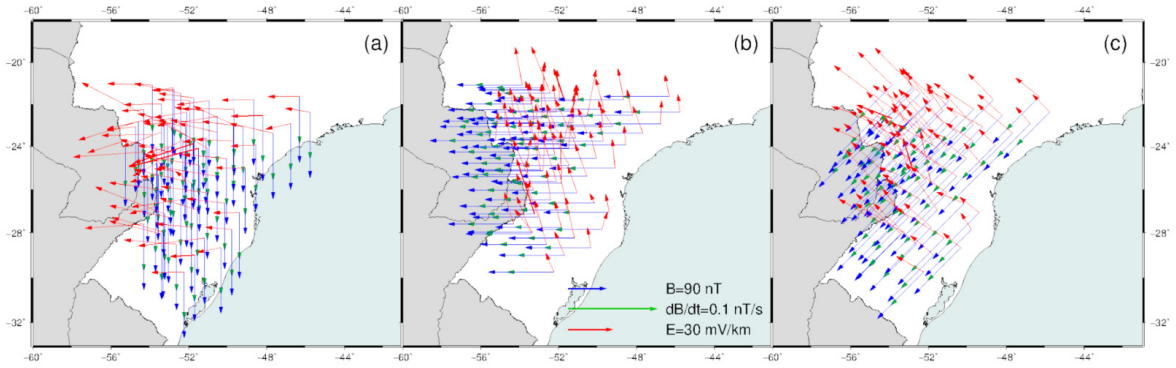

SOURCE: Author production.

The more significant changes in vector direction and the largest amplitudes of synthetic geoelectric fields are observed in the central and northeastern portions of the Paraná basin, where the 3-D model shows high resistivities. On the other hand, the entire eastern part of the GDS array shows low amplitudes of the geoelectric field regardless of the polarization of the magnetic field. This is an unpredicted result as it would be expected that for some polarizations the coast effect would

predominate in this region. This effect is related to a concentration of induced currents in the ocean where the conductivity is much higher than that of surrounding coastal rocks. In a 2-D context, the geoelectric field would be amplified or damped depending on whether the inducing geomagnetic field is parallel (H-polarization or TM-mode) or normal (E-polarization or TE-mode) to the coastline, respectively. The magnetic field polarized in the north-south (Figure 4.6a) and south-west (Figure 4.6c) directions correspond to the TM-mode in relation to different regions of the coast and should lead to an amplification of the synthetic geoelectric vectors at sites approaching the coast. Unobservance of these amplification effects in the south-southeast region of Brazil is interpreted as due to the presence of high conductivity anomalies bordering the entire coastline (see Figure 4.1b-c). Also, due to the shallow waters in this part of the South Atlantic Ocean (seafloor bathymetry less than 200 m up to 200 km from the coast), coast effects are relatively weak and do not extend over great distances onshore.

4.1.2.3 Geoelectric time series during the 2015 geomagnetic storms

The same procedure of the synthetic test was used to derive the geoelectric fields from the interpolated geomagnetic variations during the two magnetic storms. Figure 4.7 presents the geoelectric field time series estimated in the north-south (E_x) and east-west (E_y) directions during the June storm at the 8 chosen sites of Figure 4.5a. Stronger geomagnetic variations are usually observed in the S-N direction (B_x), close to the Earth's magnetic meridian, and cause the geoelectric field to have a much larger magnitude in the E-W direction (E_y) than in the S-N direction (E_x). Also, considering the same polarization for the magnetic field, the greatest magnitudes of the geoelectric field are observed in more resistive regions. This can be seen, for example, when comparing the magnitude of the geoelectric field E_y modeled for station *apg*33 with its neighboring stations *apg*48 and *apg*54. The peak magnitudes of the E_y field for these three sites observed around 20:01 UT on June 22 was -46.7 mV/km (*apg*48), -142.2 mV/km (*apg*48) and -61.0 mV/km (*apg*54).

Figure 4.7 - Geoelectric field E_x (red) and E_y (blue) time series for the storm of 21-24 June 2015 for each of the GDS locations of Figure 4.5, derived using the 3-D modeled impedance tensors from resistivity model in Figure 4.1c and filtered geomagnetic variations of Figure 4.2a-b.

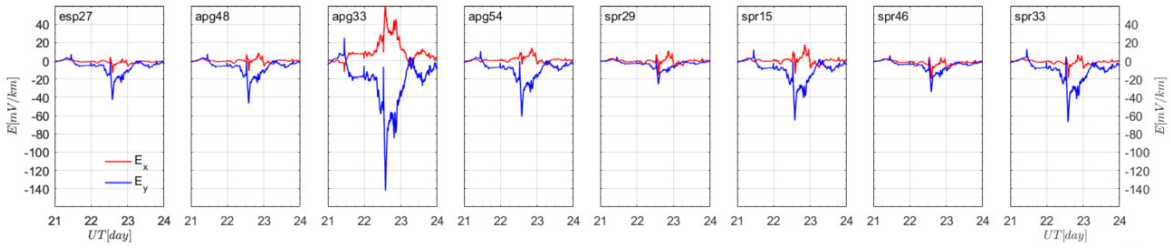

SOURCE: Author production.

Geomagnetic storms are transient phenomena that cause high rates of change in horizontal geomagnetic components observed on the Earth's surface. These stormy disturbances often vary over a wide range of frequencies and as a consequence give rise to geoelectric fields with very different spectral content. Geoelectric fields with different frequencies of oscillation can also affect technological systems on the surface differently. Thus, an important aspect in GIC studies is to correlate the main peaks of geoelectric field variation with the characteristics of the rate of change of the magnetic field.

A comparison of the estimated geoelectric field time series during the two storms at *apg*33 with the time derivative of the magnetic field (dB/dt) and its Fourier spectral power at selected instants is shown in Figure 4.8. In the upper and intermediate panels are identified instants in the geoelectric field time series and in the magnetic field time derivatives (6 vertical dashed lines in each storm) that correspond to some chosen peaks in the geoelectric field. These time instants are presented in Table 4.2 and include the storm sudden commencement (*ssc*), another CME impact and the maximum geoelectric field of the June storm (snapshots 1, 2 and 3, respectively) and the *ssc* of the December storm (snapshot 1). At the bottom of Figure 4.8 are snapshots of dB/dt spectrograms around (120 s) each of the time instants. Parseval's relation (SMITH, 2013) was used to indicate how the signal energy is distributed over frequencies.

Figure 4.8 - Comparison of calculated geoelectric field, dB/dt and instantaneous dB/dt power spectra at site *apg*33. The upper graphs show estimated geoelectric field time series (E_x and E_y) during the two magnetic storms. Intermediate graphs show the corresponding dB_x/dt and dB_y/dt during that time period. At the bottom are snapshots of dB_x/dt and dB_y/dt power spectra at the time instants identified by vertical dashed lines in the graphs above.

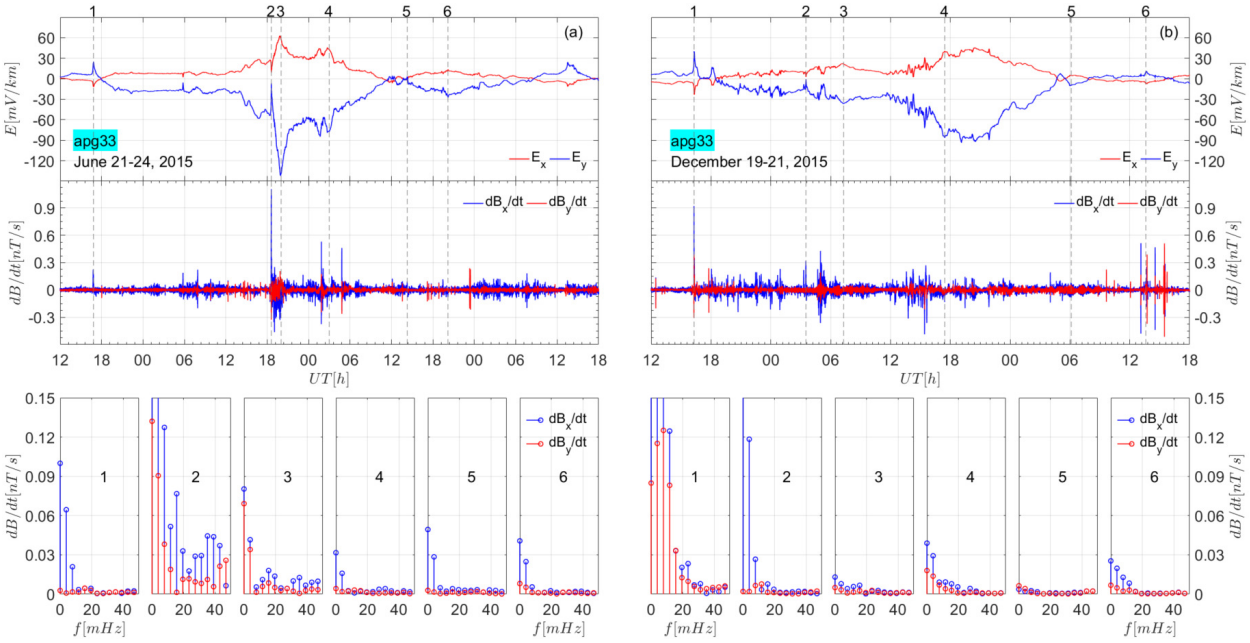

SOURCE: Author production.

Table 4.2 - Time instants of the selected snapshots presented in Figure 4.8.

June 2015			**December 2015**		
Snapshot	**Date**	**Time (UT)**	**Snapshot**	**Date**	**Time (UT)**
1	21 Jun	16:49:50	1	19 Dec	16:18:32
2	22 Jun	18:35:14	2	20 Dec	03:31:29
3	22 Jun	20:01:04	3	20 Dec	07:18:08
4	23 Jun	02:58:10	4	20 Dec	17:26:37
5	23 Jun	14:16:43	5	21 Dec	06:07:53
6	23 Jun	20:10:59	6	21 Dec	13:36:42

SOURCE: Author production.

Contrary to what would be expected during magnetic storms for the spectral power to be distributed in different directions and over a wide range of frequencies, the spectral content of all selected peaks shows a significant predominance of dB_x/dt amplitudes and of low-frequency components (generally less than 10 mHz). The only exception is the peak amplitude dB_x/dt in the June storm, identified as snapshot 2 in that storm. It presents the highest spectral power at low frequencies but also has important high-frequency spectral components. For the December storm, the highest dB/dt and spectral power are observed at peak 1 (*ssc*). Low energy at higher frequencies is typical of low latitude regions and is related to the correlation between geomagnetic latitude and increased dB/dt levels (PULKKINEN et al., 2012). On the other hand, longer-period disturbances with larger amplitudes can be effective drivers of sustained and significant geoelectric fields and GICs.

It is not only the magnitude of the geoelectric field that is important for GIC modeling, but the orientation of the vector relative to a power network also plays a critical role (VILJANEN; PIRJOLA, 2017; DIMMOCK et al., 2020). Thus, different patterns of field vectors in a given area with the same regional mean can produce very different GICs. An accurate determination of the spatial structure of the geomagnetic variations and inferred geoelectric fields must then be taken into account with the scale of the network, which is usually done in the form of snapshots of both parameters during the most intense events.

Figure 4.9 shows the vector form of the resulting geoelectric fields at all GDS sites during three representative snapshots of each storm. Snapshots of the interpolated dB/dt for all sites at the same time instants are also shown for comparison. As expected from the larger dB_x/dt magnitudes shown in Figure 4.8, the dB/dt vector direction is preferably oriented in the NS direction. The main exception is in the *ssc* of the December storm (panel Figure 4.9d) where a NE direction is observed. On the other hand, the direction and magnitude of the geoelectric field vector vary greatly for different time instants of the magnetic storms, not necessarily following the instantaneous direction and magnitude of the dB/dt vector. In fact, the rough orthogonality between the geoelectric field vector and the dB/dt vector observed in the synthetic test in Figure 4.6 is not observed in the real situation during the two storms. Likewise, the magnitudes of the dB/dt vectors do not necessarily correspond to the magnitudes of the geoelectric field at the same time instants. This can be seen by comparing snapshots 2 and 3 of the June storm. The large NS-oriented dB/dt of snapshot 2 has an associated geoelectric field vector of small magnitude approximately parallel to this same direction. In contrast, the smallest magnitude

dB/dt of snapshot 3 is associated with a very large magnitude geoelectric field vector in the orthogonal direction.

Figure 4.9 - Selected snapshots of the modeled geoelectric field (red arrows) and interpolated dB/dt (green arrows) during the two storms. Time instants for the June storm (upper panels) and the December storm (lower panels) can be identified by the snapshot number in Table 4.2.

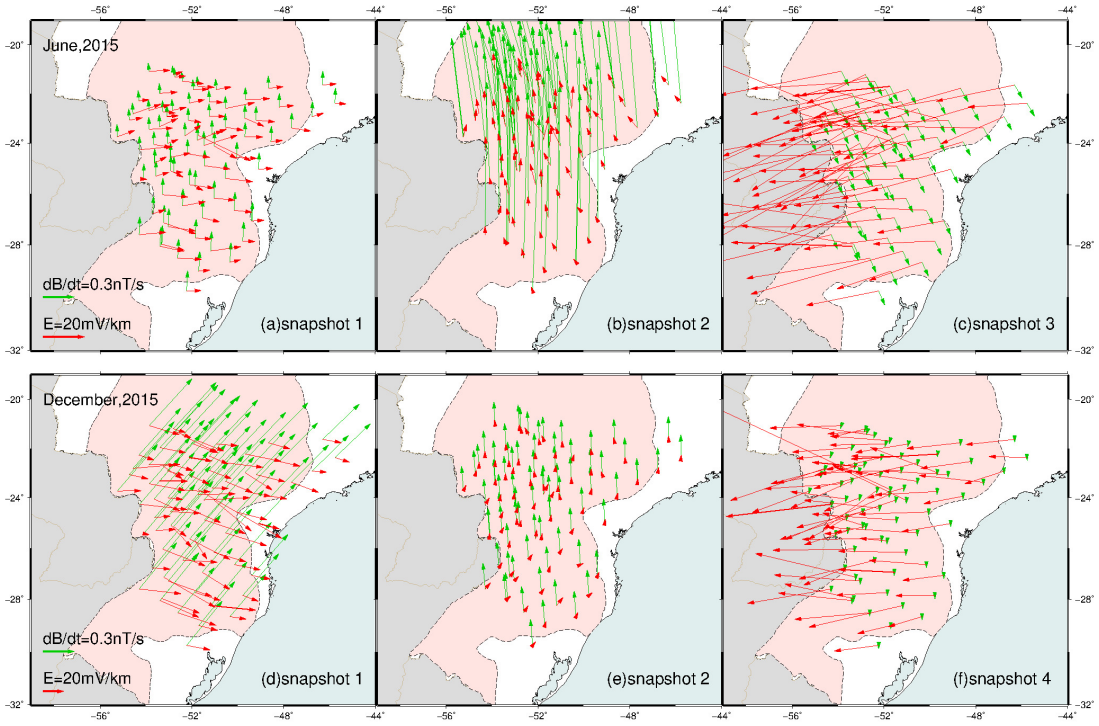

SOURCE: Author production.

These apparent discrepancies can be explained by the fact that the instantaneous geoelectric field is not only a function of the instantaneous dB/dt, but also embeds information from the preceding magnetic field. This can be shown analytically for a simplified, fully homogeneous Earth by equations relating the S-N (E_x) and E-W (E_y) components of the geoelectric field to the time derivative of the E-W (B_y) and S-N (B_x) geomagnetic field components, respectively (PIRJOLA, 2002):

$$\boldsymbol{E}_x(t) = \frac{1}{\pi\mu_0\sigma}\int_{-\infty}^{t}\frac{1}{\sqrt{t-u}}\frac{d\boldsymbol{B}_y(u)}{dt}\,du \tag{4.1}$$

$$\boldsymbol{E}_y(t) = -\frac{1}{\pi\mu_0\sigma}\int_{-\infty}^{t}\frac{1}{\sqrt{t-u}}\frac{d\boldsymbol{B}_x(u)}{dt}\,du \tag{4.2}$$

where σ represents a uniform conductivity of the Earth at the studied location. These equations indicate that the electric field depends not only on the time derivative of the geomagnetic field (shown inside the integral), but also on the previous values of the magnetic field. The weighting of the previous values of the magnetic field decreases with time by the $\sqrt{t-u}$ factor in the denominator. For a fully 3-D Earth, this is equivalent to decompose the complex impedance into a real apparent resistivity (magnitude) and a phase, where the phase describes the time lag (or lead) of the electric field relative to the magnetic field.

For snapshot 2 of the June storm, it can be seen in Figure 4.8 that the geoelectric field E_y just before the dB_x/dt peak was oscillating around -50 mV/km due to two previous CME impacts during this storm. The large positive spike in dB_x/dt from the arrival of a third CME (secondary *ssc*) causes this geoelectric field to shift to approximately -5 mV/km. For the E_x geoelectric field, the effect of the negative dB_y/dt peak was to reduce the geoelectric field from 25 nT/km to 10 mV/km. Due to the inverted polarization of the dB/dt large spike in relation to the preceding values of the geoelectric field, the magnitude of the instantaneous geoelectric field vector resulting in this snapshot is low (Figure 4.9).

On the other hand, Figure 4.8 also shows that the negative spike in dB_x/dt from snapshot 3 of the June storm follows a sequence of several negative spikes in dB_x/dt during the magnetic storm main phase. This causes an excursion of the geoelectric field E_y to values below -120 mV/km before that time instant (long period variation). Thus, the large negative magnitude of the geoelectric field E_y in snapshot 3 is associated with the cumulative effects of all these several dB_x/dt with the same negative polarity giving rise to a long period undulation. Similarly, the geoelectric field E_x is enhanced in the same snapshot by an earlier positive dB_y/dt sequence. The result is the large magnitude observed in the instantaneous geoelectric field vector seen in Figure 4.9, even though the dB/dt vector magnitude is not significant at that time instant.

Due to the close link between the time derivative of the geomagnetic field and the level of the induced geoelectric field, dB/dt has been proposed as a reasonable proxy for GIC activity (VILJANEN et al., 2001). However, some examples are found in the literature indicating the inadequacy of the dB/dt metric to characterize these in-

duced currents (TRICHTCHENKO; BOTELER, 2006; WATARI et al., 2009). The June 2015 storm discussed in this thesis represents another case study where the dB/dt metric fails, in this case associated with the relationship of the geoelectric field to previous values of the magnetic field. In fact, the unusual characteristics of this storm had a major impact on this relationship between instantaneous dB/dt and geoelectric field vectors. A similar result on the inadequacy of dB/dt as a proxy for GIC activity during this storm was obtained by Heyns et al. (2021) when analyzing long-period pulsations. It should also be considered that the linear relationship between the local dB/dt and the local geoelectric field, or the power-line average of the ground-level geoelectric field (which determines the GICs), breaks down in the presence of significant spatial heterogeneity in the Earth's electrical conductivity. A general discussion of the effects of 3-D variations in Earth's resistivity on the ground geoelectric field and the GICs can be found in Kelbert (2020).

4.1.3 GIC estimation

Following the LP method, the calculation of GIC in transmission lines requires the values of the geoelectric fields in each cell of the ground resistivity model where the substations are located and also in those through which the transmission lines pass. Although the geoelectric field can be computed for each horizontal cell of the 3-D model (10×10 km scale), our choice was to use the derived values in the observed data cells ($\sim 100 \times 100$ km scale) and fill in the necessary empty cells with an interpolation technique. As a first approximation, the nearest neighbor method that produced reliable interpolation results between cells containing measurement sites and extrapolated fields with apparently less significant errors was chosen.

Accurate values of the power network elements for GIC calculations are not available and therefore estimates of substation grounding and transformer winding resistances had to be made. According to the bidding terms and prescribed technical requirements for transmission line installations in Brazil, the resistance per unit of length must range from 0.0174 Ω/km to 0.028 Ω/km for a 525 kV power grid (ANEEL, 2003-2019). As we mainly look for the most vulnerable regions in the network, the minimum value (0.0174 Ω/km) was used to obtain the maximum GIC magnitudes. Furthermore, according to the ANSI/IEEE80 norm (IEEE, 2007) that electricity companies in Brazil must comply with, the maximum recommended grounding resistance is 1 Ω. Based on the best fit for GICs measured in previous studies of a Brazilian network (ESPINOSA et al., 2019), a value of 0.43 Ω was assumed for all grounding resistances.

The instantaneous GIC magnitudes calculated by the LP method on the network nodes during the six selected snapshots are represented by green circles in Figure 4.10. The geoelectric field vector centered on the corresponding GDS site location is also shown (same as Figure 4.9). The maximum magnitudes of the modeled GICs are observed in snapshots that are representative of the main phase of both storms (snapshot 3 for June and 4 for December). Two substations stand out as those with the highest GIC magnitude. One corresponds to node 2 in the northern part of the network, which is located in the region where the greatest geoelectric field magnitude is observed and its vector direction is approximately parallel to the transmission line direction. The other corresponds to node 12 located in the central part of the Paraná basin, a substation connecting several mainly E-W branches of the grid and also a region with a strong geoelectric field. Modeled GIC magnitudes were 9.08 A (node 2) and 7.69 A (node 12) for the June storm and 4.75 A (node 2) and 5.03 A (node 12) for the December storm. The minimum magnitudes were modeled for substation 6, located on the high conductivity anomaly along the basin axis, and substations 16-20 and 22-23, located on the strong conductors bordering the continental margin. The maximum GIC magnitudes for these substations were observed in the June storm, but were less than 2.5 A.

Figure 4.10 - Geoelectric field and GIC were calculated during the selected snapshots for the June and December 2015 storms. Red arrows show the instantaneous vector geoelectric field, highlighting those chosen for the GIC calculation. Green circles are the instantaneous GIC modeled on the 525 kV transmission line substations (in blue). GIC magnitude is proportional to the diameter of the circles, with the highest value at substation 2 for snapshot 3 of the June storm corresponding to 9.08 A.

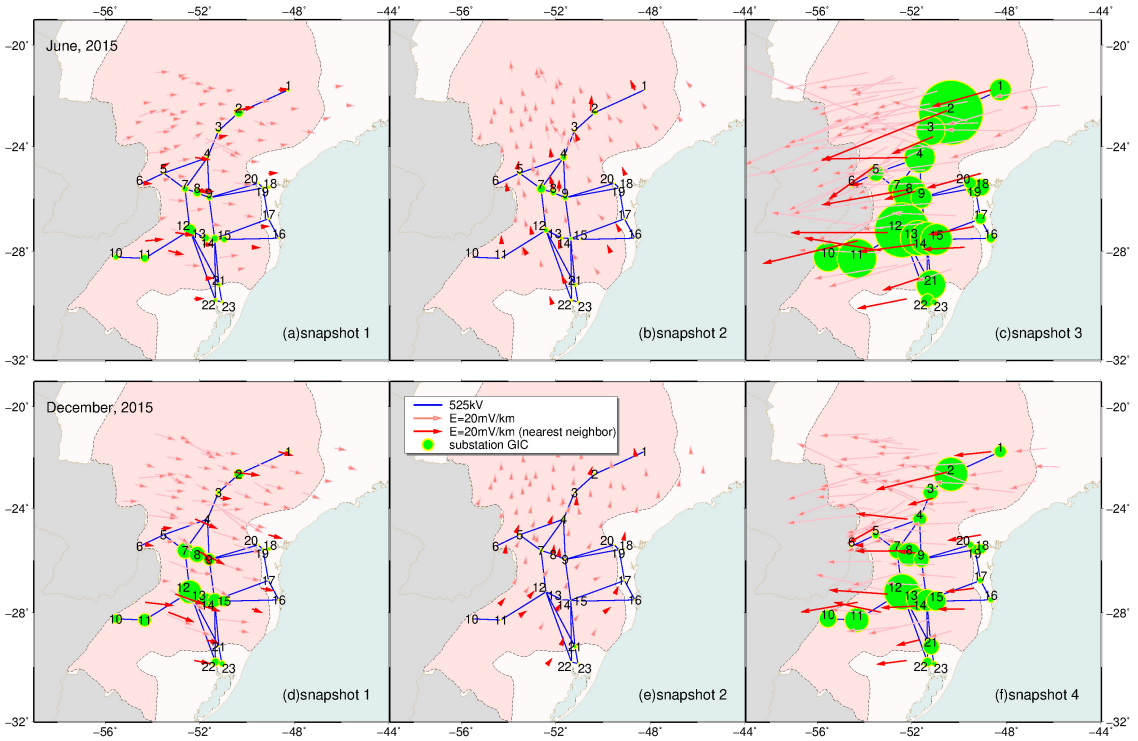

SOURCE: Author production.

Figure 4.11 shows time series of GIC magnitudes calculated for each substation in the simplified power grid during the June storm, the strongest of the two storms analyzed. Two effects are highlighted in this figure: substations with opposite GIC polarity and substations with large GIC. Substations with opposite GIC polarity to the remaining substations are concentrated along a NE-SW branch on the northern edge of the power grid (substations 1-5). The inverted GIC polarity is likely associated with the edge effect whereby the GIC typically flows to/from the ground through substations at the edge of the network (BOTELER; PIRJOLA, 2017).

Figure 4.11 - Time series of the resulting GIC modeling at the 23 substations of the simplified 525 kV transmission line during the June storm. Substations with the highest GIC magnitudes are highlighted in yellow and indicate possible nodes for future installation of GIC sensors.

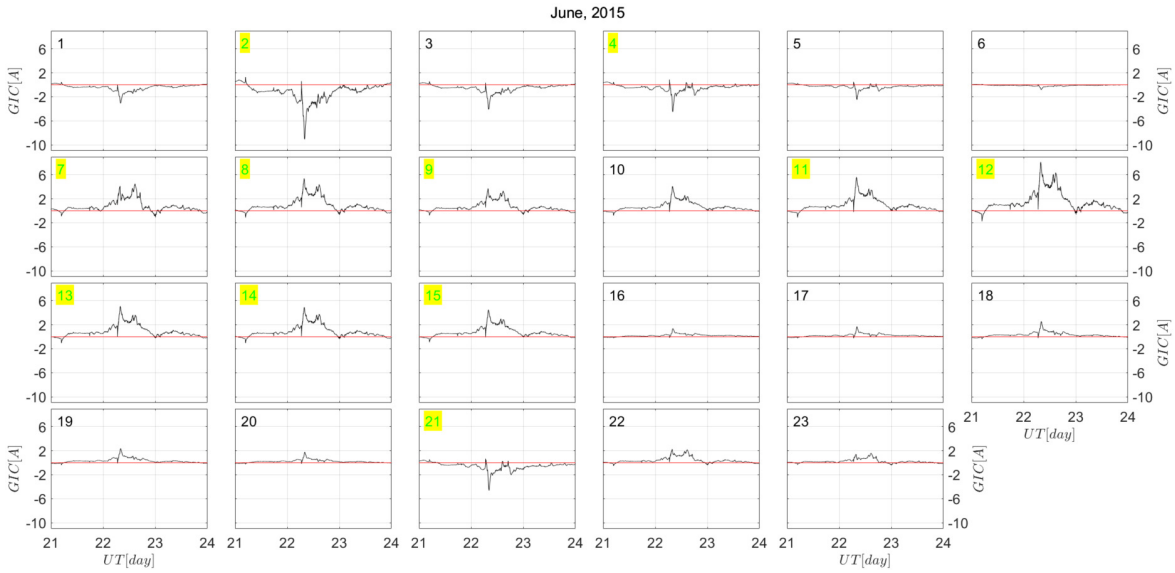

SOURCE: Author production.

On the other hand, it would be expected that geometric properties of the grid (edge effect) would cause large GICs to occur at the corners of the grid and this is observed in many studies worldwide (TORTA et al., 2014; ZHENG et al., 2014). However, Figures 4.10 and 4.11 show that the substations experiencing large GICs are found in the central part of the network, where the transmission lines are oriented mainly east-west and a higher concentration of substations is observed, and in the localized region of high resistivity under substation 2 of the northern branch. The possibility of larger GICs concentrated in the inner parts of the grid rather than its edges was pointed out in simulation studies for the Japanese network (NAKAMURA et al., 2018). They indicated that the topology of the network, its relationship to the direction of the geoelectric field and localized effects of ground resistivity can generate larger GICs in different parts of the network.

The substations with the highest GIC in Figures 4.10 and 4.11 can then be related to various effects, including the predominantly E-W direction of the geoelectric

field with higher magnitude, the concordant E-W direction of transmission lines in the central part of the grid, and lower subsurface conductance values in the same region beneath the Paraná basin. Furthermore, the 3-D model shows strong crustal high conductivity anomalies along the coastline, which contributes to dampening GIC estimates in this area. More importantly, these figures indicate possible substations where to install GIC sensors to validate the modeling methodology. It should be noted, however, that the results were based on a simplified power grid network topology and configuration (i.e., the equivalent electrical circuit). This type of GIC estimation, which assumes an average grounding resistance, neglects knowledge of the power grid as a complete equivalent electrical circuit (i.e., with time-varying complex admittance to represent all branches, generators and loads, as well as details of transformer windings, etc.). There may therefore be an unknown significant impact on both the magnitude and phase of the modeled induced current waveform.

4.2 GIC estimation in a power network of north-northeast Brazil

GIC activity has been extensively studied at high latitudes due to the initial paradigm of first-order influence on GIC activity related to the higher dB/dt amplitudes that are observed in auroral latitude regions. Until recently, GIC studies at very low latitudes and in the equatorial region were very rare. The few studies performed have inferred potential effects of interplanetary shocks in the equatorial region, noting that the amplification of the magnetic signature increases the susceptibility of this region to GICs (CARTER et al., 2015; OLIVEIRA et al., 2018). Also, according to Carter et al. (2016), sudden increases in the solar wind dynamic pressure causing sudden increases in the magnetopause current and consequently changes in the resulting magnetospheric-ionospheric current systems would be the main drivers of equatorial GICs. Other studies of the effects of the EEJ current system on GICs have mainly focused on comparisons between geomagnetic field derivatives related to a limited number of stations located in the equator region (maximum 2 stations), comparing dB/dt ratios from different latitudes (CARTER et al., 2015). Kasran et al. (2018) considered real scenarios in a database of reported power grid failures with GIC impact. They used the nearest ground magnetic station within $\pm 15^{\circ}$ of magnetic latitude to estimate a magnetic rate-of-change threshold of 30 nT/min that would affect a power system. However, there is no known effective study of GIC modeling for the equatorial region in the literature.

This section presents a case study of GIC modeling in the north-northeast Brazilian sector. The main goal is to analyze the impact of the equatorial electrojet current system on the induced geoelectric field amplitudes that could contribute to GIC amplifications. A regional study is developed considering a synthetic situation for generating GICs using magnetic field data acquired during $1990 - 1991$, 3-D conductivity structure in the subsurface and a 525 kV power transmission line.

4.2.1 Dataset description

The dataset available for GIC modeling in the Brazilian equatorial region is here described, following the same sequence as in Subsection 4.1.1.

4.2.1.1 Available geological and geophysical information

The South American platform in north-northeast Brazil is composed of a series of crustal segments, which are the result of the Late Neoproterozoic–Eopaleozoic Brasiliano–Pan African agglutination process of West Gondwana by the general collage of the Amazonian, São Luís/West Africa and São Francisco/Congo cratons (ALMEIDA et al., 1981). Neoproterozoic fold belts surround these cratonic landmasses. Tectonic adjustments after the cessation of the Brasiliano orogeny formed rift systems that reactivated major preexisting zones of weakness, creating space for sediment accommodation and the formation of graben-like structures. Processes of subsidence along these unstable crustal regions formed the large Paleoproterozoic intracratonic Parnaíba basin that currently covers much of the north-northeast region of Brazil (VAZ et al., 2007).

The Parnaíba basin (Figure 4.12) comprises an area of approximately $600,000$ km^2 and, based on a few deep boreholes and interpretations of potential methods and seismic lines, the sedimentary-volcanic package has a maximum thickness of about 3500 m at its depocenter (CASTRO et al., 2014). It has a relatively thick lithosphere ($160-180$ km) (DALY et al., 2014, and references therein) and is bounded to the north by the São Luis craton, to the east by the Borborema province, to the south by the São Francisco craton and its sedimentary cover, and to the west by the Amazonian craton and sedimentary cover. The basin encompasses successive sub-basins with distinct genesis and ages: a cratonic sag sub-basin, filled with Ordovician to early Triassic marine sediments, an intermediate interior fracture basin, which combines continental sedimentary rocks and basaltic flows of the Jurassic and Cretaceous, and two other sub-basins that occur on the northern and southern edges, deposited respectively in marine and desert environments. Its stratigraphy comprises thick

epicontinental sequences, mostly of siliciclastic nature, separated by widespread unconformities (GÓES et al., 1990). On the basis of petrography and Rb–Sr and K–Ar geochronology of basement rocks, a Proterozoic cratonic nucleus was inferred below the central part of the basin (CORDANI et al., 1984) and, in the eastern margin, the Transbrasiliano lineament seems to control its evolutionary history and shape (CUNHA, 1986).

Also in its eastern region, aeromagnetic data reveal a series of NE–SW elongate anomalies interpreted as related to several basement grabens in these these directions (NUNES, 1993). This deep NE–SW structure is reinforced by combined EM surveys on the southern and eastern margins of the basin (MEJU et al., 1999), which show high conductivity anomalies relative to the adjoining basement displaying the same elongate structure. Previous analyzes of our GDS data using thin-sheet modeling by Arora et al. (1999) highlighted the presence of a NNW-SSE oriented high conductivity belt (named LINK anomaly by these authors) in the east-southeast portion of the basin. They also identified highly conductive anomalies in areas of intense magmatic activity, indicating the presence of a large conductive block confined to the central part of the basin, called Parnaíba Basin Conductivity Anomaly (PBCA).

Figure 4.12 - Regional geological map of north-northeast Brazil, with emphasis on the Parnaiba basin (modified from Bizzi et al. (2001)). Locations of GDS (white circles) and broad-band MT (black triangles) sites are shown. Geological periods of outcrops are: CZ = Cenozoic; Mz = Mesozoic; Pz = Paleozoic; Pr = Proterozoic; Ar = Archean. The inset shows the study area in the Brazilian territory with the Parnaiba basin in bold outline.

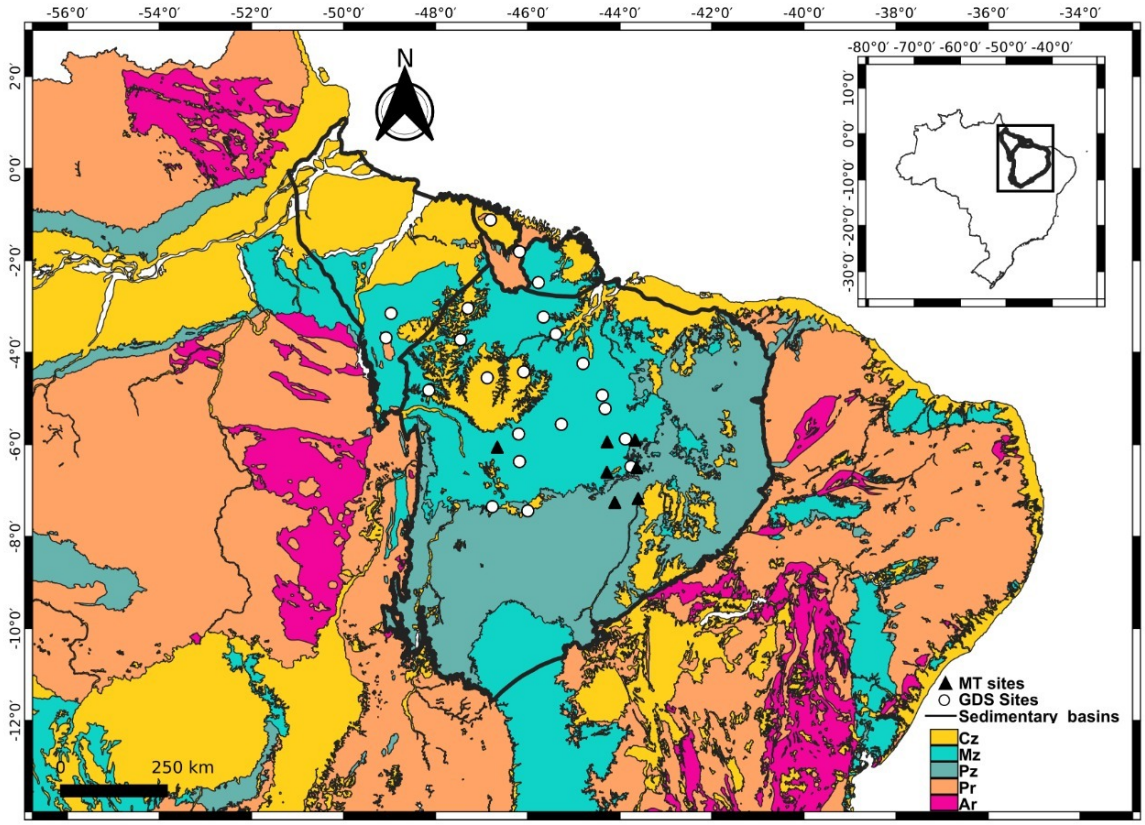

SOURCE: Adapted from Bizzi et al. (2001).

Some studies were carried out more recently to obtain geophysical information on the basement structure of the Parnaíba basin (DALY et al., 2018, for more details). Regarding the resistivity distribution, Padilha et al. (2017) analyzed MT data from the eastern part of the Parnaíba basin and northwest of the Borborema province and identified a resistive cratonic keel below the central part of the basin, hidden under the sedimentary package, and conductive zones along the crust and upper mantle to the east. The conductive structure was interpreted as a suture zone correlated to the Neoproterozoic Brasiliano collage. Solon et al. (2018) mapped the lithosphere along

an east-west 1430 km profile crossing the basin. Three distinct patterns from 3-D inversion were observed: resistive crustal blocks in the western and eastern regions and zones of increased conductivity in the central continental crust, unexpected in a crystalline crustal basement. This conducting crust and upper mantle was interpreted as related to the Brasiliano orogeny or igneous events of the Triassic and Cretaceous. Also based on MT studies, Rocha et al. (2019) mapped the lithosphere through a NNW-SSE profile and observed distinct patterns from 3-D inversion: a resistive crustal block in the central part of the basin, also interpreted as the cratonic block below from the central part of the basin, and a mosaic of resistive and conductive zones to the east related to the extensive fold belt of the Borborema Province.

4.2.1.2 3-D electrical resistivity structure beneath the central part of the Parnaíba Basin

Most 3-D inversions previously carried out in the Parnaíba Basin used MT surveys established along one or more linear profiles (PADILHA et al., 2017; SOLON et al., 2018; ROCHA et al., 2019). Thus, an overview of lateral variations in mapped structures is compromised. The 3-D inversion presented in Section 3.2 coupled regional GDS data (240 to 10240 s) and localized MT sites (240 to 2560 s) to provide a lateral and in-depth model of the resistivity variation in the crust and upper mantle under the Parnaíba basin.

Figure 4.13 shows 4 horizontal sections of the 3-D model at depths representative of the upper crust (10 km), middle crust (25 km), lower crust (40 km) and upper mantle (55 km). The minimum period (240 s) used in the inversion is constrained by the GDS data and does not allow adequate resolution at shallow depths. Because of this, the scattered resistivity distribution seem at 10 km depth reflects the large-scale and non-uniform distribution of measurement sites. This pattern indicates lack of information about near-surface distortion effects and aliasing caused by the lack of sampling (MEQBEL et al., 2014), generating a rougher and poorly resolved structure. The preliminary and simplified interpretation of the model will focus on slices at depths of the middle-lower crust ($25-40$ km) and upper mantle (55 km), considering that the crust-mantle boundary in this region is ~ 40 km (ASSUMPÇÃO et al., 2013).

Figure 4.13 - Horizontal slices of the 3-D resistivity model at depths of $z \sim 10$ km, $z \sim 25$ km, $z \sim 40$ km and $z \sim 55$ km. The color scale is logarithmic and covers the range $10^0 - 10^3$ Ωm. Projections of the continental margin (black contour line), Parnaíba basin limits (white dashed line), GDS (black points) and MT (white points) sites on the surface are also shown.

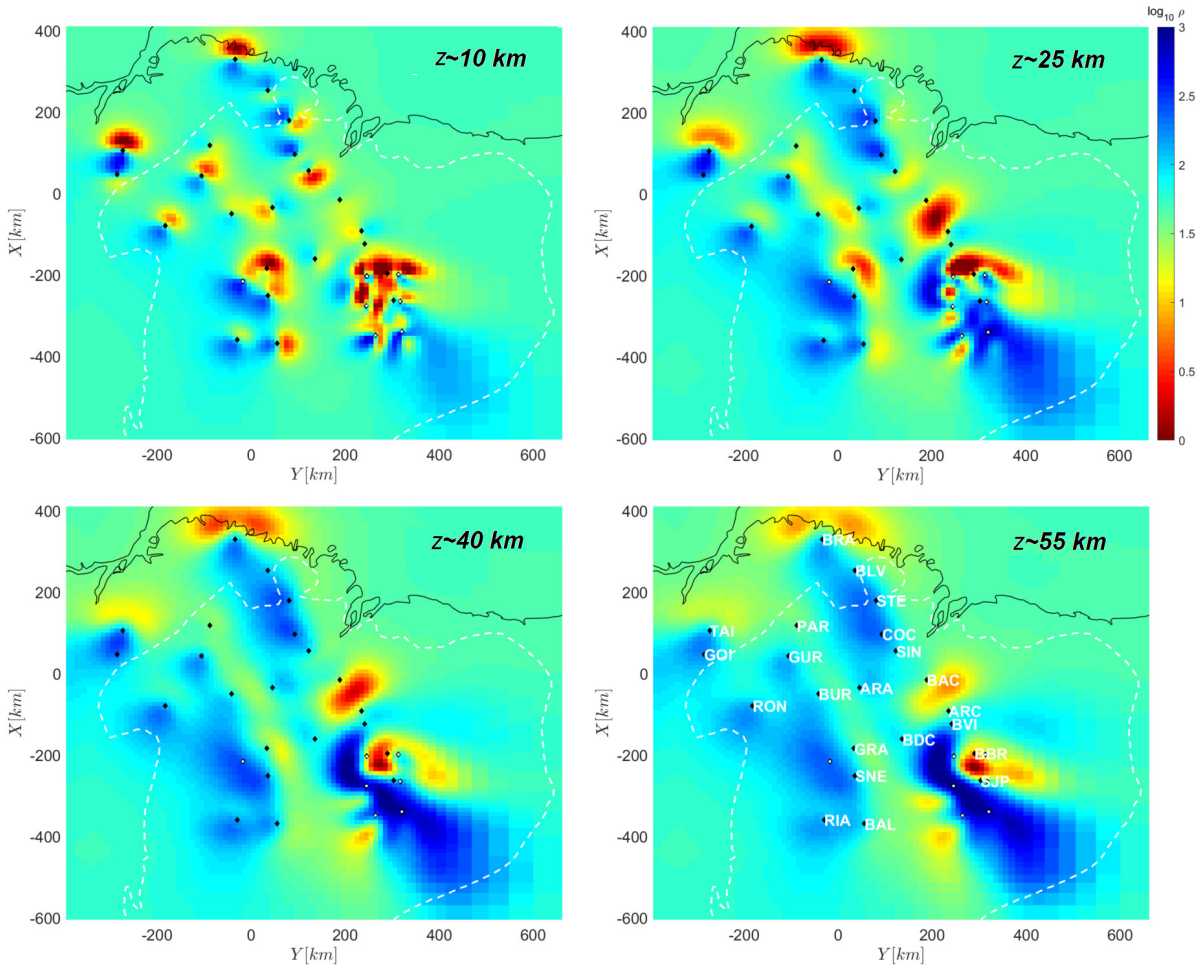

SOURCE: Author production.

The resistivity distribution for the lower crust and mantle is well delineated and shows the presence of resistive blocks intercepted by conductive structures. The two main conductors previously suggested by Arora et al. (1999) in GDS-only modeling can be identified. LINK appears as a well-resolved elongated deep conductor in the NNW-SSE direction through the central part of the area, while PBCA can be identified as the strong conductor located in the western part of the GDS array,

between the BBR and BAC stations. The E-W profile of Solon et al. (2018) also maps the conductive bodies in the basement under the central part of the basin, but extends them laterally for distances much further east.

For modeling the GDS data, Arora et al. (1999) used thin-sheet techniques that have no depth resolution. Therefore, they interpreted the conducting bodies as situated in the upper crust. LINK was interpreted as a sedimentary channel joining the Parnaíba and Marajó basins, and PBCA as a graben-like structure situated at the base of the sedimentary package. The joint GDS-MT inversion performed here imposes much better constraints given by the depth resolution of the MT data. It can be seen that LINK and PBCA are much deeper conductors that permeate the entire crust and also have signatures in the upper mantle. Similar to the previous MT survey by Padilha et al. (2017) for the eastern part of the Parnaíba basin and western Borborema province, the lithosphere in the central part of the basin appears dominated by a mosaic of resistive blocks separated by more linear conductive structures. The presence of a postulated single resistive block under the central part of the basin (Parnaiba block) is not confirmed. A more comprehensive interpretation of the 3-D resistivity model would need to integrate other geological and geophysical information and is beyond the scope of this work.

4.2.1.3 Ground magnetic stations time series

To achieve the main goal of this thesis of using geomagnetic data with high acquisition cadence (1 s) and 3-D underground resistivity to evaluate the effects of GICs on transmission lines during solar cycle 24 magnetic storms, we initially evaluated the distribution of EMBRACE and INTERMAGNET stations in the South America equatorial region. This is shown in Figure 4.14, where the position of the magnetic *dip equator* for the year 2015 and the presumed limits for the EEJ effects to be observed in geomagnetic surface measurements are also presented. The distribution of stations is obviously inadequate for our study, as there is a large concentration in the eastern part of the magnetic equator, one in the area affected by the EEJ (ttb station) and only one to the western part of the magnetic equator (kou station). This distribution makes it impossible to apply the SECS method to interpolate the magnetic field, especially considering the horizontal inclination of the geomagnetic field. Furthermore, the area where the 3-D resistivity model discussed in the previous section is located is currently positioned east of the magnetic equator region, outside the EEJ effects. Thus, even if it were possible to interpolate the geomagnetic field for the region where the 3-D model is available, it would not be possible to evaluate

the EEJ effects on the estimated geoelectric fields at the surface.

Figure 4.14 - Location of the EMBRACE and INTERMAGNET geomagnetic stations in the South America equatorial region. The magnetic *dip equator* $I = 0°$ (solid blue line) and boundaries north and south of the expected EEJ effects on the ground (dashed blue lines at $I = \pm 6°$) are also shown. Geomagnetic coordinates derived using IGRF-13 coefficients.

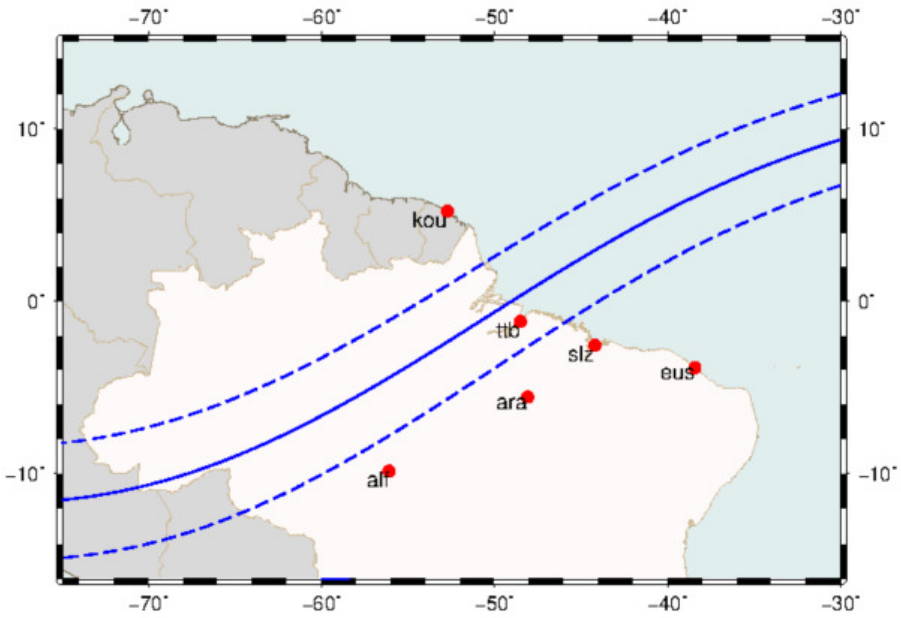

SOURCE: Author production.

Having discarded the EMBRACE magnetometers to carry out the planned studies in the Brazilian equatorial region, we return to the GDS survey used to model the 3-D electrical resistivity of the Parnaíba basin. In addition to mapping the internal structure of resistivity on a regional scale, with a station spacing of $50-100$ km, this array also aimed to establish parameters of the EEJ currents (RIGOTI et al., 1999). Thus, the layout of the fluxgate magnetometers was arranged roughly along three profiles that run perpendicular to the *dip equator* at that time. They were deployed to operate simultaneously at 29 stations of the array to measure the two horizontal components and the vertical component of the geomagnetic field. Measurements started on November 22, 1990, with the last magnetometer operating until March 25, 1991. During this interval, the three magnetic field components were sampled

with an acquisition rate of 1 minute and a resolution of 1 nT (CHAMALAUN; WALKER, 1982). Of the 29 magnetometers installed during the survey, 22 were selected for this study based on total acquisition time and data quality (Figure 4.15). Also, of the three profiles in which the magnetometers were originally installed, only one (P3) has adequate data for analysis at all stations. Although all calculations have been made for the 22 available stations, the graphs to be presented below will prioritize the results along this profile. The objective is to verify the variation of the geomagnetic and geoelectric fields as a function of the distance from the *dip equator*. Details on general magnetometer operation, data acquisition and reduction steps are provided in Rigoti et al. (1999).

Figure 4.15 - Map showing the layout of the magnetometer sites (green circles) and profiles P1 ($tai - bal$), P2 ($par - sne$) and P3 ($bra - sjp$) discussed in the text. Geomagnetic sites with available data for the March 1991 storm are shown with red triangles. Areal extent of the Parnaíba basin in pink. The magnetic *dip equator* $I = 0°$ (solid blue line) and limits north and south of the EEJ effects (dashed blue lines at $I = \pm 6°$) were derived for the measurement period (November 1990 - March 1991) using IGRF coefficients.

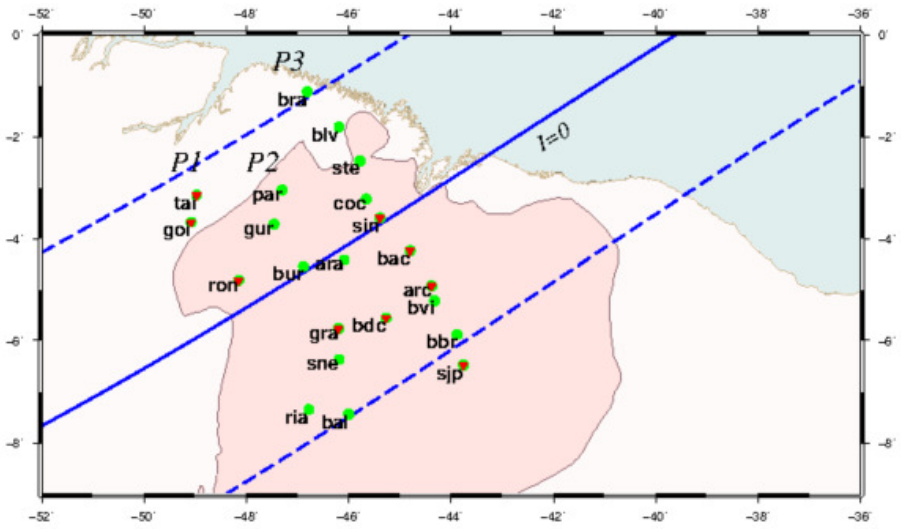

SOURCE: Author production.

Five magnetic storms were recorded during the operation of the array (Table 4.3). According to the classification of Table 2.1, one of these storms can be classified as severe, one intense, one moderate and the others two as weak. Unfortunately,

the strongest storm occurred in the final period of data acquisition and only 9 magnetometers had any record of its occurrence. Due to the distribution of these magnetometers across the array (Figure 4.15), this storm cannot be used in our analyses. Also the February 1991 storm was very weak and did not result in significant variations in the geomagnetic field. The other storms will be analyzed and are identified as S1 (November 1990), S2 (January 1991) and S3 (January-February 1991).

Table 4.3 - List of periods with geomagnetic disturbances from November 1900 until March 1991.

No.	**Date**	Dst[nT]	$\frac{dX}{dt}$ [nT/min]
1(S1)	26-28 Nov. 1990	−135	42
2(S2)	23-25 Jan. 1991	−37	−14
3(S3)	31 Jan.-2 Feb. 1991	−79	−17
4	22-24 Feb. 1991	−26	18
5	24-28 Mar. 1991	−298	151

SOURCE: Author production.

The intense geomagnetic storm in November 1990 (event S1) was associated with a large sunspot region (AR6368) that produced a sequence of eight solar flares on November 26-28, 1990 (TAYLOR, 1990). The time series of the geomagnetic field recorded by the 10 stations along the P3 profile is shown in Figure 4.16 for these 3 days. The initial phase of the storm lasted 6 h, the main phase $\sim$ 10 h and the recovery phase remained for 58 h. The first most energetic event, on November 26, triggered an interplanetary shock that impacted the magnetosphere around 23:37 UT of that day (UDDIN et al., 1995), corresponding to 20:37 LT in the South American sector. This shock, corresponding to the *ssc*, is indicated by the letter "a" in the figure. The geomagnetic field experienced the most significant variations during the main phase of the storm that occurred on November 27 and is indicated by the "b" interval. Important for our study is that this main phase took place entirely during daytime in the South American sector. To enhance visualization, the daytime period in local time is presented by white stripes, while the nighttime period by gray stripes (this same representation will be used in subsequent figures). The largest amplitudes and rates of change of the geomagnetic field during this storm were observed at the

station *bac* situated south of the *dip equator* (*dip latitude* $= -0.79$). The maximum rate of change at this station was 42 nT/min, recorded during the main phase at 10:22 UT on November 27, when the amplitude of the geomagnetic field reached 281 nT in the northward component.

Figure 4.16 - Geomagnetic field time series (left panels) and time derivatives (right panels) for the northward (ΔB_x) and eastward (ΔB_y) components measured at the ten stations of the P3 profile during the geomagnetic storm on November 26-28, 1990 (event S1). The numbers on the right correspond to the *dip latitude* of each station during data acquisition and time intervals "a" and "b" are discussed in the text.

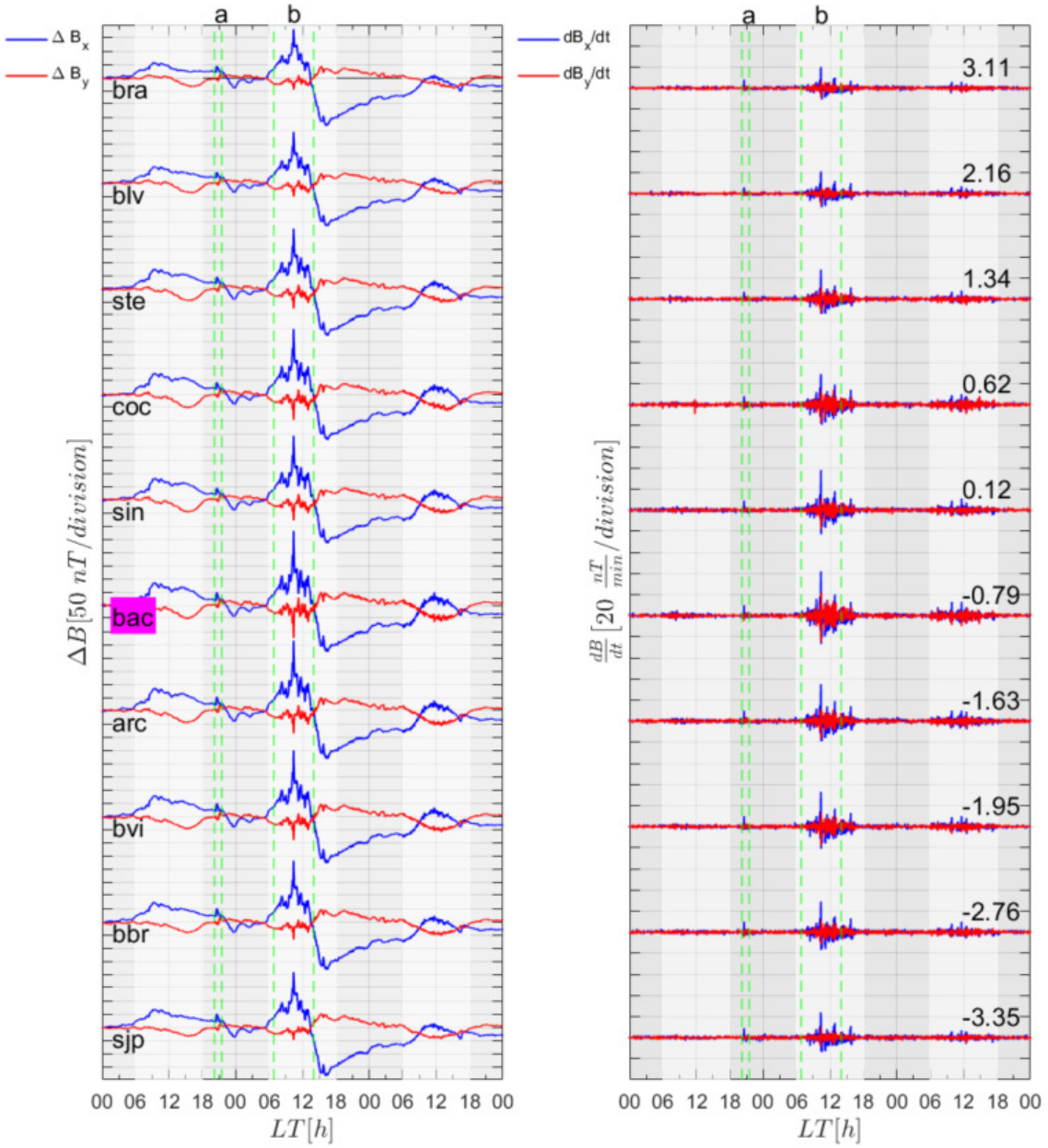

SOURCE: Author production.

An increase in solar activity was recorded in January 1991 due to the evolution of two active regions (AR6462 and AR6466). Associated with this solar activity, a geomagnetic disturbance (event S2) was recorded in ground magnetometers from January 19 to 25, 1991. Figure 4.17 shows the variation of B_x and B_y components and their respective rates of change during January 23-25, 1991. Around local sunset (17:30 LT) on January 23, a *ssc* was observed during daytime in the South American sector (interval "a" in the figure) with maximum rate of change of 8 nT/min at station *bac*. Another solar flare on January 24 caused magnetic field disturbance, observed during daytime in the South American sector (10:00-15:00 LT on this day; interval "b"), which generated a rate of change of less than 10 nT/min for both geomagnetic components. The most energetic event in this period occurred on January 25 (UDDIN; VERMA, 1996), leading to small but rapid changes in the geomagnetic field (interval "c"). During local noon of the same day (about 10:00-16:00 LT), the geomagnetic field exhibited a period with more significant increases in the rate of change. The maximum rate of change was (17 nT/min) at 15:53 LT on January 25, recorded in *coc* for the dB_y/dt component.

Figure 4.17 - Geomagnetic field time series (left panels) and time derivatives (right panels) for the northward (ΔB_x) and eastward (ΔB_y) components measured at the ten stations of the P3 profile during the geomagnetic storm on January 23-25 1991 (event S2). The numbers on the right correspond to the *dip latitude* of each station during data acquisition and time intervals "a", "b" and "c" are discussed in the text.

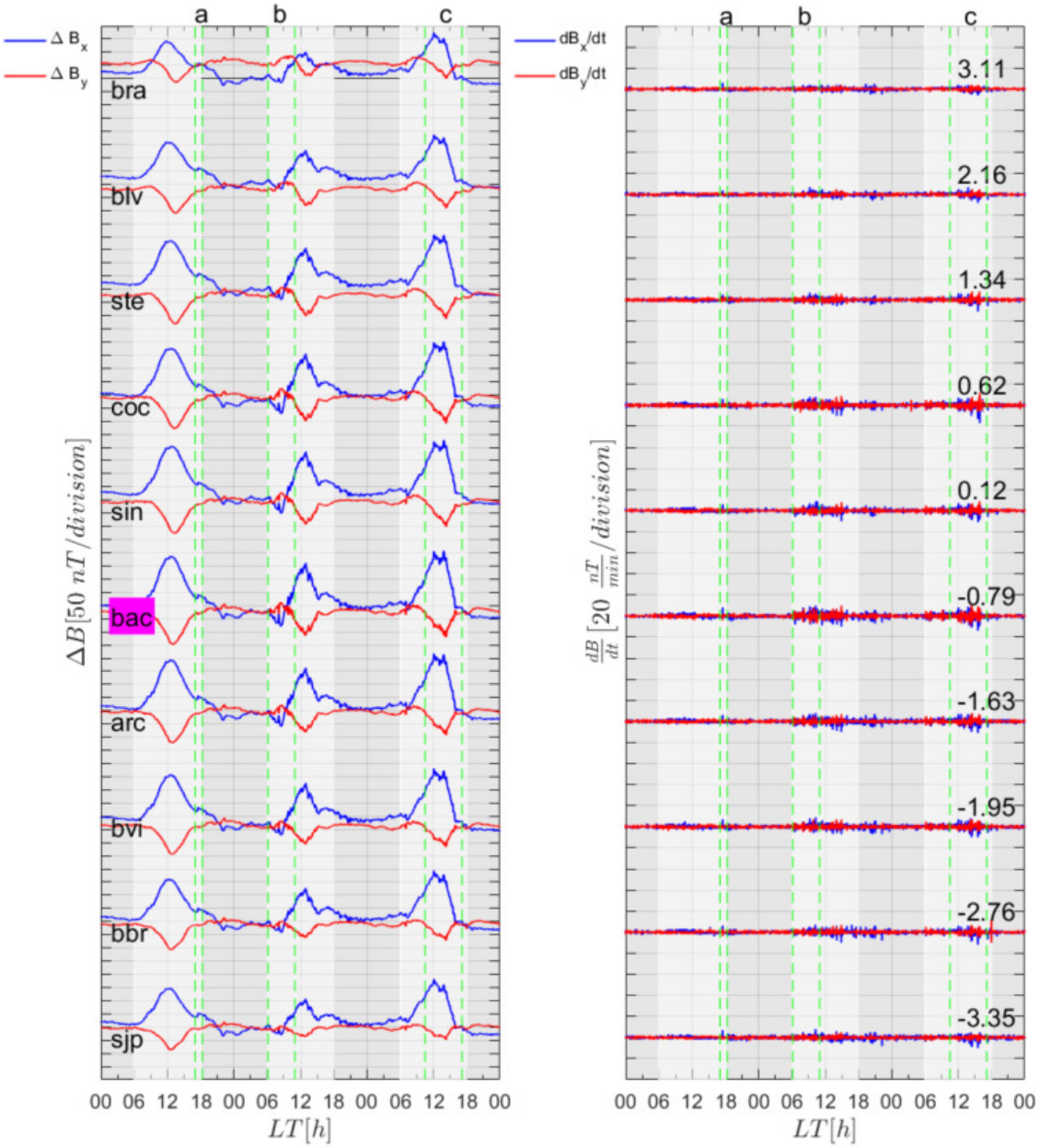

SOURCE: Author production.

Figure 4.18 shows the signature of the moderate geomagnetic storm and its time derivative of the horizontal components (dB/dt) that occurred between January 31 and February 2, 1991 (event S3). This perturbation was associated with a solar proton event (10>MeV) coming from the active region RA6469, starting on January 31 at 11:30 UT with peak flux at 16:20 UT (TAYLOR, 1991). This event boosted the geomagnetic field variation recorded during local daytime (12:00-14:00 LT) in our magnetometers and indicated as the "a" interval in the figure. On February 1, another interplanetary clash was recorded around 15:42 LT (daytime), leading to a significant decrease in the geomagnetic field ("b" interval). In this interval, the maximum rate of change in *ssc* for the component B_x was observed in station *bvi* (66 nT/min) and the minimum in *ste* (42 nT/min). After the *ssc*, the maximum amplitude of the rate of change was 38 nT/min observed at the station *bac*. Although the global geomagnetic field disturbances during this storm were not strong ($Dst = -79$ nT), this shock during the "b" interval produced the strongest dB/dt magnitude recorded for our three case studies in the Brazilian equatorial region.

Figure 4.18 - Geomagnetic field time series (left panels) and time derivatives (right panels) for the northward (ΔB_x) and eastward (ΔB_y) components measured at the ten stations of the P3 profile during the geomagnetic storm on January 31-February 2, 1991 (event S3). The numbers on the right correspond to the *dip latitude* of each station during data acquisition and time intervals "a" and "b" are discussed in the text.

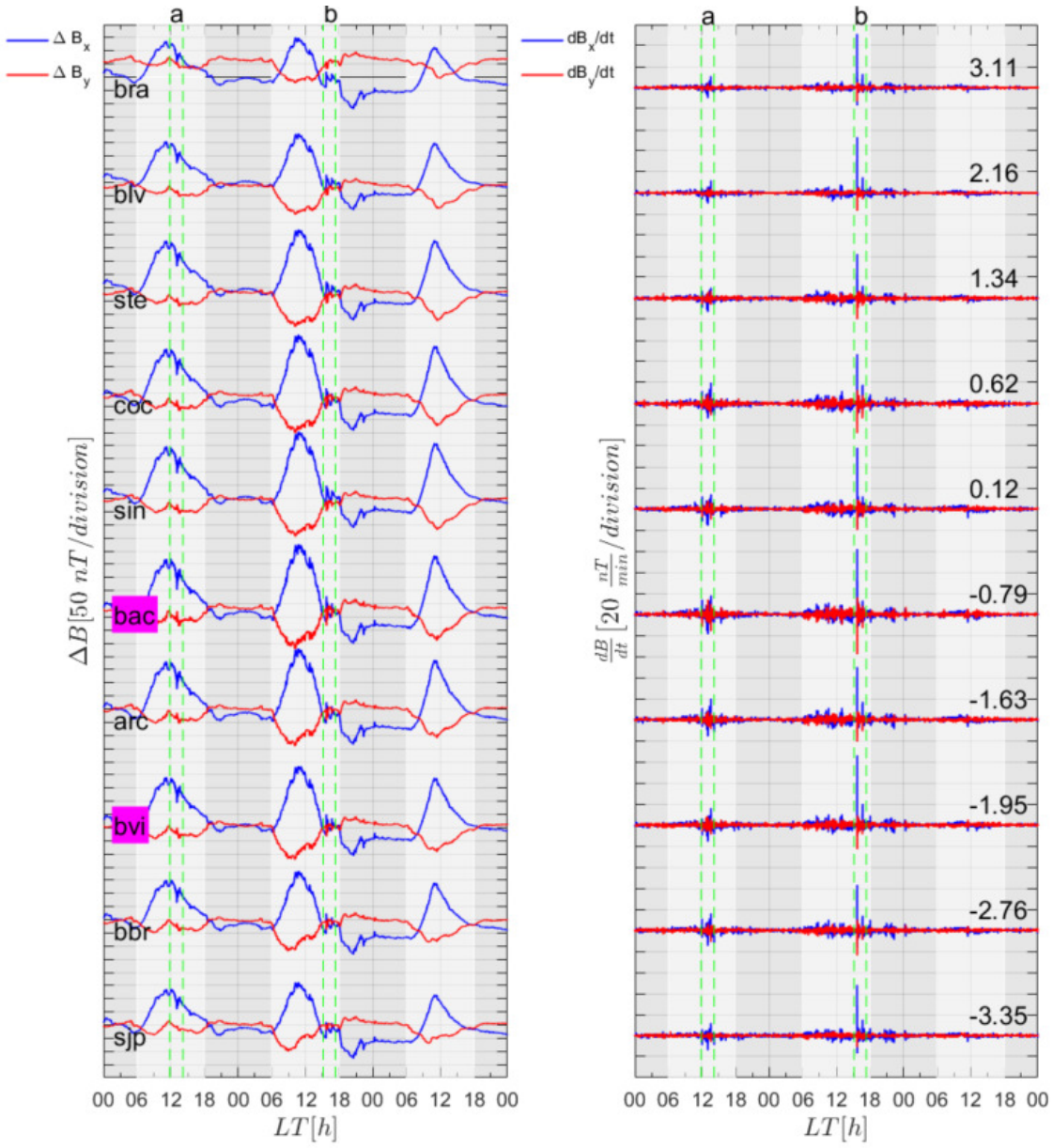

SOURCE: Author production.

The graphs above show some well-known features of the geomagnetic field at low latitudes and in the equatorial region. A clear polarization is observed along the magnetic meridian, with the highest amplitudes and rates of change in the B_x component. Also, the largest variations are located around the *dip equator*, but not exactly below it. In general, the greatest variations during storms are located in the *bac* station ($dip = -0.79$). This result is in agreement with an EEJ modeling for quiet days by Rigoti et al. (1999), which shows that the average position of the EEJ center was south of the *dip equator*. In addition, the known daily and seasonal variability of the EEJ currents should be considered (FORBES, 1981; KANE; TRIVEDI, 1982).

Possible induction effects on geomagnetic field magnitude recorded by our magnetometers cannot be ruled out. Significant inducing effects resulting from regional underground conductivity were inferred by Arora et al. (2001) for station *bac*. These authors showed that a conductive body close to this station (see model in Figure 4.13) induces anomalous magnetic fields, amplifying horizontal geomagnetic components mainly during periods of moderate geomagnetic disturbance. This interpretation stems from the analysis of other stations with a similar location in relation to *dip equator* and which do not show anomalous amplification. This behavior has been observed in different regions of the world with high conductivity structures (PADILHA et al., 2017, and references therein) that typically amplify the amplitude of geomagnetic variations by a few tens of percent. The relationship between the polarity of the geomagnetic field and lateral inhomogeneities of the electrical conductivity on Earth defines the preferential orientation of the geoelectrical currents flowing underground and consequently the induced effects on the local amplification of the geomagnetic field. On the other hand, magnetic field amplification is not observed at the *bbr* station, although it is above a conductive region that extends from the upper crust to the upper mantle. This may indicate that the preferential polarization of the geomagnetic field does not align with the geological strike of the conductive structure to amplify the magnetic field at the surface, contrary to what occurs in *bac*.

4.2.1.4 High-voltage power transmission lines of north-northeast Brazil

Electric power transmission lines in Brazil are constantly expanding, so that the current network in the north-northeast region was not operating during the 1990-1991 GDS array. According to information available from ANEEL (2003-2019), some of the substations that currently make up the main 525 kV transmission line in this

region only started operating in 2001. To estimate GICs in this region, we consider a hypothetical situation using a simplified section of the current power transmission line in the Brasilian equatorial region artificially moved as if it were already operating during the 3 magnetic storms recorded by the GDS array. Figure 4.19 shows the simplified version of the grid and the components of the geomagnetic field during the GDS data acquisition period.

Figure 4.19 - Map with straight-line approximations of the current 525 kV power transmission line in north-northeast Brazil. The region covering the Parnaíba basin is shown in pink. The magnetic *dip equator* $I = 0°$ (solid gray line) and boundaries north and south of the ground EEJ effects (dashed gray lines at $I = \pm 6°$) are for the geomagnetic field in 1990-1991.

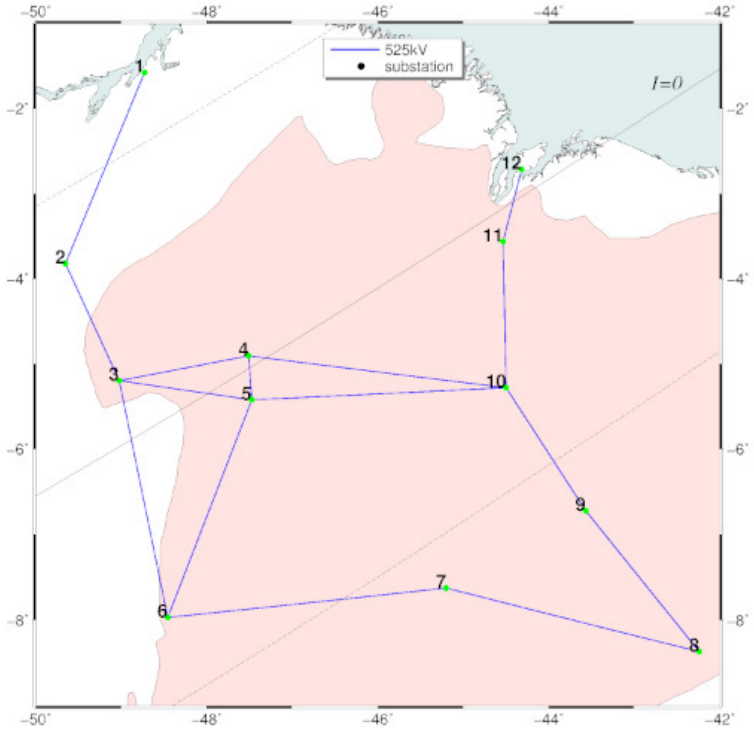

SOURCE: Author production.

The power grid model comes from a 525 kV network operated across almost the entire study region in north-northeast Brazil, including 14 transmission lines and 12 substations. As in the previous study of south-southeast Brazil, existing transmission lines with a lower voltage level are not included in the modeling process.

It is also a simplified electrical network, since the nodes are represented as single conductors, which means that a three-phase power transmission line is connected to a transformer with a neutral point into the ground. Thus, the total resistance is the sum of the transformer resistances and the earthing resistance, even in some substations where the 525 kV network is connected to lower power networks. In Figure 4.19, the substations that make up the 525 kV transmission network section are marked with numbers and their locations specified in Table 4.4.

Table 4.4 - Geographical coordinates of the substations on the simplified 525 kV power transmission line in north-northeast Brazil shown in Figure 4.19.

Nº	**Name**	**Longitude**	**Latitude**
1	Vila do Conde	-48.7	-1.5
2	Tucurui	-49.6	-3.8
3	Maraba	-49.0	-5.1
4	Acailandia	-47.5	-4.9
5	Imperatriz	-47.4	-5.4
6	Colinas	-48.4	-7.9
7	Rib. Gonçalves	-45.2	-7.6
8	S. João Piaui	-42.2	-8.3
9	B. Esperança	-43.5	-6.7
10	P. Dutra	-44.4	-5.2
11	Miranda II	-44.5	-3.5
12	São Luis II	-44.3	-2.7

SOURCE: Author production.

4.2.2 Geoelectric time series during the geomagnetic storms

Geoelectric field was estimated using the previously described convolution procedure between the underground conductivity distribution and the recorded geomagnetic variations. The MT transfer functions (impedance tensor) were initially derived at each GDS site by forward calculation using the software package *ModEM* (EGBERT; KELBERT, 2012; KELBERT et al., 2014). Target frequencies were chosen equally spaced on a logarithmic scale between periods 240 $s - 10,240$ s (corresponding to frequencies between $\sim 9.77\times10^{-5} - \sim 4.17\times10^{-3}$ Hz). These impedance tensor components were then interpolated to have a continuous spectrum using a cubic spline interpolation method with 3^{rd} degree polynomials between contiguous discrete points and ensuring that the first and second derivatives were continuous and smooth (AHLBERG et al., 1967).

To calculate the magnetic field spectrum during the three magnetic storms, five-day data were considered to avoid boundary effects. Thus, 7,201 magnetic field time series with a sampling interval of 1 min were considered at each of the 22 stations for the November (00:00 UT on 25 November to 24:00 UT on 29 November 1990), January (00:00 UT on 22 January to 24:00 UT on 26 January 1991) and February (00:00 UT on 30 January to 24:00 UT on 3 February 1991) storms. A window function was applied to the time series to minimize spectral leakage in the FFT calculation and the magnetic field spectra were estimated at the same bandwidth as the MT impedance tensor. The geoelectric field spectra were then computed by convolving the MT tensors with the magnetic fields using Equation 2.27. The geoelectric field time series were finally derived by inverse FFT and removing the window effect.

The geoelectric field calculated during geomagnetic storms in the region under the influence of EEJ currents is influenced by three factors: the global magnetospheric-ionospheric current system which is affected by magnetospheric compression due to solar wind pressure and particles penetrating through the auroral region, localized ionospheric current systems associated with enhanced Cowling conductivity around the magnetic *dip equator* and effects induced by subsurface conductivity. In the following exercise, it was assumed that the *bra* station (*dip latitude* = 3.11) is far enough from the *dip equator* to have little effect from the increased Cowling conductivity in the equatorial region and is not significantly affected by effects of underground conductivity (Figure 4.13). Thus, we tentatively consider the geomagnetic field measured at this station as representative of the primary storm, without EEJ effect. This field was then taken as a reference for the entire area and the geoelectric field at each station was calculated considering both the locally measured magnetic field and the reference magnetic field of the *bra* station.

Figure 4.20 shows the time series of the geoelectric field estimated in the north-south (E_x) and east-west (E_y) directions during the November 1990 storm using impedance tensor and measured geomagnetic field at each station (upper panels). The intermediate panels show the geoelectric field estimated using the impedance tensor at each site, but with the reference geomagnetic field recorded at station *bra*, as previously discussed. These graphs serve to illustrate the effects of the resistivity structure on the geoelectric field at each station as the EEJ effect is eliminated. Finally, the lower panels show the magnitude of the absolute difference between the geoelectric field under real conditions (upper panels) and the estimated synthetic geoelectric field (middle panels) for both components. This subtraction allows inferring the influence

of the EEJ on the amplitudes of the induced geoelectric field.

Figure 4.20 - Time series of the estimated geoelectric fields E_x (red) and E_y (blue) during the intense storm from November 26 to 28, 1990 (S1) for each station of the P3 profile (upper panels), derived using the 3-D impedance tensors and geomagnetic variations at each station. Intermediate panels show the geoelectric field calculated using the impedance tensor at each station and the geomagnetic variation of the station *bra*. Lower panels show the absolute difference between the modeled geoelectric field (upper panels) and the synthetic geoelectric field (intermediate panels) at each station.

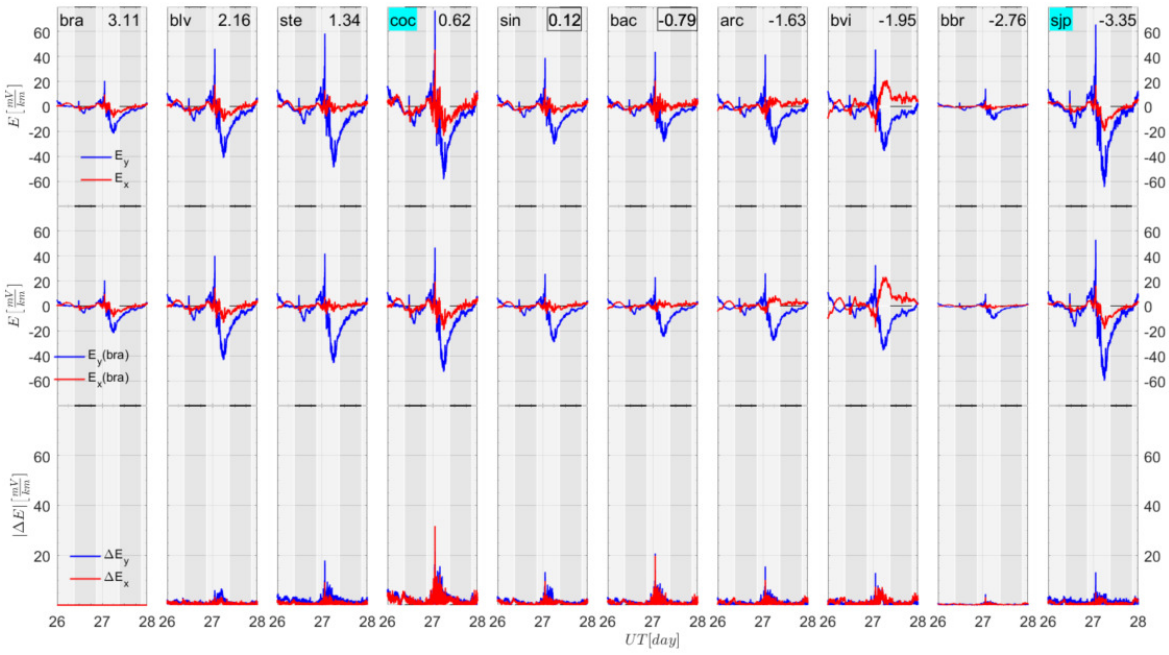

SOURCE: Author production.

In principle, larger geoelectric field amplitudes would be expected for larger dB/dt amplitudes. However, the upper panels of Figure 4.20 show that the highest geoelectric field amplitudes are modeled at the sites *coc* and *sjp*, which differs from the highest dB/dt magnitude observed closer to the site *bac*. This behavior highlights the relevance of the conductivity structure and EEJ effects atenuating or amplifying the geoelectric field. Maximum geoelectric peaks for the intense storm S1 were estimated for these two stations on November 27 at 10:22 LT, with 76.79 mV/km for the E_y component in *coc* and 65.6 mV/km also for the E_y component in *sjp*. On

the other hand, the lowest amplitudes for both E_x and E_y components during this event were modeled in *bbr*, situated over a strong conductive anomaly (Figure 4.13).

The site-to-site variability of the geoelectric field estimated using the reference geomagnetic field shown in intermediate panels clearly expresses the effect of underground conductivity. The largest magnitudes of the geoelectric field are modeled in *coc* and *sjp*, both located over resistive structures in Figure 4.13, while the smallest amplitudes are in *bbr* over a strong conductivity anomaly. Amplifications are also observed in *ste* and *blv*, located in resistive regions in the northern region of the profile. The *sjp* station has the highest amplification by induction effects. Finally, the lower panels showing the influence of the EEJ through the magnitudes $|\Delta E_x|$ and $|\Delta E_y|$ indicate that the largest amplitudes are generally observed in the E_y component, except in *coc*. This confirms that the EEJ current system drives the largest induced geoelectric field amplitudes along the EW direction. It is also observed that the amplifications of the geoelectric field by the EEJ have similar amplitudes at all stations in the region around the dip equator. The main difference is seen in *coc* ($dip\ latitude = 0.62$) which has a much higher amplitude, probably being closer to the EEJ current center during this storm. Also, the E_x field is significant at the two stations around the dip equator (*coc* and *bac*) indicative of perturbations in the N-S direction in the local ionospheric current system during the storm. In summary, the station *coc* shows amplification of the geoelectric field by both the subsurface resistivity structure and the EEJ currents, while *sjp* is amplified only by the resistive structure underlying this station.

Similar analyzes are performed in Figure 4.21 for the weak January 1991 storm. As expected, the modeled geoelectric field is much weaker than in the previous case. The most disturbed periods occur on January 25, with a positive peak at 15:03 UT and the highest geoelectric field amplitudes observed in *coc* (21.7 mV/km in the E_x component and 40 mV/km in E_y) and *sjp* (10.9 mV/km in E_x and 31.1 mV/km in E_y). Another negative peak was calculated at 15:53 LT that same day, with the E_y component giving -40.7 mV/km in *coc* and -37 mV/km in *sjp*. The intermediate panels show the greatest amplification of the geoelectric field due to the strong resistivity anomaly underlying *sjp*, more significant than that observed at stations further north of the *dip equator* (*coc*, *ste* and *blv*). Again the damping of the geoelectric field in *bbr* is highlighted. The lower panels show that the largest EEJ effects were again concentrated in *coc*, but with an important contribution of E_x currents at all stations around the *dip equator*.

Figure 4.21 - Time series of the estimated geoelectric fields E_x (red) and E_y (blue) during the weak storm in 23-25 January 1991 (S2) for each station of the P3 profile (upper panels), derived using the 3-D impedance tensors and geomagnetic variations at each season. Intermediate panels show the geoelectric field calculated using the impedance tensor at each station and the geomagnetic variation of the station *bra*. Lower panels show the absolute difference between the modeled geoelectric field (upper panels) and the synthetic geoelectric field (intermediate panels) at each station.

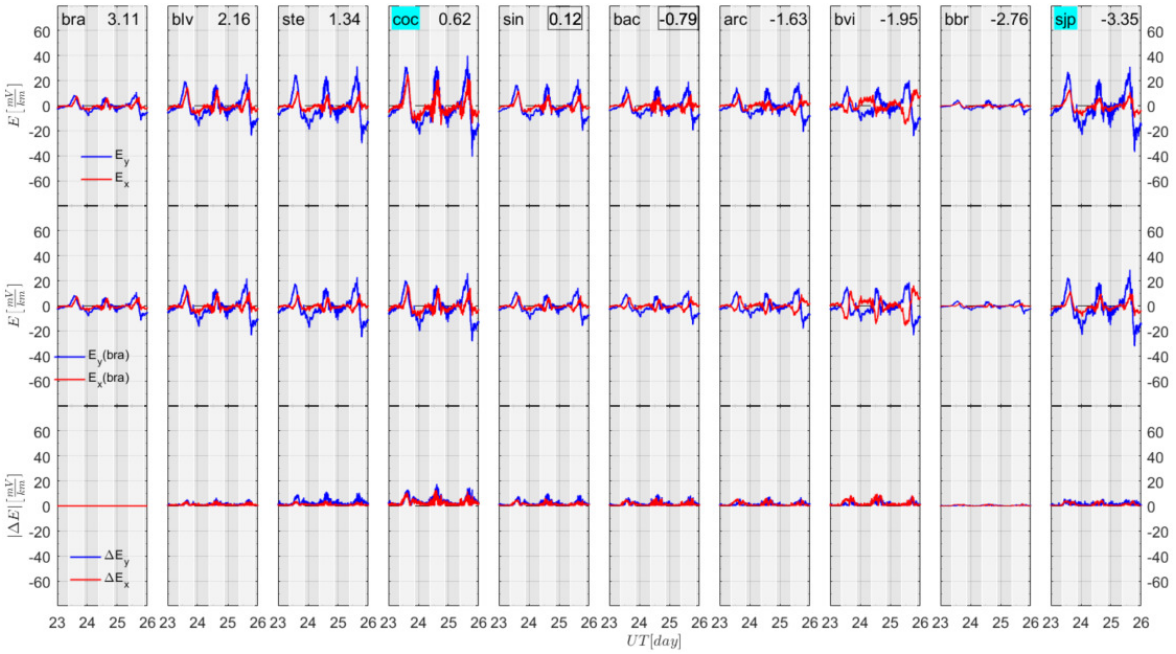

SOURCE: Author production.

Figure 4.22 shows the temporal evolution of the geoelectric field estimated for the stations of the P3 profile during the moderate storm of February 1991 (S3). Despite having a low D_{st} index, this storm appears much more complex in the equatorial region than the others studied here. The largest geoelectric field amplitudes were modeled on February 1st in the E_y component in *coc*, which reached 48.4 mV/km at 15:43 LT and -42.3 mV/km at 18:27 LT (local sunset). The amplitude in *sjp* was also high for this last event with -42.6 mV/km. Intermediate panels show the same results as previous storms, with the highest induction amplification in *sjp*, followed by *coc*, *ste*, and *blv*. The effect of high conductivity under *bbr* is also evident. The lower panels show the complexity of the local ionospheric field during this magnetic

storm. In addition to the amplification of the E_y field (ionospheric currents EW) in the equatorial region, there is also the generation of strong electric fields E_x (ionospheric currents NS) that are concentrated throughout the region around the *dip equator*. This result contradicts an important paradigm for GIC studies in the equatorial region that power lines with EW direction would be the most affected by EEJ currents. In addition to the effects generated by 3-D subsurface conductivity, ionospheric currents during disturbed periods can also induce important variations in the orthogonal component (NS) of the geoelectric field, affecting transmission lines with different directions.

Figure 4.22 - Time series of the estimated geoelectric fields E_x (red) and E_y (blue) during the moderate storm in 31 January-2 February 1991 (S3) for each station of the P3 profile (upper panels), derived using the 3-D impedance tensors and geomagnetic variations at each season. Intermediate panels show the geoelectric field calculated using the impedance tensor at each station and the geomagnetic variation of the station *bra*. Lower panels show the absolute difference between the modeled geoelectric field (upper panels) and the synthetic geoelectric field (intermediate panels) at each station.

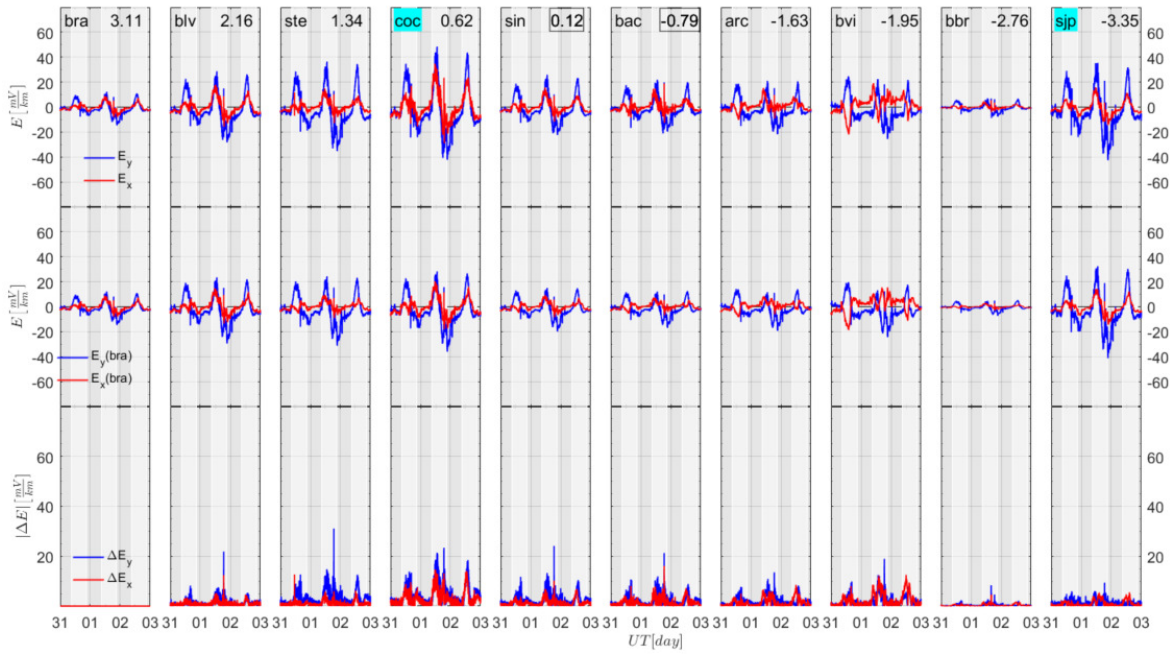

SOURCE: Author production.

As discussed in the previous section on modeling induced currents in transmission lines in south-southeast Brazil, an important aspect in GIC studies is to correlate the main peaks of geoelectric field with the rate of change of the magnetic field and its power spectrum. A comparison of the estimated time series of the geoelectric field during the three storms at *coc* with the time derivative of the magnetic field (dB/dt) at that same station and its Fourier spectral power at selected instants is shown in Figures 4.23-4.25. In the upper and middle panels of each figure, instants are identified in the time series of the geoelectric field and in the time derivatives of the magnetic field (8 vertical dashed lines in each storm) that correspond to chosen peaks in the geoelectric field. At the bottom of the figures are snapshots of dB/dt spectrograms around 10 min of these time instants for all 10 stations of profile P3. The Parseval relationship (SMITH, 2013) was used to calculate how the signal energy is distributed over frequencies. These power spectrum plots are limited to the maximum frequency of 8 mHz which corresponds to the Nyquist frequency for 1 min data acquisition. The upper limit of the power spectrum amplitude was limited to 3 nT/min to facilitate the visualization of the different events, although in some cases the spectrum significantly exceeds this value.

Figure 4.23 shows snapshots of the power spectra of the 8 selected time instants for the November 1990 storm. The selected time instants are presented in Table 4.5. As already noted for the low magnetic latitude region of south-southeast Brazil, the highest signal energies are generally concentrated at lower frequencies and in the dB_x/dt component. The peak with the highest spectral power is number 3 (10:22 LT on 27 November) which presents high power spectrum in both components at frequencies below 2 mHz for stations around the *dip equator*. The maximum power spectra at this time instant were 8.25 nT/min (station *bac*) and 6.87 nT/min (station *arc*) at a frequency of about 1 mHz. Significant energy is also observed at lower frequencies for this time instant in the two components for all stations in the profile.

Figure 4.23 - Comparison of calculated geoelectric field, dB/dt and instantaneous dB/dt power spectra at site *coc* during the November 1990 storm (S1). The upper graphs show estimated geoelectric field time series (E_x and E_y) during the magnetic storm. Intermediate graphs show the corresponding dB_x/dt and dB_y/dt during that time period. At bottom are snapshots of dB_x/dt and dB_y/dt power spectra at the time instants identified by vertical dashed lines in the graphs above for the 10 stations of profile P3.

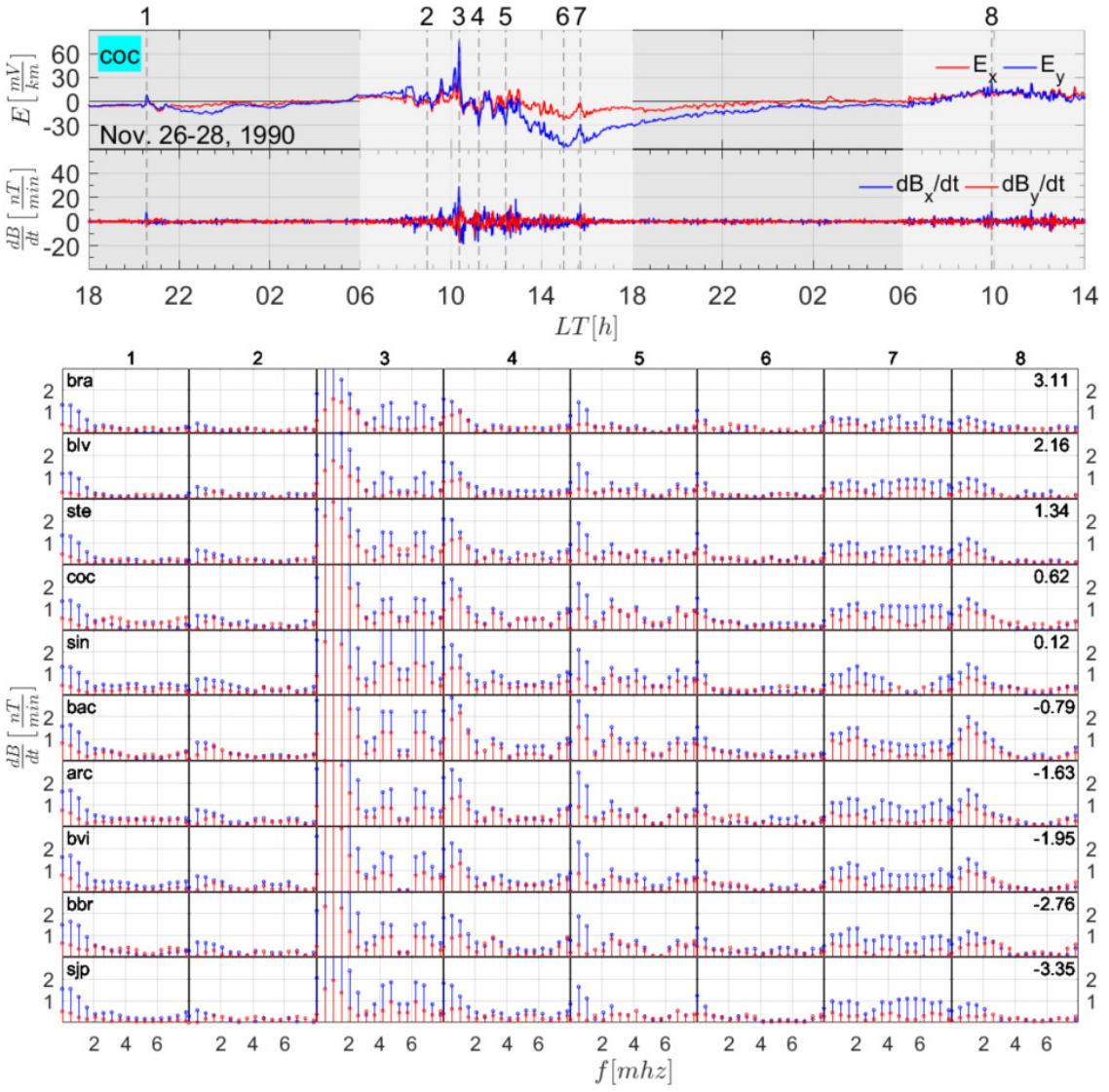

SOURCE: Author production.

Table 4.5 - Time instants of the selected snapshots presented in Figure 4.23.

November 1990		
Snapshot	**Date**	**Time (LT)**
1	26 Nov	20:37
2	27 Nov	09:35
3	27 Nov	10:22
4	27 Nov	11:14
5	27 Nov	12:25
6	27 Nov	14:59
7	27 Nov	15:43
8	28 Nov	09:53

SOURCE: Author production.

Power spectra for the January 1991 weak storm are shown in Figure 4.24 with the chosen time instants presented in Table 4.6. As expected, the power spectra for this storm are very low. The spectrum at time instant 8 (15:53 LT on 25 January) for the station *coc* stands out for being quite different from the other stations in this event. It shows high spectra at virtually all frequencies in both components, with the highest spectral power of 1.93 nT/min at frequency 3.6 mHz.

Figure 4.24 - Comparison of calculated geoelectric field, dB/dt and instantaneous dB/dt power spectra at site *coc* during the January 1991 storm (S2). The upper graphs show estimated geoelectric field time series (E_x and E_y) during the magnetic storm. Intermediate graphs show the corresponding dB_x/dt and dB_y/dt during that time period. At bottom are snapshots of dB_x/dt and dB_y/dt power spectra at the time instants identified by vertical dashed lines in the graphs above for the 10 stations of profile P3.

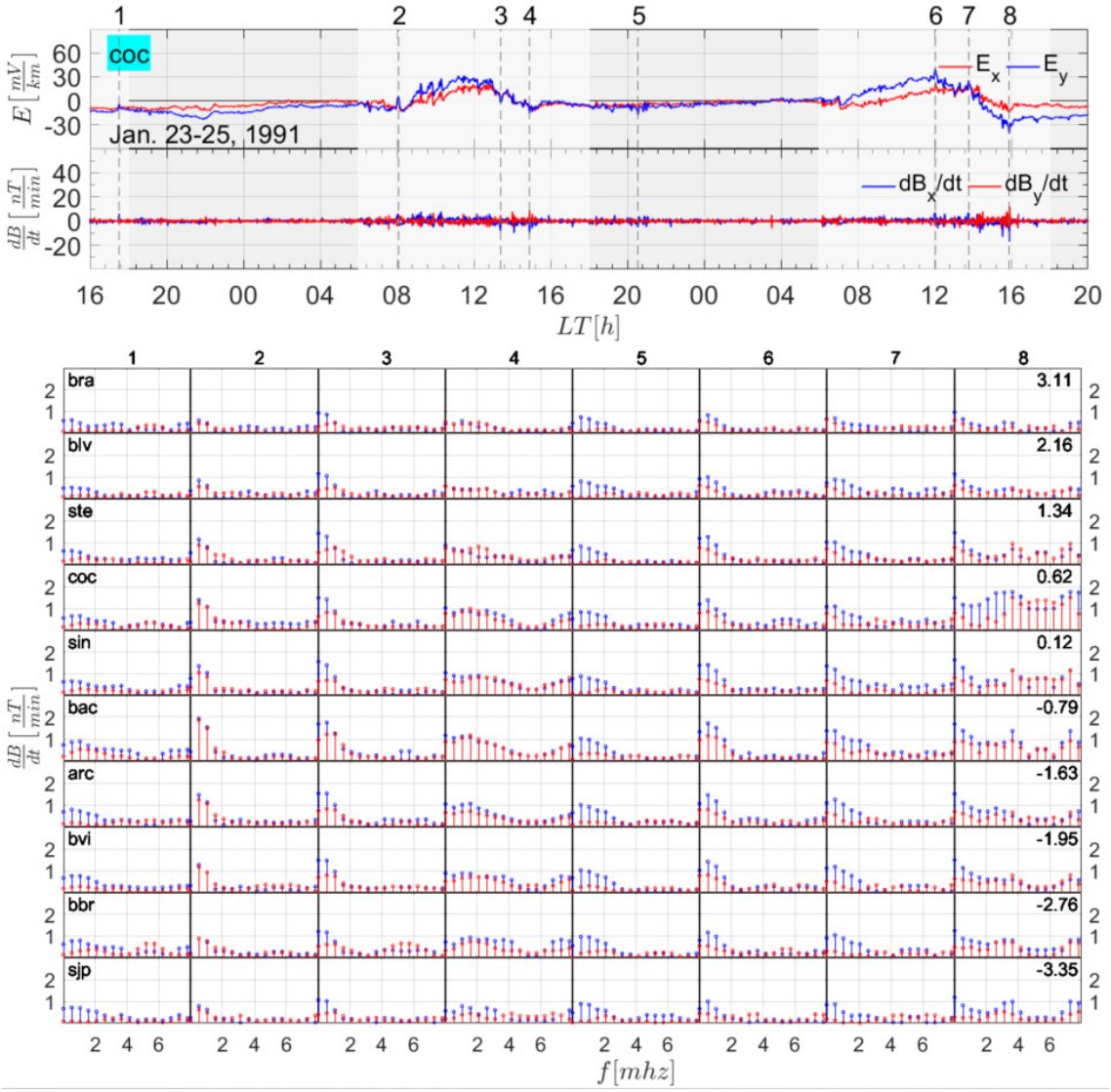

SOURCE: Author production.

Table 4.6 - Time instants of the selected snapshots presented in Figure 4.24.

January 1991		
Snapshot	**Date**	**Time (LT)**
1	23 Jan	17:30
2	24 Jan	08:05
3	24 Jan	13:24
4	24 Jan	14:54
5	24 Jan	20:33
6	25 Jan	12:03
7	25 Jan	13:47
8	25 Jan	15:53

SOURCE: Author production.

The geoelectric field modeled in *coc*, time derivatives of the geomagnetic field and the power spectra for the 8 time instants chosen for the February 1991 moderate storm are presented in Figure 4.25, with the time instants shown in Table 4.6. It has the highest dB/dt peak of the three storms analyzed, in addition to a high spectral content. Time instant 5 (15:42 LT of February 1) shows maximum power spectra of 5.99 nT/min in *bac* and 5.79 nT/min in *arc* for a frequency of about 2 mHz. High energy values distributed over practically the entire spectrum are observed in this event, especially for dB_x/dt. Event 2 (13:04 LT January 31) also has significant spectral content, but limited to frequencies below 2 mHz.

Figure 4.25 - Comparison of calculated geoelectric field, dB/dt and instantaneous dB/dt power spectra at site *coc* during the February 1991 storm (S3). The upper graphs show estimated geoelectric field time series (E_x and E_y) during the magnetic storm. Intermediate graphs show the corresponding dB_x/dt and dB_y/dt during that time period. At bottom are snapshots of dB_x/dt and dB_y/dt power spectra at the time instants identified by vertical dashed lines in the graphs above for the 10 stations of profile P3.

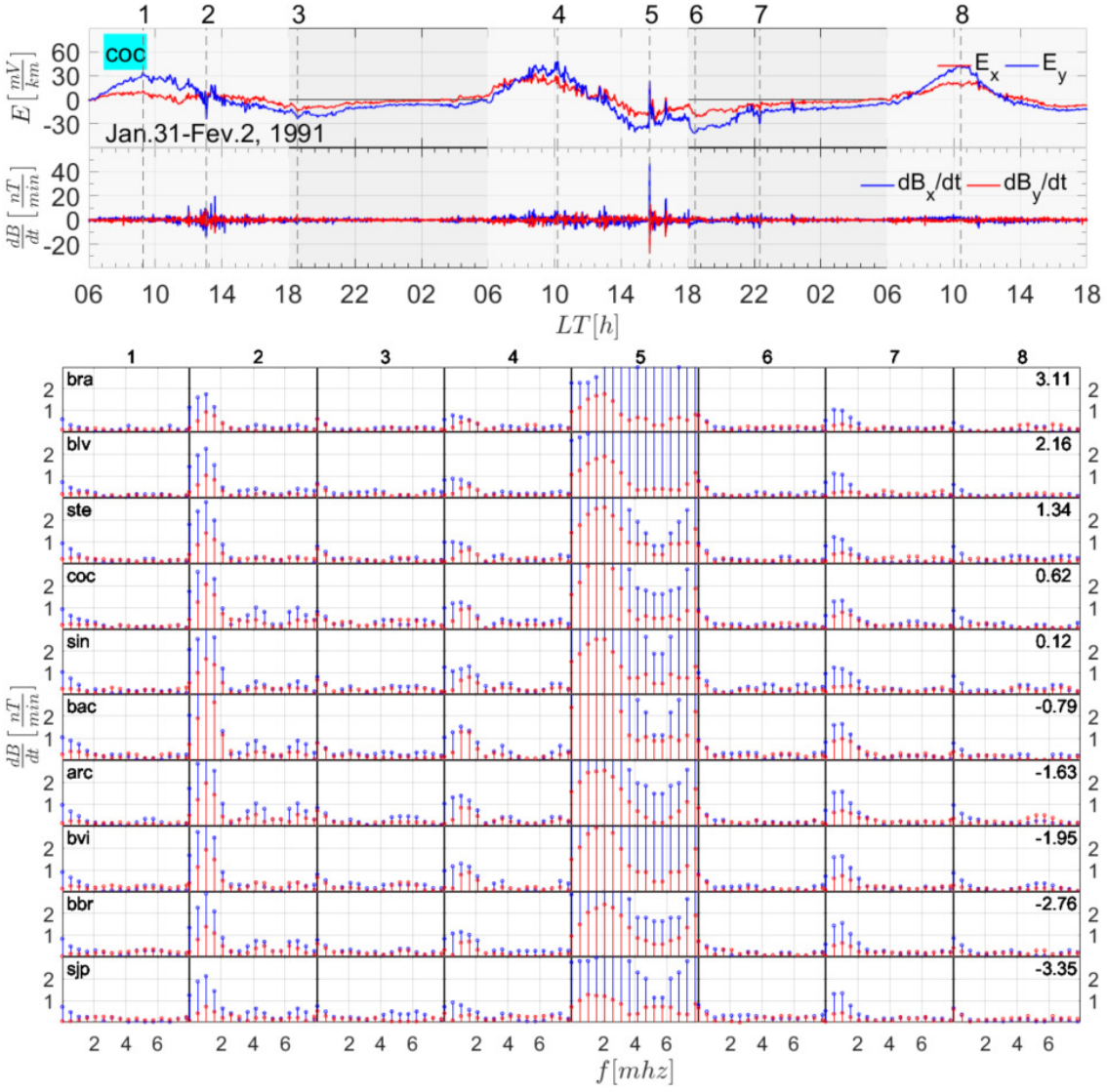

SOURCE: Author production.

Table 4.7 - Time instants of the selected snapshots presented in Figure 4.25.

February 1991		
Snapshot	**Date**	**Time (LT)**
1	31 Jan	09:16
2	31 Jan	13:04
3	31 Jan	18:33
4	01 Feb	10:11
5	01 Feb	15:42
6	01 Feb	18:27
7	01 Feb	22:20
8	01 Feb	10:25

SOURCE: Author production.

Based on these analyzes of the spectral content of the geomagnetic field for the three storms, it can be preliminary inferred which would be the most significant snapshots for GIC modeling. For the November 1990 storm (S1) the highest spectral energies are concentrated in snapshots 3, 4, 5 and 7, for the January 1991 storm (S2) in snapshots 4 and 5, and for the February 1991 storm (S3) in snapshots 2 and 5. However, as discussed in the previous section on GIC modeling in the power network of south-southeast Brazil, it is not only the dB/dt spectral energy and the magnitude of the geoelectric field that are important to assess the effects of these induced currents. The orientation of geoelectric field vectors and their relationship to the orientation of transmission lines also plays an important role. The geoelectric fields obtained in the chosen snapshots of the three geomagnetic storms will be presented in the next section in vector form over all the GDS sites to assess this situation in the study region of Brazilian equatorial zone.

4.2.3 Vector geoelectric fields and GIC estimates

The instantaneous vector geoelectric field and time derivative of the geomagnetic field (dB/dt) is displayed in Figure 4.26 for all selected snapshots of the three storms. In general, the main orientation of geoelectric field vectors is E-W or ENE-WSW, approximately parallel to the magnetic *dip equator*. This preferred direction results from the strong polarity of the geomagnetic field along the magnetic meridian in regions of low magnetic latitudes. Most of the chosen snapshots are diurnal to allow the evaluation of the EEJ effects on the geoelectric field calculations. However, there is no clear evidence of a change in the direction or amplitude of the geoelectric field vectors that could be correlated with the diurnal increase in Cowling conductivity

around the magnetic equator. The orientation of the geoelectric field vectors varies between snapshots due to the variation in the magnetic field during the storm. The geoelectric field vectors are not perfectly parallel in the same snapshot due to underground conductivity effects.

The direction and amplitude of the geoelectric field vectors do not necessarily match the instantaneous dB/dt vector at various time instants of magnetic storms and these variations can be quite significant. This can be seen by comparing snapshots 3 and 5 of the November 1990 storm and snapshots 5 and 6 of the February 1991 storm. Also, in snapshots 5 and 7 of the November 1990 storm, snapshot 6 of the January 1991 storm, and snapshots 6 and 8 of the February storm it is observed that a modest dB/dt amplitude results in a very large magnitude of the geoelectric field vectors in the orthogonal direction. These results again exemplify why dB/dt is not a good GIC proxy when the 3-D impedance tensor is considered, as it disregards the phase relationship between $\boldsymbol{E}$ and $\boldsymbol{B}$ and the dependence on the conductivity structure. Furthermore, the relationship between $\boldsymbol{E}$ and $\boldsymbol{B}$ is a function of frequency given by the complex elements of the impedance tensor, which has a lengthy tail when converted to the time domain which results in lasting impact on the field geoelectric.

Figure 4.26 - Time derivative of the geomagnetic field (dB/dt) and geoelectric field vectors calculated during the selected snapshots for the November 1990 (S1), January 1991 (S2) and February 1991 (S3) storms. Instantaneous geoelectric field (red arrows) and geomagnetic field (green arrows) vectors are shown at each time instant of the snapshots presented in Tables 4.5, 4.6 and 4.7.

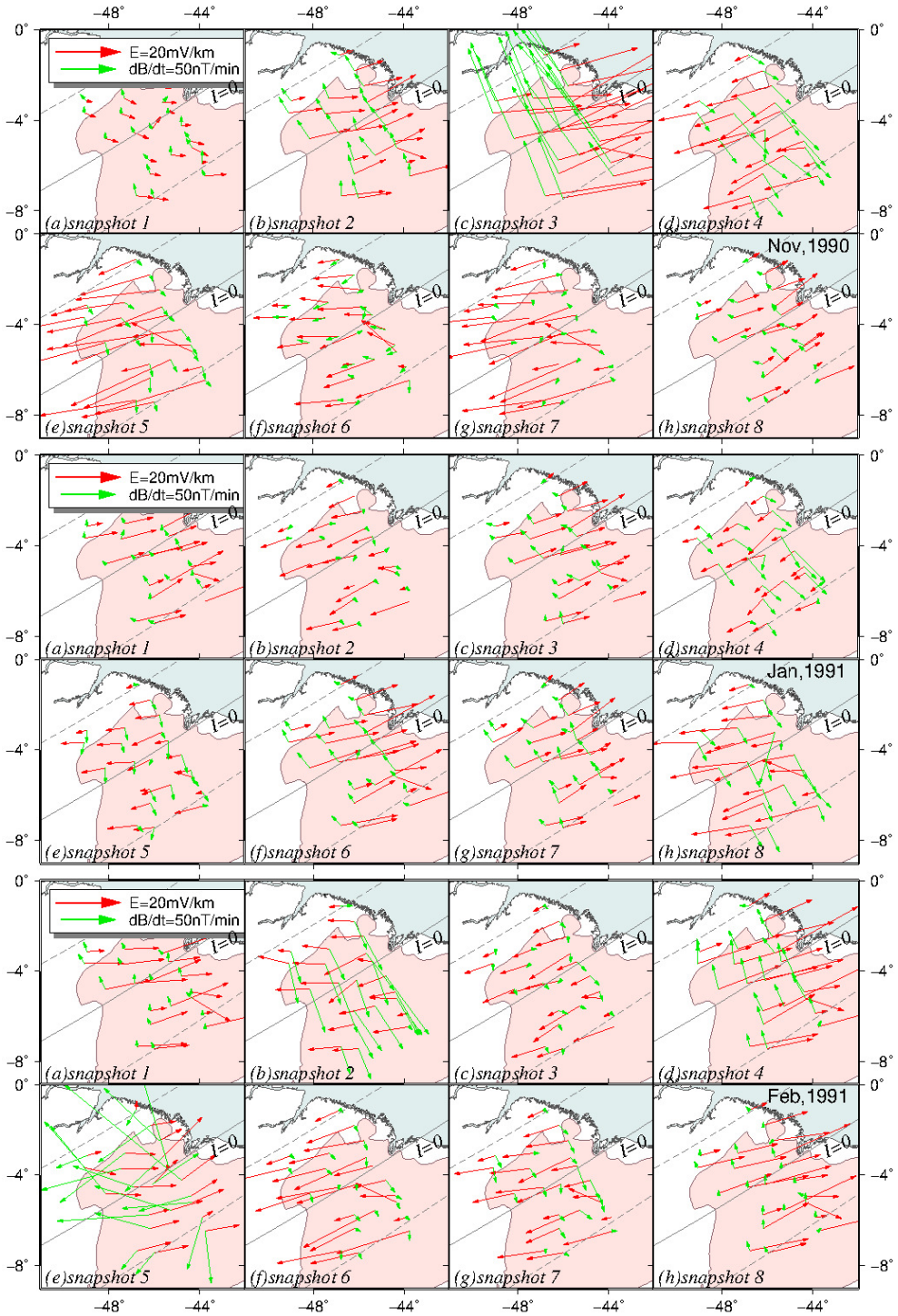

SOURCE: Author production.

Figure 4.27 shows the instantaneous geoelectric field vectors in 4 snapshots plotted on the 3-D resistivity model for the Parnaíba basin for a lower crustal depth ($\sim$ 40 km). Generally, the midwest part of the model is characterized by alternating conductive and resistive structures approximately elongated in the NNW-SSE direction. This situation can be approximated by a 2-D subsurface resistivity model. As a consequence, the geoelectric field vectors suffer little deflection in this region, except for some localized conductivity structure at shallower depths that may slightly alter the vector's direction or decrease its magnitude. On the other hand, the eastern portion of the model (along the profile P3) presents very localized, highly conductive bodies in contact with strongly resistive structures. It is a typical 3-D situation in which the geoelectric field vectors are strongly deflected and their magnitude varies greatly depending on whether the site is located on a resistive or conductive structure. Figure 4.27 also shows the simplified 525 kV power line used to simulate GICs with these geoelectric field vectors. It is observed that the external branches of the power line are located outside the region where the data used to derive the 3-D resistivity model are located. GICs modeled at these extreme nodes are unreliable because there is no adequate subsurface conductivity model for these areas.

Figure 4.27 - Instantaneous vector geoelectric field (black arrows) calculated during four selected snapshots for the November 1990 (S1), January 1991 (S2) and February 1991 (S3) storms plotted on the location of the GDS sites and a horizontal slice of the 3-D resistivity model at $\sim$ 40 km depth (Figure 4.13). Thin black straight-line is an approximation of the 525 kV power transmission line in north-northeast Brazil.

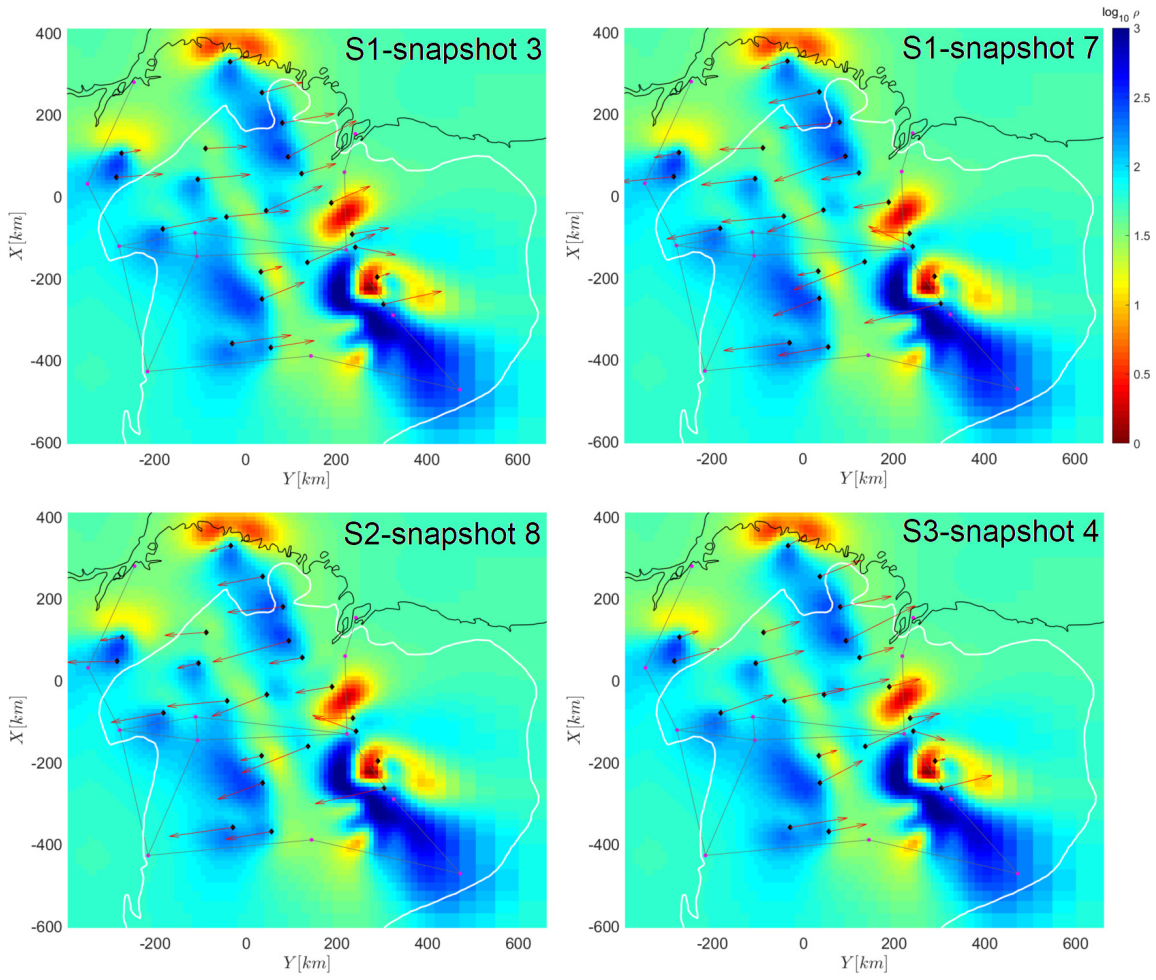

SOURCE: Author production.

To simulate GICs in power transmission lines, the LP method requires obtaining the geoelectric fields along the mesh of the 3-D resistivity model and knowing the engineering parameters and topology of this transmission line. The procedure used with the geoelectric field was the same as in the south-southeast Brazil, using the values obtained in the cells with GDS soundings and filling the empty cells through

which the transmission lines pass with the nearest neighbor interpolation method. The required engineering parameters were also the same as in that study, assuming 0.0174 Ω/km for resistance per unit of length and 0.43 Ω for all grounding resistances.

Figure 4.28 shows instantaneous GIC magnitudes (green circles) on the 12 network nodes of the 525 kV transmission power grid during the eight snapshots in Table 4.3 for the magnetic storm of November 1990. This type of map can be used to identify grid nodes with higher vulnerability to the occurrence of higher amplitude GICs. The vector form of the estimated geoelectric fields (red arrows) during the snapshots are also shown centered at each GDS site location.

Figure 4.28 - Geoelectric field and GIC calculated during the selected snapshots for the November 1990 storm. Red arrows show the instantaneous vector geoelectric field. Green circles are the instantaneous GIC modeled on the 525 kV transmission line substations (in blue). GIC magnitude is proportional to the diameter of the circles, with the highest value at substation 3 for snapshot 3 of this storm corresponding to 6.24 A.

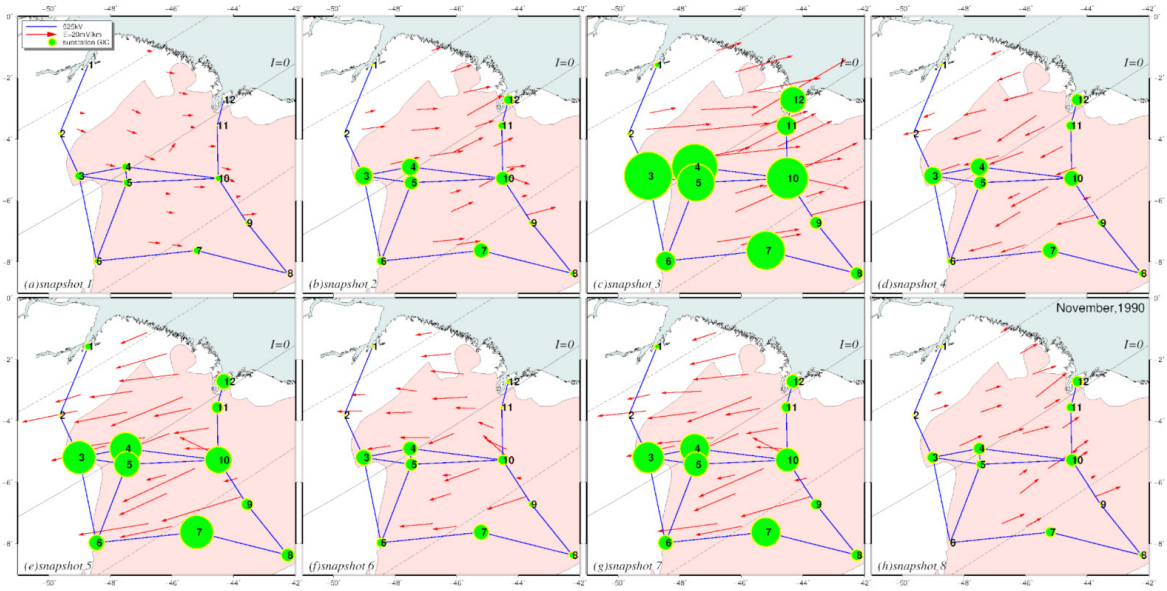

SOURCE: Author production.

The maximum magnitudes of the modeled GICs are observed in snapshots 3, 5 and 7, representative of the main phase of this intense geomagnetic storm. Snapshot 3 has high spectral content at low frequency (Figure 4.23) and the main direction

of the geoelectric field vectors is approximately E-W, coincident with the direction of the transmission lines in the central part of the network. Snapshots 5 and 7 have spectral content spread over various frequencies and very similar geoelectric fields pointing preferentially to ENE-WSW. Snapshot 3 presents the largest GIC amplitude, with emphasis on the substations in the western part of the network (3 and 4). The maximum GIC magnitudes during snapshot 3 were 6.24 A (node 3) and 5.97 A (node 4). In this region, the geoelectric field has a higher amplitude (89.33 mV/km) with vector direction approximately parallel to the transmission line. The GIC minimum magnitudes were modeled at substations 2 and 9, located in regions with enhanced underground conductivity. As the model does not have experimental data to provide information on the conductivity structure covering the entire study area, the quantitative GIC values derived in substations at the grid corners (1, 6 and 8) are unreliable.

Figure 4.29 shows instantaneous geoelectric field vectors (red arrows) and GIC magnitudes (green circles) on the 12 network nodes of the 525 kV transmission power grid during the eight chosen snapshots for the weak magnetic storm of January 1991.

Figure 4.29 - Geoelectric field and GIC calculated during the selected snapshots for the January 1991 disturbed period. Red arrows show the instantaneous vector geoelectric field. Green circles are the instantaneous GIC modeled on the 525 kV transmission line substations (in blue). GIC magnitude is proportional to the diameter of the circles, with the highest value at substation 3 for snapshot 8 corresponding to 3.15 A.

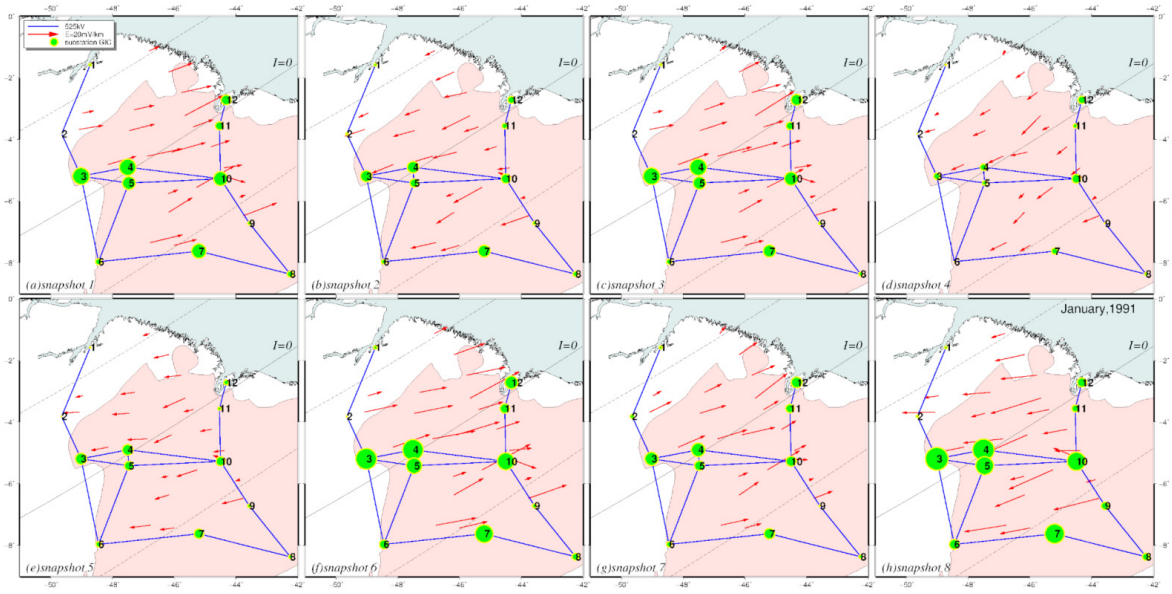

SOURCE: Author production.

Due to the low spectral content of this storm (Figure 4.24), the estimated GIC magnitudes are small for all snapshots. The largest amplitudes were again modeled for nodes 3 (3.15 A) and 4 (2.96 A) during snapshot 8. The geoelectric field of greatest amplitude occurs in this western region of the network with magnitude of 45.48 mV/km and ENE-WSW vector direction near the geomagnetic station *ron*, located on a resistive lithospheric block (Figure 4.13).

Figure 4.30 shows instantaneous geoelectric field vectors (red arrows) and GIC magnitudes (green circles) on the 12 network nodes of the 525 kV transmission power grid during the eight chosen snapshots for the moderate magnetic storm of February 1991.

Figure 4.30 - Geoelectric field and GIC estimated during the selected snapshots for the February 1991 storm. Red arrows show the instantaneous vector geoelectric field. Green circles are the instantaneous GIC modeled on the 525 kV transmission line substations (in blue). GIC magnitude is proportional to the diameter of the circles, with the highest value at substation 4 for snapshot 4 corresponding to 3.20 A.

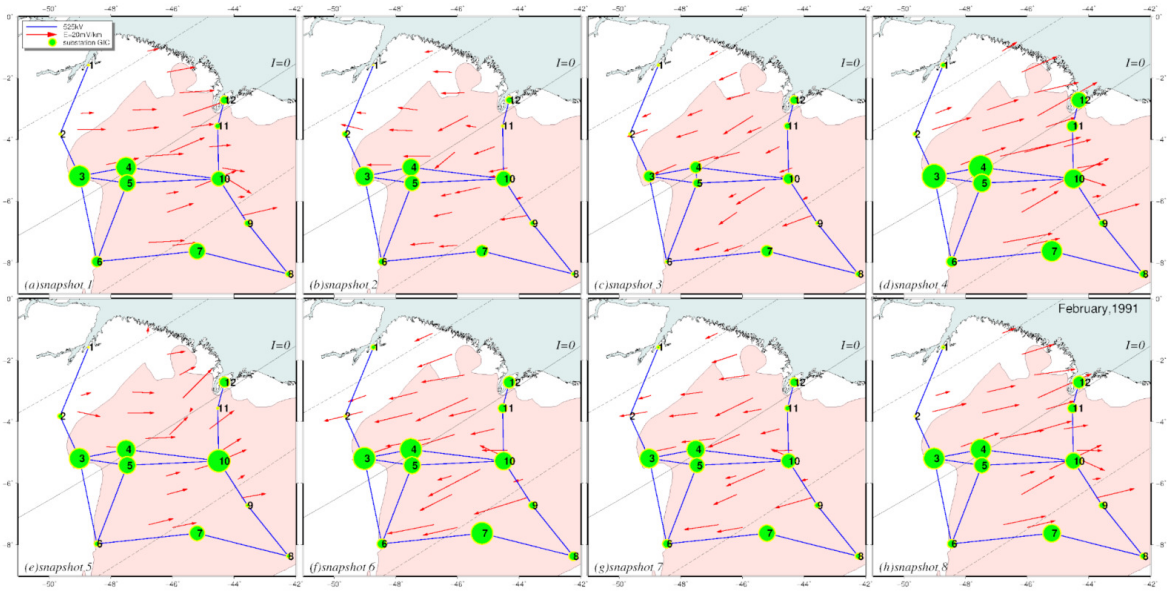

SOURCE: Author production.

Snapshot 5 of this storm recorded at 15:42 LT on February 1, 1991 has the highest dB/dt and high spectral content at different frequencies observed throughout the measurement period in the Brazilian equatorial region. However, the magnitude of the geoelectric field and consequently of the GIC estimated in this time instant is very small. This is related to the behavior of the geoelectric field shown in Figure 4.25. Analogously to previously discussed in GIC modeling for the snapshot 2 of the June 2015 storm in the south-southeast region of Brazil (Subsubsection 4.1.2.3), the inverted polarization between the dB/dt peak and the preceding values of the geoelectric field causes the instantaneous magnitude of the resulting geoelectric field to be low. This is another example from this study in which the dB/dt metric fails because the geoelectric field depends on the previous values of the geomagnetic field.

The estimated GIC magnitudes are low for all snapshots chosen for this storm. The largest amplitudes are concentrated in the central branch of the power grid (nodes

3, 4, 5 and 10), with the largest values of 3.20 A modeled for nodes 3 and 4 during snapshot 4. Again the western region of the model has the largest geoelectric field amplitude with 55.55 mV/km at the geomagnetic station *ron*.

In summary, the largest modeled GIC amplitudes are observed in the central-west portion of the power line (nodes 3, 4 and 5) due to the resistive block underlying this area. Another amplification could occur at node 8 due to another resistive block that could extend to this southeastern end of the grid. However, there is no reliable information in the 3-D resistivity model to support this hypothesis. Node 10 is sandwiched between conductive and resistive structures, but the local geoelectric field appears to be controlled by the resistive structure as significant GICs are modeled for this substation. Thus, the central branch of the electrical network formed by nodes 3, 4, 5 and 10, with E-W direction and parallel to the main direction of the induced geoelectric field, is the most promising to obtain higher GIC estimates. In addition, geoelectric field and GIC estimates for the snapshop 5 of the February 1991 storm confirm that the use of dB/dt as a proxy for GIC activity is inappropriate.

Figures 4.31, 4.32 and 4.33 show the time series of modeled GIC magnitudes for each substation of the simplified electrical grid during the magnetic storms of November 1990, January 1991 and February 1991, respectively. Two effects are observed in these figures: substations with higher GIC amplitudes and substations with GIC of opposite polarity. Generally, the higher amplitude GICs are concentrated in the central branch of the line (nodes 3, 4, 5 and 10) which, as discussed earlier, are located on resistive blocks and benefit from the direction of the lines having direction parallel to the predominantly E-W oriented geoelectric fields. Substations with GIC polarity opposite to the other substations are concentrated in a NE-SW branch at the north end of the grid (node 1) and in a NW-SE branch at the south end of the grid (node 9), both with very low amplitudes GICs. As previously discussed in Subsection 4.1.3, reverse polarity is likely associated with edge effects where current flows into or out of the ground through substations at the extremes of the network (BOTELER; PIRJOLA, 2017).

Figure 4.31 - Time series of the resulting GIC modeling at the 12 substations of the simplified 525 kV transmission line during the November 1990 storm. Substations with the highest GIC magnitudes are highlighted in yellow.

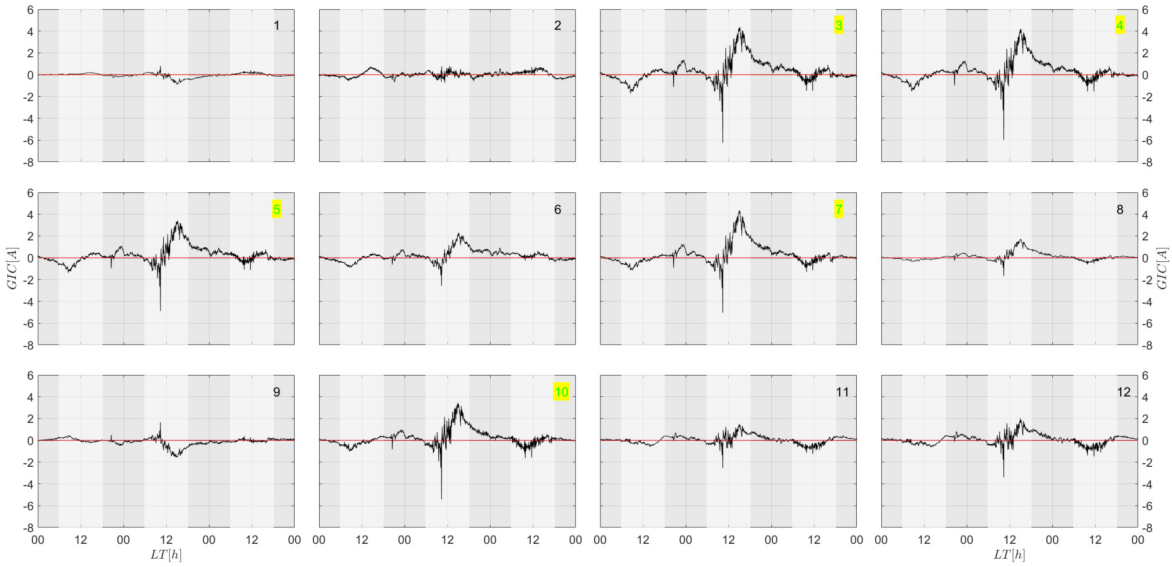

SOURCE: Author production.

Figure 4.32 - Time series of the resulting GIC modeling at the 12 substations of the simplified 525 kV transmission line during the January 1991 storm. Substations with the highest GIC magnitudes are highlighted in yellow.

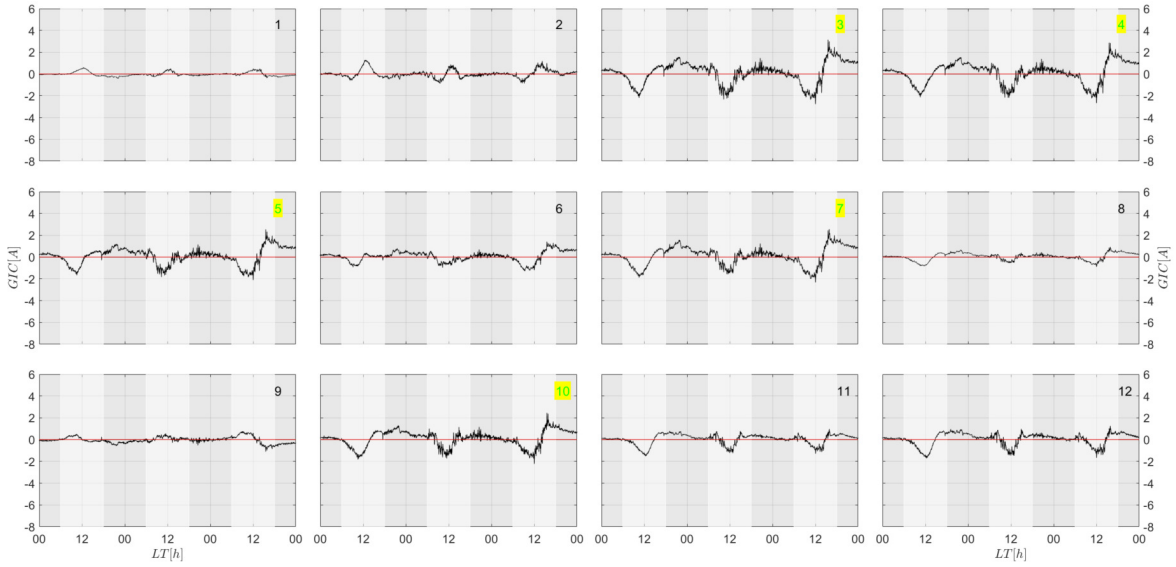

SOURCE: Author production.

Figure 4.33 - Time series of the resulting GIC modeling at the 12 substations of the simplified 525 kV transmission line during the February 1991 storm. Substations with the highest GIC magnitudes are highlighted in yellow.

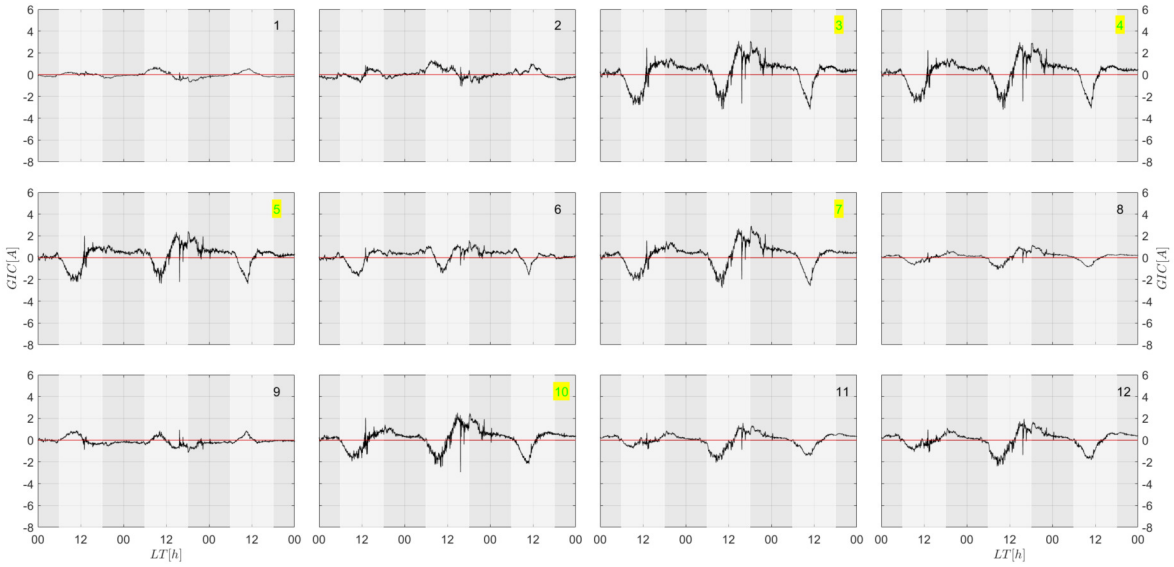

SOURCE: Author production.

The GIC calculations in this section were used to test the methodology developed in a period when the studied region was under the effect of EEJ ionospheric currents. The results indicate that the EEJ effects on the estimated induced currents for the modeled storms (weak to intense intensity) are small when compared to the effects of the 3-D variation of the subsurface conductivity. However, it is not possible to predict the local ionospheric effect on the geoelectric field for stronger storms. The magnitudes of the modeled GICs are small (maximum 6.24 A for the intense November 1990 storm), but are of little significance considering the severe limitations of the modeling. In addition to the limitations also valid for the south-southeast region of Brazil (lack of information on the engineering parameters of the transmission lines), it can be added the use of geomagnetic variations with low acquisition cadence (1 min) and the limitations of the available 3-D resistivity model that does not cover the total area of the power grid chosen for modeling.

5 DISCUSSIONS

The study presented in this thesis is the first approach to model GIC amplitudes in Brazil using the current state-of-the-art to simulate induced currents affecting power transmission lines during magnetic storms. For the first time, 3-D electrical resistivity models for the Earth's interior and geomagnetic variations acquired with high-cadence rate (1 s) were used to simulate geoelectric currents in simplified representations of real electrical networks in the south-southeast and north-northeast regions of the country. These regions were chosen both by availability of GDS/MT data for deriving 3-D resistivity models and to assess possible distortional effects of the South Atlantic Magnetic Anomaly and the equatorial electrojet. The quantitative GIC values derived for the two regions are not significant due to inherent simplifications assumed in the modeling approach. In any case, an accurate and detailed calculation of GIC time series in our electrical networks was not the main goal of this study. A guide to the relative importance of system parameters when estimating GIC impacts on an electrical grid is provided by Zheng et al. (2014). In our case, in addition to the lack of information about the network engineering parameters and the omission of transmission lines of lower voltage elements, the limitation of the 3-D model used to calculate the geoelectric field and the practical impossibility of using data with high acquisition cadence must also be considered.

Although the geomagnetic field measured for the south-southeast region has a resolution of 10 s and the impedance tensor elements derived from foward calculation can cover any frequency range, the modeled geoelectric field has a lower resolution. This is because the 3-D resistivity model was mainly based on GDS data acquired with a sampling of 60 s (Nyquist limit of 120 s). As a result, only periods longer than this Nyquist limit can be considered for calculating the geoelectric field. At depths shallower than a critical depth determined by the subsurface resistivity structure and the highest frequency data available, there is essentially no structural resolving power and electromagnetic induction methods become insensitive to structural details while remaining sensitive to conductance (vertically integrated conductivity) of these surface layers. Thus, the resolution of the near-surface part of the model is very low, especially outside the limits of the two sedimentary basins studied (Paraná and Parnaíba) where resistive structures outcropping at the edges of these basins are observed. In this scenario, the modeled geoelectric values should be considered lower estimates of potential real values.

An additional problem arises due to the 3-D resistivity model used to derive GICs

in the Parnaíba basin region. It is based on data covering an area smaller than that needed to model the chosen power network. This brings limitations not only in the calculation of induced currents entering the substations located in these regions without data coverage, but also affects the modeling of the substations in the most central part of the model and connected to these outermost substations. The LP model uses a line integral that requires knowledge of the entire terrestrial connection with adjacent substations.

In addition to the aforementioned limitations for the geoelectric field calculation, the method chosen to interpolate this field for GIC modeling also has significant limitations. The interpolation technique adopted deals with an irregular grid (50-100 km) of cells with observed data, which makes the geoelectric field to be considered homogeneous between some substations. This procedure eliminates local galvanic distortions associated with fine-scale inhomogeneities in the near-surface conductivity structure, but makes lateral variations in conductance very approximate. The use of local transfer functions or regional spatial averaging to represent conductivity for geoelectric field modeling is widely discussed in the literature (BEDROSIAN; LOVE, 2015; BONNER; SCHULTZ, 2017; KELBERT et al., 2019). Alternative methods that do not require a realistic geoelectric field and its integration over power lines for calculating GICs (KELBERT; LUCAS, 2020) can also be considered to streamline the entire modeling procedure for its future operational use by the EMBRACE program. The validation efforts planned for comparing modeled GICs with real measurements on sensors installed in some substations can help answer these questions.

The modeling results of this thesis are based on a limited number of magnetic storms. For the south-southeast region, the two largest storms recorded since the beginning of the EMBRACE magnetometer network were analyzed, while for the north-northeast region only the storms recorded during the short period of operation of the magnetometers of the GDS matrix were available. Magnetic storms are known to vary significantly between different occurrences, so any storm is essentially unique (KAMIDE; MALTSEV, 2007). A small change in the ionospheric source during a disturbance of the geomagnetic field can potentially produce large changes in both the magnitude and orientation of the resulting geoelectric fields at the Earth's surface. From a risk assessment perspective, what matters is the availability of a dataset that includes a significant number of severe space weather events. This is because the substations that experience large GICs in a network are not necessarily the same during different (BLAKE et al., 2016) magnetic storms. More statistics are needed to reliably assess the hot spots and potential risks of GIC in our power grids,

considering large timescales. This can be done for the south-southeast region, but not in the equatorial region under the influence of the equatorial electrojet. Due to the continuous westward drift of the main geomagnetic field, the geophysical conditions available during that GDS survey will no longer be repeated in the Brazilian equatorial region. Therefore, it will not be practicable to assess possible EEJ effects during more severe storms.

Geomagnetic data from stations installed at great distances in the south-central region of Brazil show that the geomagnetic field can be geographically uniform during magnetic storms (Figures 4.2 and 4.5). This is not unexpected for low magnetic latitudes, but also needs to be confirmed with a larger number of events. Field homogeneity can be used to increase computational speed for operational GIC risk assessment in the EMBRACE program. A sophisticated and computationally demanding technique such as SECS may not be necessary for magnetic field interpolation in this region of low magnetic latitude during magnetically disturbed periods. Simpler techniques such as the nearest neighbor used here for GIC modeling or latitudinal weighted averaging using distant EMBRACE magnetometers may be adequate enough for magnetic field interpolations. Another possibility is to use a reduced number of stations as a reference for the geomagnetic field of the entire region, streamlining the methodology to provide real-time responses of the geoelectric field for EMBRACE operational purposes. Also, confirmed that the geomagnetic field is homogeneous during storms in this region of low magnetic latitudes, the same procedure can be adopted for the north-northeast region of Brazil. One (or some) of the EMBRACE stations currently operating in the region east of the magnetic equator (shown in Figure 4.14) can be used as a reference for the geomagnetic field in that region. Geoelectric fields could then be modeled using the 3-D resistivity model of the Parnaíba basin and this regional geomagnetic field during storms of the current solar cycle. This possibility was not explored in this thesis because one of the goals was to evaluate the EEJ influence on GIC estimates.

One of the most critical aspects of modeling GICs in electrical networks is the need to validate the estimated results. This procedure was carried out in this thesis by sequentially validating the different computer programs developed. However, the final estimate of the GIC magnitude cannot be verified and this is the most error-prone step due to the multiple simplifications employed in the modeling. This validation process can only be done by comparing the results generated by the model with the currents actually measured in the neutral of transformers of the network substations. On the other hand, the simulation results of this study can be used to

determine GIC mitigation strategies for power transmission systems in Brazil and, even more importantly at this point, to identify relevant substations for installation of monitoring equipment. In the case of the 525 kV line of south-southeast Brazil, mitigation efforts can be initially focused on the identified cluster of hot spots in substation 2, located on the northern edge of the study area, and on the central parts of the modeled network, where small conductances and E-W lines can generate large geoelectric fields and GIC. Sensors can then be installed in some of these substations, avoiding those with multiple connections. The main candidates would be nodes 2, 8, 11, 13 or 15 (Figure 4.10). An extreme member with a lower current could also be chosen for validation processes and the NE-SW line at the north end would be the obvious choice. The major limitations in modeling the north-northeast Brazilian region make the definition of these mitigation strategies more complex. In principle, the central east-west part of the power grid, involving nodes 3, 4, 5 and 10, could be the best option.

6 CONCLUSIONS AND FUTURE WORKS

A current methodology for GIC simulation in power transmission lines during magnetic storms was implemented in this thesis. This methodology was used to model currents generated during storms recorded in the south-southeast and north-northeast regions of Brazil in simplified representations of real electrical networks. For this purpose, measurements of geomagnetic variations of 1 s available for the south-southeast region, under the influence of the South Atlantic Magnetic Anomaly, and of 60 s available from an old GDS survey in the north-northeast region, at that time under influence of the equatorial electrojet, were used. As a result, possible substations more prone to GICs of greater magnitude were identified in these simplified networks. Due to the various simplifications assumed in the modeling approach, an accurate calculation of the GIC is not possible. The study primarily focuses on identifying substations with potential GIC hazards and where to install future monitoring equipment for validation efforts.

Future work will focus on operational Space Weather activities targeting regional forecasts for future assimilation by the EMBRACE program. The next step will be to use the results of this thesis to plan the installation of GIC sensors in the chosen substations in the south-southeast region of Brazil. More information is also required to improve GIC calculations. As discussed earlier, the electrical resistivity structure was obtained primarily by fitting long period GDS data. The impedance tensors for geoelectric field modeling were derived from the 3-D resistivity model. This model will need to be updated to improve the resolution of the upper crust, which can only be done with future MT surveys. It is also necessary to include low voltage transmission lines in the electrical network model and to use realistic information about transformer resistances and substation grounding. This means intensifying end-user participation in the modeling and validation processes, especially power transmission line operators. Finally, the methodology developed for this region should be expanded to other regions of Brazil where similar GDS arrays (BOLOGNA et al., 2014) and MT soundings so far generally concentrated along profiles are available. In the absence of detailed continental-scale MT grids (such as USArray, SinoProbe and AusLamp), is what can be done at this point.

REFERENCES

ABDU, M. A.; BATISTA, I. S.; CARRASCO, A. J.; BRUM, C. G. M. South Atlantic magnetic anomaly ionization: a review and a new focus on electrodynamic effects in the equatorial ionosphere. **Journal of Atmospheric and Solar Terrestrial Physics**, v. 67, p. 1643–1657, 2005. Available from: <http://dx.doi.org/10.1016/j.jastp.2005.01.014>. 13

AHLBERG, J. H.; NILSON, E. N.; WALSH, J. L. **The theory of splines and their applications**. [S.l.]: Elsevier Science, 1967. (ISSN). ISBN 9780080955452. 40, 88

ALKEN, P.; THEBAULT, E.; BEGGAN, C. D.; AMIT, H.; AUBERT, J.; BAERENZUNG, J.; BONDAR, T. N.; BROWN, W. J.; CALIF, S.; CHAMBODUT, A.; CHULLIAT, A.; COX, G. A.; FINLAY, C. C.; FOURNIER, A.; GILLET, N.; GRAYVER, A.; HAMMER, M. D.; HOLSCHNEIDER, M.; HUDER, L.; HULOT, G.; JAGER, T.; KLOSS, C.; KORTE, M.; KUANG, W.; KUVSHINOV, A.; LANGLAIS, B.; LEGER, J.; LESUR, V.; LIVERMORE, P. W.; LOWES, F. J.; MACMILLAN, S.; MAGNES, W.; MANDEA, M.; MARSAL, S.; MATZKA, J.; METMAN, M. C.; MINAMI, T.; MORSCHHAUSER, A.; MOUND, J. E.; NAIR, M.; NAKANO, S.; OLSEN, N.; PAVON-CARRASCO, F. J.; PETROV, V. G.; ROPP, G.; ROTHER, M.; SABAKA, T. J.; SANCHEZ, S.; SATURNINO, D.; SCHNEPF, N. R.; SHEN, X.; STOLLE, C.; TANGBORN, A.; TOFNER-CLAUSEN, L.; TOH, H.; TORTA, J. M.; VARNER, J.; VERVELIDOU, F.; VIGNERON, P.; WARDINSKI, I.; WICHT, J.; WOODS, A.; YANG, Y.; ZEREN, Z.; ZHOU, B. International geomagnetic reference field: the thirteenth generation. **Earth, Planets and Space**, v. 73, n. 49, 2021. Available from: <http://dx.doi.org/10.1186/s40623-020-01288-x>. 50

ALMEIDA, F. F. M.; BRITO NEVES, B. B.; CARNEIRO, C. D. R. The origin and evolution of the South American platform. **Earth-Science Reviews**, v. 50, n. 1, p. 77–111, 2000. ISSN 0012-8252. Available from: <http://dx.doi.org/10.1016/S0012-8252(99)00072-0>. 48

ALMEIDA, F. F. M.; HASUI, Y.; BRITO NEVES, B. B.; FUCK, R. A. Brazilian structural provinces: an introduction. **Earth-Science Reviews**, v. 17, p. 1–29, 1981. Available from: <http://dx.doi.org/10.1016/0012-8252(81)90003-9>. 71

ALVES, L.; PADILHA, A. Correntes geomagneticamente induzidas. **Boletim SBGf**, n. 98, p. 21–23, 2017. Available from: <https://www.researchgate.net/publication/314205093_Correntes_Geomagneticamente_Induzidas>. 3

AMM, O. Ionospheric elementary current systems in spherical coordinates and their application. **Journal of Geomagnetism and Geoelectricity**, v. 49, p. 947–955, 1997. Available from: <http://dx.doi.org/10.5636/jgg.49.947>. 26, 27

AMM, O.; VILJANEN, A. Ionospheric disturbance magnetic field continuation from the ground to the ionosphere using spherical elementary current systems. **Earth, Planets and Space**, v. 51, p. 431–440, 1999. Available from: <http://dx.doi.org/10.1186/BF03352247>. 26, 27

ANEEL. **Características e requisitos técnicos básicos das instalações de linhas de transmissão.** Brasil, 2003–2019. Agência Nacional de Energia Elétrica (ANEL). Available from: <https://antigo.aneel.gov.br/transmissao4>. 66, 86

ARORA, B. R.; SUBBA RAO, P. B. V.; TRIVEDI, N. B.; PADILHA, A. L.; VITORELLO, I. Appraisal of electromagnetic induction effects on magnetic pulsation studies. **Annales Geophysicae**, v. 19, n. 2, p. 171–178, 2001. Available from: <http://dx.doi.org/10.5194/angeo-19-171-2001>. 86

ARORA, B. R.; TRIVEDI, N. B.; VITORELLO, I.; PADILHA, A. L.; RIGOTI, A.; CHAMALAUN, F. H. Overview of Geomagnetic Deep Soundings (GDS) as applied in the Parnaiba basin, north-northeast Brazil. **Revista Brasileira de Geofísica**, v. 17, n. 1, p. 43–65, 1999. ISSN 0102-261X. Available from: <https://doi.org/10.1590/S0102-261X1999000100005>. 33, 39, 72, 75, 76

ASSUMPÇÃO, M.; BIANCHI, M.; JULIÀ, J.; DIAS, F. L.; FRANÇA, G. S.; NASCIMENTO, R.; DROUET, S.; PAVÃO, C. G.; ALBUQUERQUE, D. F.; LOPES, A. E. V. Crustal thickness map of Brazil: data compilation and main features. **Journal of South American Earth Sciences**, v. 43, p. 74–85, 2013. ISSN 0895-9811. Available from: <https://doi.org/10.1016/j.jsames.2012.12.009>. 74

BAKER, W. G.; MARTYN, D. F. Electric currents in the ionosphere - the conductivity. **Philosophical Transactions of the Royal Society of London, Series A, Mathematical and Physical Sciences**, v. 246, p. 281—294, 1953. Available from: <http://dx.doi.org/10.1098/rsta.1953.0016>. 12

BARBOSA, C.; HARTMANN, G.; PINHEIRO, K. Numerical modeling of geomagnetically induced currents in a Brazilian transmission line. **Advances in Space Research**, v. 55, n. 4, p. 1168–1179, 2015. ISSN 18791948. Available from: <http://dx.doi.org/10.1016/j.asr.2014.11.008>. 2, 3

BEDROSIAN, P. A.; LOVE, J. J. Mapping geoelectric fields during magnetic storms: synthetic analysis of empirical United States impedances. **Geophysical Research Letters**, v. 42, n. 23, p. 10160–10170, 2015. ISSN 19448007. Available from: <http://dx.doi.org/10.1002/2015GL066636>. 2, 51, 114

BERNHARDI, E. H.; CILLIERS, P. J.; GAUNT, C. T. Improvement in the modelling of geomagnetically induced currents in southern Africa. **South African Journal of Science**, v. 104, n. 7-8, p. 265–272, 2008. ISSN 0038-2353. Available from: <http://www.scielo.org.za/scielo.php?script=sci_arttext&pid=S0038-23532008000400010&nrm=iso>. 27, 29, 55

BIZZI, L. A.; SCHOBBENHAUS, C.; GONÇALVES, J. H.; BAARS, F. J.; DELGADO, I. M.; ABRAM, M. B.; NETO, R. L.; MATOS, G. M. M. de; SANTOS, J. O. S. **Geologia, tectônica e recursos minerais do Brasil: Sistema de Informações Geográficas-SIG e mapas na Escala 1: 2 500 000**. 4. ed. [S.l.]: Companhia de Pesquisa e Recursos Minerais, 2001. Cd-Rom. xvi, xviii, 49, 73

BLAKE, S. P.; GALLAGHER, P. T.; CAMPANYA, J.; HOGG, C.; BEGGAN, C. D.; THOMSON, A. W. P.; RICHARDSON, G. S.; BELL, D. A detailed model of the Irish high voltage power network for simulating GICs. **Space Weather**, v. 16, n. 11, p. 1770–1783, 2018. Available from: <http://dx.doi.org/10.1029/2018SW001926>. 54

BLAKE, S. P.; GALLAGHER, P. T.; MCCAULEY, J.; JONES, A. G.; HOGG, C.; CAMPANYA, J.; BEGGAN, C.; THOMSON, A. W. P.; KELLY, G. S.; BELL, D. Geomagnetically induced currents in the Irish power network during geomagnetic storms. **Space Weather**, v. 14, p. 1136–1154, 2016. Available from: <http://dx.doi.org/10.1002/2016SW001534>. 114

BOLOGNA, M. S.; PADILHA, A. L.; PADUA, M. B.; VITORELLO, I.; CHAMALAUN, F. H. Paraguay-Araguaia belt conductivity anomaly: a fundamental tectonic boundary in South American Platform imaged by electromagnetic induction surveys. **Geochemistry, Geophysics, Geosystems**, v. 15, n. 3, p. 509–515, 2014. Available from: <http://dx.doi.org/10.1002/2013GC004970>. 117

BONNER, L. R.; SCHULTZ, A. Rapid prediction of electric fields associated with geomagnetically induced currents in the presence of three-dimensional ground structure: projection of remote magnetic observatory data through magnetotelluric impedance tensors. **Space Weather**, v. 15, n. 1, 2017. ISSN 15427390. Available from: <http://dx.doi.org/10.1002/2016SW001535>. 2, 114

BOTELER, D. H. The evolution of Québec earth models used to model geomagnetically induced currents. **IEEE Transactions on Power Delivery**, v. 30, n. 5, p. 2171–2178, 2015. Available from: <http://dx.doi.org/10.1109/TPWRD.2014.2379260>. 2

BOTELER, D. H.; PIRJOLA, R. J. Modeling geomagnetically induced currents. **Space Weather**, v. 15, n. 1, p. 258–276, 2017. ISSN 15427390. Available from: <http://dx.doi.org/10.1002/2016SW001499>. 1, 7, 8, 68, 109

CAGNIARD, L. Basic theory of the magneto-telluric method of geophysical prospecting. **Geophysics**, v. 18, p. 605–635, 1953. Available from: <http://dx.doi.org/10.1190/1.1437915>. 16

CARABALLO, R.; BETTUCCI, L. S.; TANCREDI, G. Geomagnetically induced currents in the Uruguayan high-voltage power grid. **Geophysical Journal International**, v. 195, n. 2, p. 844–853, 2013. Available from: <http://dx.doi.org/10.1093/gji/ggt293>. 1, 2, 55

CARTER, B.; YIZENGAW, E.; PRADIPTA, R.; WEYGAND, J.; PIERSANTI, M.; PULKKINEN, A.; MOLDWIN, M.; NORMAN, R.; ZHANG, K. Geomagnetically induced currents around the world during the 17 March 2015 storm. **Journal of Geophysical Research: Space Physics**, v. 121, n. 10, p. 496–507, 2016. ISSN 21699402. Available from: <http://dx.doi.org/10.1002/2016JA023344>. 70

CARTER, B. A.; YIZENGAW, E.; PRADIPTA, R.; HALFORD, A. J.; NORMAN, R.; ZHANG, K. Interplanetary shocks and the resulting geomagnetically induced currents at the equator. **Geophysical Research Letters**, v. 42, n. 16, p. 6554–6559, 2015. Available from: <https://doi.org/10.1002/2015GL065060>. 70

CASTRO, D. L. de; FUCK, R. A.; PHILLIPS, J. D.; VIDOTTI, R. M.; BEZERRA, F. H.; DANTAS, E. L. Crustal structure beneath the paleozoic parnaíba basin revealed by airborne gravity and magnetic data, brazil.

Tectonophysics, v. 614, p. 128–145, 2014. ISSN 0040-1951. Available from: <https://doi.org/10.1016/j.tecto.2013.12.009>. 71

CHAMALAUN, F. H.; WALKER, R. A microprocessor based digital fluxgate magnetometer for geomagnetic deep sounding studies. **Journal of Geomagnetism and Geoelectricity**, v. 34, n. 8, p. 491–507, 1982. Available from: <http://dx.doi.org/10.5636/jgg.34.491>. 78

CHAPMAN, S. Bakerian Lecture.—Some phenomena of the upper atmosphere. **Proceedings of the Physical Society of London, Section B**, v. 64, p. 833–844, 1951. Available from: <http://dx.doi.org/10.1098/rspa.1931.0105>. 12

CORDANI, U. G.; BRITO NEVES, B. B.; FUCK, R. A.; PORTO, R.; TOMAZ FILHO, A.; CUNHA, F. M. B. **Estudo preliminar de integração do Pré-Cambriano com os eventos tectônicos das bacias sedimentares brasileiras**. Rio de Janeiro, Brasil: Petrobrás, 1984. Petrobrás/CENPES/SINTEP report, 15. 72

CUNHA, F. M. B. **Evolução paleozóica da Bacia do Parnaíba e seu arcabouço tectônico**. 107 p. Dissertação (Mestrado em Geologia) — Universidade Federal do Rio de Janeiro, Rio de Janeiro, 1986. 72

CUTTLER, S. W.; LOVE, J. J.; SWIDINSKY, A. Geoelectric hazard assessment: the differences of geoelectric responses during magnetic storms within common physiographic zones. **Earth, Planets and Space**, v. 70, n. 35, 2018. ISSN 18805981. Available from: <http://dx.doi.org/10.1186/s40623-018-0807-7>. 2, 51

DALY, M. C.; ANDRADE, V.; BAROUSSE, C. A.; COSTA, R.; MCDOWELL, K.; PIGGOTT, N.; POOLE, A. J. Brasiliano crustal structure and the tectonic setting of the Parnaíba basin of NE Brazil: results of a deep seismic reflection profile. **Tectonics**, v. 33, n. 11, p. 2102–2120, 2014. Available from: <http://dx.doi.org/10.1002/2014TC003632>. 71

DALY, M. C.; FUCK, R. A.; JULIÀ, J.; MACDONALD, D.; WATTS, A. B. Cratonic basin formation: a case study of the Parnaíba Basin of Brazil. **Geological Society, London, Special Publications**, v. 472, p. 1–15, 2018. ISSN 0305-8719. Available from: <http://dx.doi.org/10.1144/SP472>. 73

DENARDINI, C. M.; ABDU, M. A.; DE PAULA, E. R.; SOBRAL, J. H.; WRASSE, C. M. Seasonal characterization of the equatorial electrojet height rise

over Brazil as observed by the RESCO 50MHz back-scatter radar. **Journal of Atmospheric and Solar-Terrestrial Physics**, v. 67, n. 17-18 SPEC. ISS., p. 1665–1673, 2005. ISSN 13646826. Available from: <http://dx.doi.org/10.1016/j.jastp.2005.04.008>. 13

DENARDINI, C. M.; CHEN, S. S.; RESENDE, L. C. A.; MORO, J.; BILIBIO, A. V.; FAGUNDES, P. R.; GENDE, M. A.; CABRERA, M. A.; BOLZAN, M. J. A.; PADILHA, A. L.; SCHUCH, N. J.; HORMAECHEA, J. L.; ALVES, L. R.; NETO, P. F. B.; NOGUEIRA, P. A. B.; PICANÇO, G. A. S.; BERTOLLOTTO, T. O. The Embrace magnetometer network for South America: network description and its qualification. **Radio Science**, v. 53, n. 3, p. 288–302, 2018. Available from: <http://dx.doi.org/10.1002/2017RS006477>. 47, 51

DIMMOCK, A. P.; ROSENQVIST, L.; WELLING, D. T.; VILJANEN, A.; HONKONEN, I.; BOYNTON, R. J.; YORDANOVA, E. On the regional variability of dB/dt and its significance to GIC. **Space Weather**, v. 18, n. 8, 2020. Available from: <http://dx.doi.org/10.1029/2020SW002497>. 63

DIOGO, E. M. **Modelagem de correntes geomagneticamente induzidas: comparação de efeitos em diferentes latitudes**. Tese (Doutorado em Geofísica Espacial) — Instituto Nacional de Pesquisas Espaciais, São José dos Campos, Brazil, 2018. Available from: <http://www.inpe.br/posgraduacao/ges/arquivos/teses/tese_erica_diogo_2018.pdf>. 2, 55

DONG, S. W.; LI, T. D.; Lü, Q. T.; GAO, R.; YANG, J. S.; CHEN, X. H. Progress in deep lithospheric exploration of the continental China: a review of the SinoProbe. **Tectonophysics**, v. 606, p. 1—13, 2013. Available from: <https://doi.org/10.1016/j.tecto.2013.05.038>. 2

EGBERT, G.; KELBERT, A.; MEQBEL, N. **ModEM: user's guide: revision 1.0**. Corvallis, Oregon, USA, 2016. 1–27 p. 32

EGBERT, G. D. Robust multiple-station magnetotelluric data processing. **Geophysical Journal International**, v. 130, n. 2, p. 475–496, 1997. ISSN 0956540X. Available from: <https://doi.org/10.1111/j.1365-246X.1997.tb05663.x>. 33

EGBERT, G. D.; KELBERT, A. Computational recipes for electromagnetic inverse problems. **Geophysical Journal International**, v. 189, p. 251—-267, 2012. Available from: <https://doi.org/10.1111/j.1365-246X.2011.05347.x>. 2, 22, 23, 32, 88

ESPINOSA, K. V.; PADILHA, A. L.; ALVES, L. R. Effects of ionospheric conductivity and ground conductance on geomagnetically induced currents during geomagnetic storms: case studies at low-latitude and equatorial regions. **Space Weather**, v. 17, n. 2, p. 252–268, 2019. ISSN 15427390. Available from: <https://doi.org/10.1029/2018SW002094>. 2, 3, 45, 66

ESPINOSA, K. V.; PADILHA, A. L.; ALVES, L. R.; SCHULTZ, A.; KELBERT, A. Estimating geomagnetically induced currents in the southern Brazil power network using 3-D Earth resistivity model. **Space Weather**, (submitted), 2022. 5, 47

EVANS, R. L. Conductivity of Earth materials. In: CHAVE, A. D.; JONES, A. G. (Ed.). **The magnetotelluric method: theory and practice**. New York: Cambridge University Press, 2012. chapter 6, p. 50–95. 18

EXEC.ORDER. **Coordinating national resilience to electromagnetic pulses**. Presidential document, March 2019. 12041-12046 p. Available from: <https://www.federalregister.gov/documents/2019/03/29/2019-06325/coordinating-national-resilience-to-electromagnetic-pulses>. 2

FONTES, S. L.; BENEVIDES, A.; PANETTO, L.; MAURYA, V. P.; LA TERRA, E. F.; PADILHA, A. Deep images of electrical conductivity in Parnaiba Basin - NE Brazil. In: EGU GENERAL ASSEMBLY, 2022. **Proceedings...** Vienna: EGU, 2022, 2022. Available from: <https://doi.org/10.5194/egusphere-egu22-6586>. 33

FORBES, J. M. The equatorial electrojet. **Reviews of Geophysics**, v. 19, n. 3, p. 469–504, 1981. Available from: <https://doi.org/10.1029/RG019i003p00469>. 12, 86

FUJII, I.; OOKAWA, T.; NAGAMACHI, S.; OWADA, T. The characteristics of geoelectric fields at kakioka, kanoya, and memambetsu inferred from voltage measurements during 2000 to 2011. **Earth, Planets and Space**, v. 67, n. 62, 2015. Available from: <http://dx.doi.org/10.1186/s40623-015-0241-z>. 41

GANNON, J. L.; BIRCHFIELD, A. B.; SHETYE, K. S.; OVERBYE, T. J. A comparison of peak electric fields and GICs in the Pacific Northwest using 1-D and 3-D conductivity. **Space Weather**, v. 15, n. 11, p. 1535—1547, 2017. Available from: <https://doi.org/10.1002/2017SW001677>. 3

GANUSHKINA, N. Y.; LIEMOHN, M. W.; DUBYAGIN, S. Current systems in the Earth's magnetosphere. **Reviews of Geophysics**, v. 56, n. 2, p. 309–332,

2018. ISSN 19449208. Available from: <https://doi.org/10.1002/2017RG000590>. 9

GAUNT, C. T.; COETZEE, G. Transformer failures in regions incorrectly considered to have low GIC-risk. In: IEEE (Ed.). **2007 IEEE lausanne power tech**. Lausanne, Switzerland: IEEE, 2007. p. 807–812. Available from: <https://doi.org/10.1109/PCT.2007.4538419>. 3

GONZALEZ, W. D.; JOSELYN, J. A.; KAMIDE, Y.; KROEHL, H. W.; ROSTOKER, G.; TSURUTANI, B. T.; VASYLIUNAS, V. M. What is a geomagnetic storm? **Journal of Geophysical Research**, v. 99, n. A4, p. 5771–5792, 1994. Available from: <https://doi.org/10.1029/93JA02867>. 9, 11

GRAWE, M. A.; MAKELA, J. J.; BUTALA, M. D.; KAMALABADI, F. The impact of magnetic field temporal sampling on modeled surface electric fields. **Space Weather**, v. 16, n. 11, p. 1721—1739, 2018. Available from: <https://doi.org/10.1029/2018SW001896>. 3

GÓES, A. M. O.; SOUZA, J. M. P.; TEIXEIRA, L. B. Estágio exploratório e perspectivas petrolíferas da Bacia do Parnaíba. **Boletim de Geociencias da Petrobras**, v. 4, p. 55–64, 1990. 72

HESSE, D. An investigation of the equatorial electrojet by means of ground-based magnetic measurements in Brazil. **Annales de Geophysique**, v. 38, p. 315–320, sep 1982. Available from: <https://ui.adsabs.harvard.edu/abs/1982AnG....38..315H>. 13

HEYNS, M. J.; LOTZ, S. I.; GAUNT, C. T. Geomagnetic pulsations driving geomagnetically induced currents. **Space Weather**, v. 19, n. 2, p. e02557, 2021. Available from: <https://doi.org/10.1029/2020SW002557>. 66

IEEE. **Grounding of industrial and commercial power systems**. IEEE Std 142. New York: Institute of Electrical and Electronics Engineers, 2007. ISBN ISBN 0-7381-5640-X SS95700. 66

INGHAM, M.; RODGER, C. J.; DIVETT, T.; DALZELL, M.; PETERSEN, T. Assessment of GIC based on transfer function analysis: GIC risk. **Space Weather**, v. 15, p. 1615–1627, 2017. Available from: <http://dx.doi.org/10.1002/2017SW001707>. 2

JIRACEK, G. R. Near surface and topographic distortions in electromagnetic induction. **Surveys in Geophysics**, v. 11, n. 2-3, p. 163–203, 1990. Available from: <http://dx.doi.org/10.1007/BF01901659>. 17

JOSELYN, J. A.; TSURUTANI, B. T. Geomagnetic sudden impulses and storm sudden commencements: a note on terminology. **Eos, Transactions American Geophysical Union**, v. 71, n. 47, p. 1808–1809, 1990. Available from: <https://doi.org/10.1029/90EO00350>. 10

JUUSOLA, L.; AMM, O.; VILJANEN, A. One-dimensional spherical elementary current systems and their use for determining ionospheric currents from satellite measurements. **Earth, Planets and Space**, v. 58, p. 667–678, 2006. Available from: <http://dx.doi.org/10.1186/BF03351964>. 29

KAMIDE, Y.; MALTSEV, Y. Geomagnetic Storms. In: KAMIDE, Y.; CHIAN, A. (Ed.). **Handbook of the solar-terrestrial environment**. Berlin, Heidelberg: Springer, 2007. p. 355–374. Available from: <https://doi.org/10.1007/978-3-540-46315-3_14>. 114

KANE, R. P.; TRIVEDI, N. B. Comparison of equatorial electrojet characteristics at Huancayo and Eusébio (Fortaleza) in the South American region. **Journal of Atmospheric and Terrestrial Physics**, v. 44, n. 9, p. 785–792, 1982. ISSN 00219169. Available from: <https://doi.org/10.1016/0021-9169(82)90007-1>. 13, 86

KASRAN, F. A. M.; JUSOH, M. H.; RAHIM, S. A. E. A.; ABDULLAH, N. Geomagnetically Induced Currents (GICs) in equatorial region. In: INTERNATIONAL CONFERENCE ON SYSTEM ENGINEERING AND TECHNOLOGY , 8, 2018. **Proceedings...** Bandung, Indonesia: IEEE, 2018. Available from: <https://doi.org/10.1109/ICSEngT.2018.8606391>. 11, 70

KELBERT, A. The role of global/regional earth conductivity models in natural geomagnetic hazard mitigation. **Surveys in Geophysics**, v. 41, n. 1, p. 115–166, 2020. Available from: <http://dx.doi.org/10.1007/s10712-019-09579-z>. 3, 66

KELBERT, A.; BALCH, C.; PULKKINEN, A.; EGBERT, G.; J., L.; RIGLER, E. J.; FUJII, I. Methodology for time-domain estimation of storm time geoelectric fields using the 3-D magnetotelluric response tensors. **Space Weather**, v. 15, n. 7, p. 874–894, 2017. ISSN 15427390. Available from: <https://doi.org/10.1002/2017SW001594>. xvi, 30, 40, 41, 42, 43

KELBERT, A.; BEDROSIAN, P. A.; MURPHY, B. S. The first 3-D conductivity model of the contiguous United States: reflections on geologic structure and application to induction hazards. In: _____. **Geomagnetically induced currents from the sun to the power grid**. Washington, DC, USA: American Geophysical Union, 2019. (Geophysical Monograph Series), p. 127–151. Available from: <https://doi.org/10.1002/9781119434412.ch8>. 114

KELBERT, A.; EGBERT, G.; SCHULTZ, A. **IRIS DMC Data Services Products: EMTF, the magnetotelluric transfer functions**. [S.l.], 2011. Available from: <https://doi.org/10.17611/DP/EMTF.1>. 2, 39

KELBERT, A.; LUCAS, G. M. Modified GIC estimation using 3-D Earth conductivity. **Space Weather**, v. 18, n. 8, 2020. Available from: <https://doi.org/10.1029/2020SW002467>. 2, 114

KELBERT, A.; MEQBEL, N.; EGBERT, G. D.; TANDON, K. ModEM: a modular system for inversion of electromagnetic geophysical data. **Computers and Geosciences**, v. 66, p. 40–53, 2014. ISSN 0098-3004. Available from: <https://doi.org/10.1016/j.cageo.2014.01.010>. 22, 23, 32, 88

KELLY, G. S.; VILJANEN, A.; BEGGAN, C. D.; THOMSON, A. W. P. Understanding GIC in the UK and French high-voltage transmission systems during severe magnetic storms. **Space Weather**, v. 15, n. 1, p. 99–114, 2017. Available from: <http://dx.doi.org/10.1002/2016SW001469>. 1

KIKUCHI, T.; ARAKI, T. Horizontal transmission of the polar electric field to the equator. **Journal of Atmospheric and Terrestrial Physics**, v. 41, n. 9, p. 927–936, 1979. ISSN 00219169. Available from: <https://doi.org/10.1016/0021-9169(79)90094-1>. 13

KIKUCHI, T.; HASHIMOTO, K. K. Transmission of the electric fields to the low latitude ionosphere in the magnetosphere-ionosphere current circuit. **Geoscience Letters**, v. 3, n. 1, 2016. ISSN 21964092. Available from: <https://doi.org/10.1186/s40562-016-0035-6>. 11

KIRKHAM, H.; MAKAROV, Y.; DAGLE, J.; DESTEESE, J.; ELIZONDO, M.; DIAO, R. **Geomagnetic storms and long-term impacts on power systems**. Richland WA, December 2011. Pacific Northwest National Laboratory (PNNL). Available from: <http://www.pnnl.gov/main/publications/external/technical_reports/PNNL-21033.pdf>. 8

LEHTINEN, M.; PIRJOLA, R. Currents produced in earth conductor networks by geomacnetically-induced electric fields. **Annales Geophysicae**, v. 3, p. 479–484, 1985. 44

LOVE, J. J.; LUCAS, G. M.; KELBERT, A.; BEDROSIAN, P. A. Geoelectric hazard maps for the Pacific Northwest. **Space Weather**, v. 16, p. 1114–1127, 2018b. Available from: <https://doi.org/10.1029/2018SW001844>. 3, 40, 41

LOVE, J. J.; RIGLER, E. J.; KELBERT, A.; FINN, C. A.; BEDROSIAN, P. A.; BALCH, C. C. **On the feasibility of real-time mapping of the geoelectric field across North America**. Reston, Virginia, 2018a. 16 p. U.S. Geological Survey. Available from: <https://doi.org/10.3133/ofr20181043>. 2, 31

LUCAS, G. M.; LOVE, J. J.; KELBERT, A. Calculation of voltages in electric power transmission lines during historic geomagnetic storms: an investigation using realistic earth impedances. **Space Weather**, v. 16, n. 2, p. 185–195, 2018. ISSN 15427390. Available from: <https://doi.org/10.1002/2017SW001779>. 2, 40, 41

MACKIE, R. L.; RODI, W.; WATTS, M. D. 3-D magnetotelluric inversion for resource exploration. In: SEG ANNUAL MEETING, 2001. **Proceedings...** [S.l.]: San Antonio, Texas: SEG, 2001. 2

MANTOVANI, M. S. M.; QUINTAS, M. C. L.; SHUKOWSKY, W.; BRITO NEVES, B. B. Delimitation of the paranapanema Proterozoic block: a geophysical contribution. **Episodes**, v. 28, n. 1, p. 18–22, 2005. Available from: <https://doi.org/10.18814/epiiugs/2005/v28i1/002>. 48

MARSHALL, R. A.; DALZELL, M.; WATERS, C. L.; GOLDTHORPE, P.; SMITH, E. A. Geomagnetically induced currents in the New Zealand power network. **Space Weather**, v. 10, p. S08003, 2012. Available from: <http://dx.doi.org/10.1029/2012SW000806>. 1, 3

MAURYA, V. P.; MEJU, M. A.; FONTES, S. L.; PADILHA, A. L.; TERRA, E. F. L.; MIQUELUTTI, L. G. Deep resistivity structure of basalt-covered central part of Paraná Basin, Brazil, from joint 3-D MT and GDS data imaging. **Geochemistry, Geophysics, Geosystems**, v. 19, p. 1994–2013, 2018. Available from: <http://dx.doi.org/10.1029/2017GC007314>. 48

MCLAY, S. A.; BEGGAN, C. D. Interpolation of externally-caused magnetic fields over large sparse arrays using Spherical Elementary Current Systems. **Annales Geophysicae**, v. 28, p. 1795–1805, 2010. Available from: <https://doi.org/10.5194/angeo-28-1795-2010>. 55

MCPHERRON, R. L. Magnetic pulsations: Their sources and relation to solar wind and geomagnetic activity. **Surveys in Geophysics**, v. 26, p. 545–592, 2005. ISSN 01693298. Available from: <http://doi.org/10.1007/s10712-005-1758-7>. 10, 11

MEJU, M. A.; FONTES, S. L.; OLIVEIRA, M. F. B.; LIMA, J. P. R.; ULUGERGERLI, E. U.; CARRASQUILLA, A. A. Regional aquifer mapping using combined VES-TEM-AMT/EMAP methods in the semi-arid eastern margin of Parnaiba Basin, Brazil. **Geophysics**, v. 64, p. 337–356, 1999. Available from: <http://dx.doi.org/10.1190/1.1444539>. 72

MELFI, A. J.; PICCIRILLO, E. M.; NARDY, A. J. R. Geological and magmatic aspects of the Paraná Basin – an introduction. In: PICCIRILLO, E. M.; MELFI, A. J. (Ed.). **The mesozoic flood volcanism of the Paraná Basin**. São Paulo, SP, Brazil: IAG-USP, 1988. p. 1–13. 48

MEQBEL, N. M.; EGBERT, G. D.; WANNAMAKER, P. E.; KELBERT, A.; SCHULTZ, A. Deep electrical resistivity structure of the northwestern U.S. derived from 3-D inversion of USArray magnetotelluric data. **Earth and Planetary Science Letters**, v. 402, p. 290–304, 2014. ISSN 0012821X. Available from: <https://doi.org/10.1016/j.epsl.2013.12.026>. 74

MILAN, S. E.; CLAUSEN, L. B.; COXON, J. C.; CARTER, J. A.; WALACH, M. T.; LAUNDAL, K.; ØSTGAARD, N.; TENFJORD, P.; REISTAD, J.; SNEKVIK, K.; KORTH, H.; ANDERSON, B. J. Overview of solar wind–magnetosphere–ionosphere–atmosphere coupling and the generation of magnetospheric currents. **Space Science Reviews**, v. 206, n. 1-4, p. 547–573, 2017. ISSN 15729672. Available from: <https://doi.org/10.1007/s11214-017-0333-0>. 9

MILANI, E. J.; RAMOS, V. A. Orogenias paleozóicas no domínio sul-ocidental do Gondwana e os ciclos de subsidência da Bacia do Paraná. **Revista Brasileira de Geociências**, v. 28, n. 4, p. 473–484, 1998. 48

NAKAMURA, S.; EBIHARA, Y.; FUJITA, S.; GOTO, T.; YAMADA, N.; WATARI, S.; OMURA, Y. Time domain simulation of Geomagnetically Induced Current (GIC) flowing in 500-kV power grid in Japan including a three-dimensional ground inhomogeneity. **Space Weather**, v. 16, n. 12, p. 1946–1959, 2018. Available from: <https://doi.org/10.1029/2018SW002004>. 43, 69

NGWIRA, C. M.; PULKKINEN, A.; MCKINNELL, L.-A.; CILLIERS, P. J. Understanding GIC in the UK and French high-voltage transmission systems during severe magnetic storms. **Space Weather**, v. 6, n. 11, p. S11004, 2008. Available from: <https://doi.org/10.1029/2008SW000408>. 1

NUNES, K. C. Interpretação integrada da Bacia do Parnaíba com ênfase nos dados aeromagnetométricos. In: INTERNATIONAL CONGRESS OF THE BRAZILIAN GEOPHYSICAL SOCIETY, 1993. **Proceedings...** [S.l.]: Rio de Janeiro, Brazil: SBGf, 1993. p. 152–157. 72

OLIVEIRA, D. M.; AREL, D.; RAEDER, J.; ZESTA, E.; NGWIRA, C. M.; CARTER, B. A.; YIZENGAW, E.; HALFORD, A. J.; TSURUTANI, B. T.; GJERLOEV, J. W. Geomagnetically induced currents caused by interplanetary shocks with different impact angles and speeds. **Space Weather**, v. 16, n. 6, p. 636–647, 2018. Available from: <https://doi.org/10.1029/2018SW001880>. 70

PADILHA, A.; TAKAHASHI, H.; DE PAULA, E.; SAWANT, H.; CAMPOS VELHO, H.; VITORELLO, I.; COSTA, J.; SOUZA, J.; CECATTO, J.; MENDES, O.; GONZALEZ, W. D. Brazilian Space Weather Program. In: COSPAR SCIENTIFIC ASSEMBLY, 37, 2008. **Proceedings...** Montreal, Canada: COSPAR, 2008. Available from: <https://ui.adsabs.harvard.edu/abs/2008cosp...37.2326P/abstract>. 1

PADILHA, A. L.; ALVES, M. V.; TRIVEDI, N. B.; KITAMURA, T.-I.; SHINOHARA, M. Bursty Pi1 activity at the South American equatorial zone during the 29 October 1994 magnetic storm. **Geophysical Research Letters**, v. 30, 2003. Available from: <https://doi.org/10.1029/2003GL017999>. 13

PADILHA, A. L.; VITORELLO, I.; ANTUNES, C. E.; PÁDUA, M. B. Imaging three-dimensional crustal conductivity structures reflecting continental flood basalt effects hidden beneath thick intracratonic sedimentary basin. **Journal of Geophysical Research: Solid Earth**, v. 120, n. 7, p. 4702–4719, 2015. Available from: <https://doi.org/10.1002/2014JB011657>. xvi, 48, 49, 50

PADILHA, A. L.; VITORELLO, I.; PÁDUA, M. B.; FUCK, R. A. Cryptic signatures of Neoproterozoic accretionary events in northeast Brazil imaged by magnetotellurics: implications for the assembly of West Gondwana. **Tectonophysics**, v. 699, p. 164–177, 2017. ISSN 00401951. Available from: <https://doi.org/10.1016/j.tecto.2017.01.022>. 39, 73, 74, 76, 86

PADILHA, A. L.; VITORELLO, Í.; RIJO, L. Effects of the equatorial electrojet on magnetotelluric surveys: field results from Northwest Brazil. **Geophysical Research Letters**, v. 24, n. 1, p. 89–92, 1997. ISSN 00948276. Available from: <https://doi.org/10.1029/96GL03792>. 13

PARKINSON, W. D. The influence of continents and oceans on geomagnetic variations. **Geophysical Journal International**, v. 6, p. 441–449, 1962. Available from: <https://doi.org/10.1111/j.1365-246X.1962.tb02992.x>. 22

PAULIKAS, G. A. Precipitation of particles at low and middle latitudes. **Reviews of Geophysics and Space Physics**, v. 13, p. 709–734, 1975. Available from: <http://dx.doi.org/10.1029/RG013i005p00709>. 13

PFAFF JR., R. F.; ACUÑA, M. H.; MARIONNI, P. A.; TRIVEDI, N. B. DC polarization electric field, current density, and plasma density measurements in the daytime equatorial electrojet. **Geophysical Research Letters**, v. 24, n. 13, p. 1667–1670, 1997. Available from: <https://doi.org/10.1029/97GL01536>. 13

PIRJOLA, R. Geomagnetically induced currents during magnetic storms. **IEEE Transactions on Plasma Science**, v. 28, n. 6, p. 1867–1873, 2000. Available from: <http://dx.doi.org/10.1109/27.902215>. 1

_____. Review on the calculation of surface electric and magnetic fields and of geomagnetically induced currents in ground-based technological systems. **Surveys in Geophysics**, v. 23, n. 1, p. 71–90, 2002. ISSN 01693298. Available from: <https://doi.org/10.1023/A:1014816009303>. 2, 64

_____. Calculation of Geomagnetically Induced Currents (GIC) in a high-voltage electric power transmission system and estimation of effects of overhead shield wires on GIC modelling. **Journal of Atmospheric and Solar-Terrestrial Physics**, v. 69, n. 12, p. 1305–1311, 2007. ISSN 13646826. Available from: <https://doi.org/10.1016/j.jastp.2007.04.001>. 8

PULKKINEN, A.; AMM, O.; VILJANEN, A. Ionospheric equivalent current distributions determined with the method of spherical elementary current systems ionospheric equivalent current distributions determined with the method of spherical elementary current systems. **Journal of Geophysical Research: Space Physics**, v. 108, n. A2, p. 1053, 2003. Available from: <https://doi.org/10.1029/2001JA005085>. 26, 27, 55

PULKKINEN, A.; BERNABEU, E.; EICHNER, J.; BEGGAN, C.; THOMSON, A. W. P. Generation of 100-year geomagnetically induced current scenarios. **Space**

Weather, v. 10, p. S04003, 2012. Available from: <https://doi.org/10.1029/2011SW000750>. 7, 63

PULKKINEN, A.; BERNABEU, E.; EICHNER, J.; VILJANEN, A.; NGWIRA, C. Regional-scale high-latitude extreme geoelectric fields pertaining to geomagnetically induced currents. **Earth, Planets and Space**, v. 67, p. 93, 2015. Available from: <https://doi.org/10.1186/s40623-015-0255-6>. 1

PULKKINEN, A.; LINDAHL, S.; VILJANEN, A.; PIRJOLA, R. Geomagnetic storm of 29-31 October 2003: geomagnetically induced currents and their relation to problems in the Swedish high-voltage power transmission system. **Space Weather**, v. 3, n. 8, p. S08C03, 2005. Available from: <https://doi.org/10.1029/2004SW000123>. 1

PULKKINEN, A.; VILJANEN, A.; PIRJOLA, R. Estimation of geomagnetically induced current levels from different input data. **Space Weather**, v. 4, n. 8, p. S08005, 2006. Available from: <https://doi.org/10.1029/2006SW000229>. 3

RATHORE, B.; KAUSHIK, S.; BHADORIA, R.; PARASHAR, K.; GUPTA, D. Sunspots and geomagnetic storms during solar cycle-23. **Indian Journal of Physics**, n. 7, p. 563–567, July 2012. Available from: <https://doi.org/10.1007/s12648-012-0106-2>. 12

RIGLER, E.; FIORI, R.; PULKKINEN, A.; WILTBERGER, M.; BALCH, C. Interpolating geomagnetic observations: techniques and comparisons. In: GANNON, J. L.; SWIDINSKY, A.; XU, Z. (Ed.). **Geomagnetically induced currents from the Sun to the power grid**. Washington, DC, USA: American Geophysical Union, 2019, (Geophysical Monograph Series). p. 15–41. Available from: <https://doi.org/10.1002/9781119434412.ch2>. 29, 31, 55

RIGOTI, A.; CHAMALAUN, F. H.; TRIVEDI, N. B.; PADILHA, A. L. Characteristics of the equatorial electrojet determined from an array of magnetometers in N-NE Brazil. **Earth, Planets and Space**, v. 51, n. 2, p. 115–128, 1999. Available from: <https://doi.org/10.1186/BF03352216>. 13, 33, 77, 78, 86

ROBERTSON, K.; HEINSON, G.; THIEL, S. Lithospheric reworking at the Proterozoic–Phanerozoic transition of Australia imaged using AusLAMP Magnetotelluric data. **Earth and Planetary Science Letters**, v. 452, p. 27–35, 2016. Available from: <https://doi.org/10.1016/j.epsl.2016.07.036>. 2

ROCHA, N. S.; FONTES, S. L.; LA TERRA, E. F.; FUCK, R. A. Lithosphere structures of the Parnaíba Basin and adjacent provinces revealed by deep magnetotelluric imaging. **Journal of South American Earth Sciences**, v. 92, n. June 2018, p. 1–11, 2019. ISSN 08959811. Available from: <https://doi.org/10.1016/j.jsames.2019.02.020>. 74

SCHULTZ, A.; EGBERT, G. D.; KELBERT, A.; PEERY, T.; CLOTE, V.; B. FRY, S. EROFEEVA; and staff of the national geoelectromagnetic facility and their contractors (2006-2018). **USArray TA magnetotelluric transfer functions**. USA, 2001–2011. Retrieved from the IRIS database on Oct 30, 2018. Available from: <https://doi.org/10.17611/DP/EMTF/USARRAY/TA>. 41

SHINBORI, A.; NISHIMURA, Y.; TSUJI, Y.; KIKUCHI, T.; ARAKI, T.; IKEDA, A.; UOZUMI, T.; OTADOY, R.; UTADA, H.; ISHITSUKA, J.; TRIVEDI, N. B.; DUTRA, S.; SCHUCH, N. J.; WATARI, S.; NAGATSUMA, T.; YUMOTO, K. Anomalous occurrence features of the preliminary impulse of geomagnetic sudden commencement in the South Atlantic Anomaly region. **Journal of Geophysical Research: Space Physics**, v. 115, n. A8, 2010. ISSN 21699402. Available from: <https://doi.org/10.1029/2009JA015035>. 13

SHINOHARA, M.; YUMOTO, K.; HOSEN, N.; YOSHIKAWA, A.; TACHIHARA, H.; SAKA, O.; KITAMURA, T.; TRIVEDI, N. B.; DA COSTA, J. M.; SCHUCH, N. J. Wave characteristics of geomagnetic pulsations across the dip equator. **Journal of Geophysical Research**, v. 103, n. A6, p. 745–754, 1998. ISSN 0148-0227. Available from: <https://doi.org/10.1029/97JA03067>. 13

SIMPSON, F.; BAHR, K. **Practical magnetotellurics**. United Kingdom: Cambridge University Press, 2005. ISBN 9780511614095. 14, 15

SIRIPUNVARAPORN, W.; EGBERT, G.; LENBURY, Y.; UYESHIMA, M. Three-dimensional magnetotelluric inversion: data-space method. **Physics of the Earth and Planetary Interiors**, v. 150, p. 3–14, 2005a. Available from: <https://doi.org/10.1016/j.pepi.2004.08.023>. 2

SIRIPUNVARAPORN, W.; EGBERT, G.; UYESHIMA, M. Interpretation of two-dimensional magnetotelluric profile data with three-dimensional inversion: synthetic examples. **Geophysical Journal International**, v. 160, p. 804–814, 2005b. Available from: <https://doi.org/10.1111/j.1365-246X.2005.02527.x>. 34

SMITH, S. W. **Digital signal processing: a practical guide for engineers and scientists**. Amsterdam, Netherlands: Elsevier, 2013. ISBN 075067444X. 52, 61, 94

SOLON, F. F.; FONTES, S. L.; LA TERRA, E. F. Electrical conductivity structure across the Parnaíba Basin, NE Brazil. **Geological Society Special Publication**, v. 472, n. 1, p. 109–126, 2018. ISSN 03058719. Available from: <https://doi.org/10.1144/SP472.19>. 33, 39, 73, 74, 76

TAYLOR, P. O. **Solar Bulletin**. Athens, GA. USA, 1990. The American Association of Variables Start Observers-Solar Division (AAVSO). Available from: <https://www.aavso.org/sites/default/files/solar_bulletin/AAVSO_SB_1990_11.pdf>. 79

_____. _____. Athens, GA. USA, 1991. Available from: <https://www.aavso.org/sites/default/files/solar_bulletin/AAVSO_SB_1991_02.pdf>. 84

TORTA, J. M.; MARCUELLO, A.; CAMPANYÀ, J.; MARSAL, S.; QUERALT, P.; LEDO, J. Improving the modeling of geomagnetically induced currents in Spain. **Space Weather**, v. 15, p. 691–703, 2017. Available from: <https://doi.org/10.1002/2017SW001628>. 55

TORTA, J. M.; MARSAL, S.; QUINTANA, M. Assessing the hazard from geomagnetically induced currents to the entire high-voltage power network in Spain. **Earth, Planets and Space**, v. 66, p. 87, 2014. Available from: <https://doi.org/10.1186/1880-5981-66-87>. 54, 69

TORTA, J. M.; SERRANO, L.; REGUÉ, J. R.; SÁNCHEZ, A. M.; ROLDÁN, E. Geomagnetically induced currents in a power grid of northeastern Spain. **Space Weather**, v. 10, p. S06002, 2012. Available from: <https://doi.org/10.1029/2012SW000793>. 1

TRICHTCHENKO, L.; BOTELER, D. H. Response of power systems to the temporal characteristics of geomagnetic storms. In: CANADIAN CONFERENCE ON ELECTRICAL AND COMPUTER ENGINEERING, 2006. **Proceedings...** Ottawa, Canada: IEEE, 2006. p. 390–393. Available from: <https://doi.org/10.1109/CCECE.2006.277733>. 66

TRIVEDI, N.; PATHAN, B.; SCHUCH, N.; BARRETO, M.; DUTRA, L. Geomagnetic phenomena in the South Atlantic anomaly region in Brazil. **Advances in Space Research**, v. 36, n. 10, p. 2021–2024, 2005. ISSN 02731177. Available from: <https://doi.org/10.1016/j.asr.2004.09.020>. 13, 14, 51

TRIVEDI, N. B.; ARORA, B. R.; PADILHA, A. L.; COSTA, J. M.; DUTRA, S. .; CHAMALAUN, F. H.; RIGOTI, A. Global Pc5 geomagnetic pulsations of March 24, 1991, as observed along the American sector. **Geophysical Research Letters**, v. 24, n. 13, p. 1683–1686, 1997. Available from: <https://doi.org/10.1029/97GL00215>. 13

TRIVEDI, N. B.; VITORELLO, F.; KABATA, W.; DUTRA, S. L. G.; PADILHA, A. L.; BOLOGNA, M. S.; PÁDUA, M. B.; SOARES, A. P.; LUZ, G. S.; PINTO, F. A.; PIRJOLA, R.; VILJANEN, A. Geomagnetically induced currents in an electric power transmission system at low latitudes in Brazil: a case study. **Space Weather**, v. 5, n. 4, p. 04004, 2007. Available from: <https://doi.org/10.1029/2006SW000282>. 1, 2, 3

UDDIN, W.; VERMA, V. Eruptive prominence associated with limb flare of 25 january 1991. **International Astronomical Union Colloquium**, v. 154, p. 173–177, 1996. Available from: <http://dx.doi.org/10.1017/S0252921100030141>. 82

UDDIN, W.; VERMA, V. K.; PANDE, M. C. Recurrent surge activity from active region noaa:6368. **Journal of Astrophysics and Astronomy Supplement**, v. 16, p. 387, dec. 1995. 1995JApAS..16..387U. 79

VANHAMÄKI, H.; AMM, O. Analysis of ionospheric electrodynamic parameters on mesoscales - a review of selected techniques using data from ground-based observation networks and satellites. **Annales Geophysicae**, v. 29, n. 3, p. 467–491, 2011. ISSN 09927689. Available from: <https://doi.org/10.5194/angeo-29-467-2011>. 55

VANHAMÄKI, H.; JUUSOLA, L. **Introduction to spherical elementary current systems.** Springer International Publishing, 2020. 5–33 p. ISBN 9783030267322. Available from: <https://doi.org/10.1007/978-3-030-26732-2>. 26

VAZ, P. T.; REZENDE, N. G. A. M.; WANDERLEY FILHO, J. R.; SILVA TRAVASSOS, W. A. Bacia do Parnaíba. **Boletim de Geociencias da Petrobras**, v. 15, p. 253–263, 2007. 71

VICHARE, G.; RAWAT, R.; BHASKAR, A.; PATHAN, B. M. Ionospheric current contribution to the main impulse of a negative sudden impulse. **Earth, Planets and Space**, v. 66, n. 92, p. 1880–1118, 2014. Available from: <https://doi.org/10.1186/1880-5981-66-92>. 10

VILJANEN, A.; NEVANLINNA, H.; PAJUNPÄÄ, K.; PULKKINEN, A. Time derivative of the horizontal geomagnetic field as an activity indicator. **Annales Geophysicae**, v. 19, n. 9, p. 1107–1118, 2001. Available from: <https://doi.org/10.5194/angeo-19-1107-2001>. 56, 65

VILJANEN, A.; PIRJOLA, R. Influence of spatial variations of the geoelectric field on geomagnetically induced currents. **Journal of Space Weather and Space Climate**, v. 7, p. A22, 2017. Available from: <https://doi.org/10.1051/swsc/2017024>. 63

VILJANEN, A.; PIRJOLA, R.; WIK, M.; ÁDAM, A.; PRACSER, E.; SAKHAROV, Y.; KATKALOV, J. Continental scale modelling of geomagnetically induced currents. **Journal of Space Weather and Space Climate**, v. 2, p. A17, 2012. Available from: <https://doi.org/10.1051/swsc/2012017>. 2

WATARI, S.; KUNITAKE, M.; KITAMURA, K.; HORI, T.; KIKUCHI, T.; SHIOKAWA, K.; NISHITANI, N.; KATAOKA, R.; KAMIDE, Y.; ASO, T.; WATANABE, Y.; TSUNETA, Y. Measurements of geomagnetically induced current in a power grid in Hokkaido, Japan. **Space Weather**, v. 7, n. 3, p. 03002, 2009. Available from: <https://doi.org/10.1029/2008SW000417>. 1, 66

WATARI, S.; NAKAMURA, S.; EBIHARA, Y. Measurement of Geomagnetically Induced Current (GIC) around Tokyo , Japan. **Earth, Planets and Space**, 2021. ISSN 1880-5981. Available from: <https://doi.org/10.1186/s40623-021-01422-3>. 3

WEIGEL, R. S. A comparison of methods for estimating the geoelectric field. **Space Weather**, v. 15, n. 2, p. 430–440, 2017. Available from: <https://doi.org/10.1002/2016SW001504>. 2, 30

WEYGAND, J. M.; AMM, O.; VILJANEN, A.; ANGELOPOULOS, V.; MURR, D.; ENGEBRETSON, M. J.; GLEISNER, H.; MANN, I. Application and validation of the spherical elementary currents systems technique for deriving ionospheric equivalent currents with the North American and Greenland ground magnetometer arrays. **Journal of Geophysical Research: Space Physics**, v. 116, n. 3, p. 1–8, 2011. ISSN 21699402. Available from: <https://doi.org/10.1029/2010JA016177>. 55

ZALÁN, P. V.; WOLFF, S.; ASTOLFI, M. A. M.; VIEIRA, I. S.; CONCEIÇÃO, J. C. J.; APPI, V. T.; NETO, E. V. S.; CERQUEIRA, J. R.; MARQUES, A. The Paraná Basin, Brazil. In: LEIGHTON, M. W.; KOLATA, D. R.; OLTZ, D. F.;

EIDEL, J. J. (Ed.). **Interior cratonic basins**. Tulsa, OK, USA: American Association of Petroleum Geologists, 1990. p. 681–708. Available from: <https://doi.org/10.1306/M51530C34>. 48

ZANANDREA, A. **Estudos de micropulsações geomagnéticas pc3-5 em latitudes muito baixas no Brasil**. Tese (Doutorado em Geofísica Espacial) — Instituto Nacional de Pesquisas Espaciais, São José dos Campos, 1999. Available from: <http://marte3.sid.inpe.br/col/sid.inpe.br/deise/1999/10.14.15.11/doc/publicacao.pdf>. 13

ZHENG, K.; BOTELER, D.; PIRJOLA, R. J.; LIU, L.; BECKER, R.; MARTI, L.; BOUTILIER, S.; GUILLON, S. Effects of system characteristics on geomagnetically induced currents. **IEEE Transactions on Power Delivery**, v. 29, n. 2, p. 890–898, 2014. Available from: <https://doi.org/10.1109/TPWRD.2013.2281191>. 54, 69, 113

ZONGE, K. L.; HUGHES, L. J. Controlled source audio-frequency magnetotellurics. In: NABIGHIAN, M. N. (Ed.). **Electromagnetic methods in applied geophysics: volume 2, application, parts A and B**. Tulsa, OK, USA: Society of Exploration Geophysicists, 1991. p. 713–810. Available from: <https://doi.org/10.1190/1.9781560802686.ch9>. 14

PUBLICAÇÕES TÉCNICO-CIENTÍFICAS EDITADAS PELO INPE

Teses e Dissertações (TDI)

Teses e Dissertações apresentadas nos Cursos de Pós-Graduação do INPE.

Notas Técnico-Científicas (NTC)

Incluem resultados preliminares de pesquisa, descrição de equipamentos, descrição e ou documentação de programas de computador, descrição de sistemas e experimentos, apresentação de testes, dados, atlas, e documentação de projetos de engenharia.

Propostas e Relatórios de Projetos (PRP)

São propostas de projetos técnico-científicos e relatórios de acompanhamento de projetos, atividades e convênios.

Publicações Seriadas

São os seriados técnico-científicos: boletins, periódicos, anuários e anais de eventos (simpósios e congressos). Constam destas publicações o Internacional Standard Serial Number (ISSN), que é um código único e definitivo para identificação de títulos de seriados.

Pré-publicações (PRE)

Todos os artigos publicados em periódicos, anais e como capítulos de livros.

Manuais Técnicos (MAN)

São publicações de caráter técnico que incluem normas, procedimentos, instruções e orientações.

Relatórios de Pesquisa (RPQ)

Reportam resultados ou progressos de pesquisas tanto de natureza técnica quanto científica, cujo nível seja compatível com o de uma publicação em periódico nacional ou internacional.

Publicações Didáticas (PUD)

Incluem apostilas, notas de aula e manuais didáticos.

Programas de Computador (PDC)

São a seqüência de instruções ou códigos, expressos em uma linguagem de programação compilada ou interpretada, a ser executada por um computador para alcançar um determinado objetivo. Aceitam-se tanto programas fonte quanto os executáveis.